2010

Experimental And Theoretical Approaches To Characterization Of Electronic Nonlinearities In Direct-gap Semiconductors

Claudiu Cirloganu
University of Central Florida

EXPERIMENTAL AND THEORETICAL APPROACHES TO CHARACTERIZATION OF ELECTRONIC NONLINEARITIES IN DIRECT-GAP SEMICONDUCTORS

by

CLAUDIU CIRLOGANU
B.S. University of Bucharest, 2000
M.S. University of Central Florida, 2003

A dissertation submitted in partial fulfillment of the requirements
for the degree of Doctor of Philosophy
in the College of Optics and Photonics: CREOL & FPCE
at the University of Central Florida
Orlando, Florida

Summer Term
2010

Major Professors: Eric W. Van Stryland and David J. Hagan

ABSTRACT

The general goal of this dissertation is to provide a comprehensive description of the limitations of established theories on bound electronic nonlinearities in direct-gap semiconductors by performing various experiments on wide and narrow bandgap semiconductors along with developing theoretical models. Nondegenerate two-photon absorption (2PA) is studied in several semiconductors showing orders of magnitude enhancement over the degenerate counterpart. In addition, three-photon absorption (3PA) is studied in ZnSe and other semiconductors and a new theory using a Kane 4-band model is developed which fits new data well. Finally, the narrow gap semiconductor InSb is studied with regard to multiphoton absorption, free-carrier nonlinearities and decay mechanisms.

The non-degenerate two-photon absorption was investigated in several direct-gap semiconductors with picosecond and femtosecond pulses. Large enhancements in 2PA were demonstrated when employing highly non-degenerate photon pairs and the results were shown to be consistent to a simple 2-parabolic band theory based on a “dressed” state approach. The nonlinear refractive index induced in such configurations was also calculated and possible implications of such extreme behavior are discussed.

A large number of measurements of 3PA were taken at multiple wavelengths and in several semiconductors. The subsequent analysis has shown that simple 2-band model calculations (based on either perturbative or tunneling approaches) do not adequately describe the experimental trends. A more comprehensive model, based on Kane’s 4-band theory was developed and we calculate three-photon spectra for zincblende structures within the perturbative

framework. We have confirmed the results of our calculations performing a series of Z-scans in semiconductors ZnSe and ZnS, yielding complete experimental three-photon spectra.

A systematic approach based on using a large variety of pulse durations was needed to quantify the wealth of nonlinear optical processes in InSb, accessible in the mid-infrared range. Femtosecond pulses provided a lower limit to measurements of the instantaneous effects (absorptive and refractive), while picosecond pulses allowed further characterization of the free-carrier effects, including population dynamics in the high density regime (Auger effects). The model developed permitted us to verify the temperature dependence of free-carrier absorption recently predicted, and to successfully model optical limiting data with longer, nanosecond pulses.

This dissertation is dedicated to my family, extremely patient with me during all these years

ACKNOWLEDGMENTS

I want to take this opportunity to thank my advisers Dr. Eric Van Stryland and Dr. David Hagan. I was part of a large group and although they both had incredibly busy schedules there was always enough time for me and my problems, pretty much whenever I needed. I feel very fortunate for having this opportunity to interact and learn from them and to take advantage of the great insight they always provided.

I would also like to extend my thanks to the members of the committee, Dr. Eduardo Mucciolo, Dr. Patrick LiKamWa and Dr. George Stegeman. I truly enjoyed the courses taught by them as they sparked my interests in the topics that would later become the central part of my research work. I am grateful for their advice and help, kindly given whenever it was sought, particularly in my final years.

As I mentioned, our research group was always a big one. I feel very fortunate to have interacted with a large number of people from different generations. I would like to specifically thank Mihaela Balu for the scientific and non-scientific conversations that always offered a fresh perspective on things and who encouraged me whenever I needed it. Also, Rich Lepkowicz who took me under his wing in my first years and basically taught me the basics and helped me find my way in the lab. I want to thank here the current members of our group, particularly Scott, Dima, Gero, Trent, Dado, HHH and Peter who have helped me in so many ways and were so nice to tolerate my sometimes quirky behavior. I will never forget our deep conversations on the balcony which were truly eye-opening and spiritually enlightening at times. I will definitely miss you guys wherever I go!

Being part of CREOL was indeed a great experience. The people here were always happy to help and always had a smile on their faces. Whoever they were, Amy, Gail, Mark, Vicky, Matt, Maria, Richard or Rachel, there was always a pleasant experience from beginning to end, with really no exceptions. Particularly, Rachel thank you for the extra effort put in whenever I would complicate things.

Last, but not least, I would like to thank Izabela, my parents, my sister and Maxi for their love and support. You guys managed to still believe in me all these years and never lost faith that graduation day would eventually come. Thank you for putting up with my procrastinating nature and I appreciate getting past the difficult situations I've put you through.

TABLE OF CONTENTS

LIST OF FIGURES

LIST OF TABLES

LIST OF ACRONYMS/ABBREVIATIONS

2PA	Two-Photon Absorption
3PA	Three-Photon Absorption
cm	Centimeter (10^{-2} m)
ESA	Excited-State Absorption
eV	Electron-Volt unit of energy
fs	Femtosecond (10^{-15}s)
FWHM	Full Width Half Maximum
FCA	Free-Carrier Absorption
FCR	Free-Carrier Refraction
GVD	Group-Velocity Dispersion
IR	Infrared
kHz	Kilohertz (10^{3} Hz)
μJ	Microjoule (10^{-6} J)
μm	Micrometer (10^{-6} m)
NBF	Narrow Band Filter
nJ	Nanojoule (10^{-9} J)
nm	Nanometer (10^{-9}m)
NLA	Nonlinear Absorption
NLR	Nonlinear Refraction
OPA	Optical Parametric Amplifier
OPG	Optical Parametric Generator

pJ	Picojoule (10^{-12} J)
ps	Picosecond (10^{-12} s)
SVEA	Slowly-Varying Envelope Approximation
SW	Single Wavelength
UV	Ultraviolet
WLC	White-Light Continuum

CHAPTER 1: INTRODUCTION

1.1. Background and Motivation

The field of nonlinear optics is a rich one. There are always numerous facets being explored experimentally and also numerous theoretical models proposed. Besides achieving a certain experimental result, it is equally important to be able to explain it. Once the basic physical mechanisms are understood one can take the next step which is utilizing the gained knowledge to come up with new ideas, applications, devices, etc. If in the past they constituted more of a novelty, nowadays optical nonlinear effects are part of everyday life. As part of a continuous effort to improve the efficiency and the performance of devices, the search for larger nonlinearities goes anywhere from creating new materials with increased nonlinearity to smart design meant to enhance the existing nonlinearities.

The main focus of this work is concerned with multiphoton absorption processes in semiconductors and associated effects, like induced changes of the refraction index and free-carrier effects. Multiphoton absorption processes are related to transitions that occur through the simultaneous absorption of two or more photons and are used in numerous applications like fluorescence imaging [1, 2], microfabrication [3], optical data storage [4] or optical limiting for sensor protection [5]. A strong propagating beam can change locally the index of refraction and such effects are used in optical switching devices [6]. For increased efficiency, low intensities are required implying that large nonlinear Kerr coefficients are needed and with small absorptive effects for useful figures of merit [7].

In order to take the step forward, towards practical applications, the physical phenomena need to be fully explained with working theoretical models. The extensive database of 2PA in

direct-gap semiconductors allowed for the formulation of scaling laws that are able to predict the magnitude of the 2PA coefficient and the nonlinear Kerr coefficient, both degenerate and non-degenerate, using just simple parameters like bandgap energy and index of refraction [8]. For the degenerate 2PA the theory shows that nonlinearity is restricted by the bandgap, as it depends on the inverse of the bandgap energy cubed. This essentially suggests that large nonlinearities may only be measured in narrow gap materials with an obvious trade-off of having to use longer wavelengths. Fortunately, it also predicts that large nonlinearities can be obtained in larger bandgap materials by using highly different energy photons, since this basically makes use of the inherent resonances. This particular aspect, even though predicted by some time, hasn't been fully explored and the limits of these enhancements were not known. In this work, we performed a series of experiments meant to verify whether the excellent agreement between the theory and the experiment holds even for the most extreme cases. These results should provide a very good reference point for measurements of the same nature, by setting an upper value for the highest nonlinearity that can be measured practically in a given semiconductor.

The success of the aforementioned scaling laws prompted several attempts at using similar simple models to describe higher order effects like 3PA. The existing experimental database on 3PA was however much smaller and a clear comparison wasn't possible. The newer publications didn't investigate the apparent discrepancies between the existing theories nor attempted to do a better than order-of-magnitude comparison to the experimental data [9]. An initial effort to check the validity of the scaling laws for the case of 3PA has revealed that the models used cannot explain some of the large variations in values measured at several wavelengths in the same semiconductor [10]. Therefore work needs to be done towards finding a

more complex and in the same time appropriate model, and to provide reliable sets of data over the entire spectra for several materials.

Narrow gap semiconductors are expected to provide the largest degenerate 2PA and they have been the focus of intensive research. The wavelengths of operation for the high power CO_2 lasers are near the peak 2PA of InSb, making this narrow gap semiconductor attractive for applications. However, the early data suffered from improper interpretations as for the longer pulses available at the time the free-carrier effects dominate mask any quasi-instantaneous effects [11, 12]. This led to an extremely large spread in the published values [8], a gross overestimation at times and an overall lack of reliability. Subsequent data seemed to converge toward a generic value of 2 cm/MW [13, 14] which was adopted as a good reference, but no systematic study was done to date. Our experimental efforts were directed towards understanding the interplay between bound and free-carrier effects as this was recognized as the main source of uncertainty in the early data. There is a clear need for a systematic approach to evaluate the capabilities and the limits of measurements in different pulsewidth ranges and various carrier density levels.

1.2. Dissertation Outline

Chapter 2 consists of a general review of the optical nonlinearities studied. Bound electronic nonlinearities arising from $\chi^{(3)}$ (2PA, n_2) and $\chi^{(5)}$ (3PA) terms along with free carrier effects (σ_{abs}, σ_{ref},) will be discussed as they constitute the main experimental focus of this work. A description of the experimental techniques employed throughout and of the laser systems used is made in Chapter 3. Specifics of the performed single beam and pump-probe type experiments

are presented with an emphasis on the particular information that can be extracted from each experiment. Chapter 4 is dedicated to the theoretical models for calculating bound electronic nonlinearities in semiconductors. Issues of advantages, scalability and limitations are addressed as well in this part. The large enhancement of two-photon absorption for the extremely non-degenerate case is discussed in Chapter 5. The experimental data is compared to the theory and a further discussion on the theoretically predicted behavior of the nonlinear refraction index is made. Chapter 6 is dedicated to the 3PA absorption process in direct gap semiconductors exhibiting a zincblende symmetry. A comprehensive theoretical approach based on a 4-band model is presented along with the measured spectra for a few materials. The unique features of these spectra, seen experimentally for the first time, are shown to be the consequence of a quantum interference process. Chapter 7 contains experimental data taken in InSb, a good candidate material for optical limiting in the 10 micron range. The goal of the experiments performed is to offer a close to complete characterization of its nonlinear properties using a variety of techniques employing different duration optical IR pulses. Finally, Chapter 8 provides conclusions and suggests possible future directions based on the work presented in this dissertation.

CHAPTER 2: NONLINEARITIES IN SEMICONDUCTORS

The domain of nonlinear optics deals with the interaction of intense light fields with matter. Nonlinear effects in electricity and magnetism were known ever since the introduction of Maxwell's equations. In the optical domain, however, the interest and the number of experiments grew only after the invention of the laser. Maiman's demonstration of the lasing action in ruby 50 years ago opened the door to a wealth of new phenomena, leading to a better understanding of the fundamentals of light and matter interactions. The use of this coherent, intense source of light not only demonstrated the optical equivalents of effects such as radio waves' rectification or second harmonic generation [15], but also allowed the discovery of new ones.

The second harmonic generation experiment of Franken [16] using a ruby laser is generally regarded as marking the birth of the field of nonlinear optics. It was the first experiment that demonstrated generation of a coherent output from a coherent input. From a general standpoint, the field of nonlinear optics aims to study and characterize the light-matter interaction encompassing such issues as light-induced changes in the optical properties of media. Any medium can be regarded as nonlinear, because any physical oscillating system will exhibit a nonlinear behavior when overdriven. There is however a strength factor associated with a nonlinear process and a particular effect can only be observed if a certain number of requirements are met. One of these requirements, and probably the most stringent one, is having a light source sufficiently intense, of at least of the order of kW/cm^2. This is why the development of powerful light sources helped advance the field of nonlinear optics, while keeping this relationship symbiotic in nature.

Any nonlinear process can be regarded in principle as consisting of two parts. The intense light will first induce a nonlinear response in the medium (action) and then the medium will modify the optical fields in a nonlinear fashion (reaction). It is well known that the action part is governed by the constitutive equations while the reaction part is described by the Maxwell's equations. Since we are dealing with electromagnetic phenomena it is therefore appropriate to start any analysis with the laws governing the behavior of the electric and magnetic fields

$$\begin{aligned} \nabla \times \mathbf{E} &= -\frac{\partial \mathbf{B}}{\partial t} \\ \nabla \times \mathbf{H} &= \frac{\partial \mathbf{D}}{\partial t} + \mathbf{J} \\ \nabla \cdot \mathbf{D} &= \rho \\ \nabla \cdot \mathbf{B} &= 0 \end{aligned} \tag{2.1}$$

We are primarily interested in solving these equations for cases when there are no free charges $\rho = 0$ or free currents $\mathbf{J} = 0$. We will also assume that medium is non-magnetic $\mathbf{B} = \mu_0 \mathbf{H}$ and the nonlinearity is given by $\mathbf{D} = \varepsilon_0 \mathbf{E} + \mathbf{P}$ such that the polarization vector depends nonlinearly upon the strength of the electric field. Using these assumptions we can write the wave equation as

$$\nabla \times \nabla \times \mathbf{E} + \frac{1}{c^2} \frac{\partial^2}{\partial t^2} (\mathbf{E} + \frac{1}{\varepsilon_0} \mathbf{P}) = 0 \tag{2.2}$$

In the general case the nonlinear polarization can be written as a convolution between the incident electric field and the susceptibility function χ which is a property of the medium and describes its response [15]

$$\mathbf{P}(\mathbf{r},t)=\varepsilon_0\int_{-\infty}^{\infty}\chi^{(1)}(\mathbf{r}-\mathbf{r}',t-t')\mathbf{E}(\mathbf{r}',t')d\mathbf{r}'dt'+$$
$$+\varepsilon_0\int_{-\infty}^{\infty}\chi^{(2)}(\mathbf{r}-\mathbf{r}_1,t-t_1;\mathbf{r}-\mathbf{r}_2,t-t_2):\mathbf{E}(\mathbf{r}_1,t_1)\mathbf{E}(\mathbf{r}_2,t_2)d\mathbf{r}_1dt_1d\mathbf{r}_2dt_2+$$
$$+\varepsilon_0\int_{-\infty}^{\infty}\chi^{(3)}(\mathbf{r}-\mathbf{r}_1,t-t_1;\mathbf{r}-\mathbf{r}_2,t-t_2;\mathbf{r}-\mathbf{r}_3,t-t_3):\mathbf{E}(\mathbf{r}_1,t_1)\mathbf{E}(\mathbf{r}_2,t_2)\mathbf{E}(\mathbf{r}_3,t_3)d\mathbf{r}_1dt_1d\mathbf{r}_2dt_2d\mathbf{r}_3dt_3+$$
$$+\ldots \tag{2.3}$$

where $\chi^{(n)}$ is the n-th order susceptibility. Given the complex description in variables $\mathbf{r}$ and t, it is useful to shift the analysis in the Fourier space by means of a Fourier transform to variables $\mathbf{k}$ and ω, respectively. This way the convolution operation turns into a simple product allowing us to express the polarization as

$$\begin{aligned}\mathbf{P}(\mathbf{k},\omega)=\varepsilon_0\chi^{(1)}(\mathbf{k},\omega)\mathbf{E}(\mathbf{k},\omega)+\varepsilon_0\chi^{(2)}(\mathbf{k}=\mathbf{k}_i+\mathbf{k}_j,\omega=\omega_i+\omega_j):\mathbf{E}(\mathbf{k}_i,\omega_i)\mathbf{E}(\mathbf{k}_j,\omega_j)+\\+\varepsilon_0\chi^{(3)}(\mathbf{k}=\mathbf{k}_i+\mathbf{k}_j+\mathbf{k}_l,\omega=\omega_i+\omega_j+\omega_l):\mathbf{E}(\mathbf{k}_i,\omega_i)\mathbf{E}(\mathbf{k}_j,\omega_j)\mathbf{E}(\mathbf{k}_l,\omega_l)+\ldots\end{aligned} \tag{2.4}$$

with nonlinear susceptibilities obtained from

$$\begin{aligned}\chi^{(n)}(\mathbf{k}=\mathbf{k}_1+\mathbf{k}_2+\ldots+\mathbf{k}_n,\omega=\omega_1+\omega_2+\ldots+\omega_n)=\\=\int_{-\infty}^{\infty}\chi^{(n)}(\mathbf{r}-\mathbf{r}_1,t-t_1;\ldots;\mathbf{r}-\mathbf{r}_n,t-t_n)\times\\\times\exp\{-i[\mathbf{k}_1(\mathbf{r}-\mathbf{r}_1)-\omega_1(t-t_1)+\ldots+\mathbf{k}_n(\mathbf{r}-\mathbf{r}_n)-\omega_n(t-t_n)]\}d\mathbf{r}_1dt_1\ldots d\mathbf{r}_ndt_n\end{aligned} \tag{2.5}$$

This expression shows that for the n-th order nonlinearity there are n interacting fields inducing a nonlinear polarization which acts as a source term for the n+1 fields. The calculated susceptibilities allow for the characterization of the optical properties of a medium, predicting all nonlinear effects. Appropriate models can be considered for each physical situation (or nonlinearity) which restrict the number of parameters and make calculations possible. In this work the discussion is restricted to electronic contribution to the susceptibilities i.e. we are considering only processes that involve electronic transitions between well-defined states.

Although simple models as the anharmonic oscillator model ("electron on a spring") and free-electron gas model can be employed, the medium response can only be properly calculated using a full quantum mechanical description. This approach relies on the description of the interaction by means of a perturbation Hamiltonian and the electronic states of the systems and their energy levels. More details for some specific cases will be presented in Chapters 4 and 7.

Strictly speaking, the power expansion of the polarization field in terms of the amplitude of the incident field works for an instantaneous response and assumes locality i.e. the nonlinear polarization at a given point depends on the electric field at that point only. The response of the medium isn't in reality instantaneous and there are also cases where the locality assumption is not valid (electrostriction for instance).

For the case of transitions involving bound electrons (referred to as pure $\chi^{(n)}$ effects), the response time is extremely fast (much faster than the pulse duration) so this is a rather good approximation. There are however, numerous other nonlinear effects with response times varying over many orders of magnitude. For instance, the index variations experienced by a strong beam can be caused by the nonlinear Kerr coefficient (n_2) related to the real part of $\chi^{(3)}$, the accumulation of free-carriers, electrostriction or thermal effects. There is a tendency of labeling all such effects in a similar manner to the quasi-instantaneous effects thus creating confusion and inconsistent comparisons. In this work we deal with both fast nonlinearities (bound effects) and slow ones, related to temporal evolution of carrier population densities. A clear delimitation of such effects will be made through accurate descriptions of the specific mechanisms, avoiding labels such as "effective $\chi^{(n)}$".

2.1. Bound electronic nonlinearities

As mentioned in the previous paragraph, the bound electronic nonlinearities are quasi-instantaneous so the above formulated mathematical description is adequate. We will continue this treatment restricting ourselves to particular terms in the power expansion of the nonlinear polarization in Eq. 2.4. Of interest for this work are the terms related to $\chi^{(3)}$ and $\chi^{(5)}$. A more detailed discussion will be made only for the third-order term while the important results will only be stated for the fifth-order term, of interest for three-photon absorption.

Let us consider the incident electric fields written in terms of its Fourier components as

$$\mathbf{E}(\mathbf{r},t) = \int_{-\infty}^{\infty} \mathbf{E}(\mathbf{r},\omega) e^{-j\omega t} d\omega \tag{2.6}$$

Using Eq. 2.5 and considering a given Cartesian coordinate system, an arbitrary component of the third-order nonlinear polarization, denoted by *i*, can be written in the following form

$$\mathbf{P}_i^{(3)}(\omega) = \varepsilon_0 \chi_{ijkl}^{(3)}(\omega;\omega_1\omega_2\omega_3)\mathbf{E}_j(\omega_1)\mathbf{E}_k(\omega_2)\mathbf{E}_l(\omega_3) \tag{2.7}$$

where the *j*,*k* and *l* are projections of the total electric field at the respective frequencies onto the axes of the chosen coordinate system. There are a couple of comments that need to be made here. The *j*,*k* and *l* indices can independently take on the values x, y or z, such that in the expression of *i* component of the nonlinear polarization we have actually a sum over all terms generated through circular permutations. Also, since these indices are just dummy variables we shall have the same value for a particular $\chi_{ijkl}^{(3)}$ component if the indices are permuted together with the respective frequencies. This property is called *intrinsic permutation symmetry*. Also, given the fact that the fields are real quantities it can be shown that in general

$$\chi^{(n)}(\omega;\omega_1+\omega_2+...\omega_n) = \chi^{(n)*}(-\omega;-\omega_1-\omega_2-...-\omega_n) \tag{2.8}$$

More details on symmetry properties of the nonlinear susceptibilities can be found in standard textbooks [15, 17].

Of interest to us is the particular case of two different frequency inputs denoted by ω_a and ω_b such that the total electric field can be described by

$$\mathbf{E}(\omega_1) = \frac{1}{2}\left\{\mathbf{E}(\omega_a)\delta(\omega_1 - \omega_a) + \mathbf{E}^*(\omega_a)\delta(\omega_1 + \omega_a) + \mathbf{E}(\omega_b)\delta(\omega_1 - \omega_b) + \mathbf{E}^*(\omega_b)\delta(\omega_1 + \omega_b)\right\} \quad (2.9)$$

Using the electric field written in this way one can identify the terms which appear in the expression of the third-order nonlinear polarization and associate them to specific processes. In general, we can identify three types of terms and their complex conjugates:

- $E(\omega_a)^3$ or $E(\omega_a)^3$ correspond to third-harmonic generation (THG) process; overall energy conservation requires $\omega = 3\omega_a$ or $\omega = 3\omega_b$
- $\left(\left|E(\omega_a)\right|^2 + \left|E(\omega_b)\right|^2\right)E_a$ or $\left(\left|E(\omega_a)\right|^2 + \left|E(\omega_b)\right|^2\right)E_b$ correspond to the so-called "intensity dependent" effects (two-photon absorption $\alpha^{(2)}$ and the nonlinear Kerr coefficient (n_2)) acting either on the same input frequency ("self"effects) or the other frequency ("cross" effects); overall energy conservation requires $\omega = \omega_a + \omega_a - \omega_a = \omega_a + \omega_b - \omega_b$ or $\omega = \omega_b + \omega_b - \omega_b = \omega_b + \omega_a - \omega_a$
- $E(\omega_a)^2(E(\omega_b) + E^*(\omega_b))$ or $E(\omega_b)^2(E(\omega_a) + E^*(\omega_a))$ correspond to Coherent Stokes and Anti-Stokes Raman Scattering; overall energy conservation requires $\omega = 2\omega_a \pm \omega_b$ or $\omega = 2\omega_b \pm \omega_a$.

We are going to consider now only the $\chi^{(3)}$ nonlinearities corresponding to the above mentioned "intensity dependent" effects. Explicitly, the respective nonlinear third-order polarization terms are

$$\begin{aligned} P^{(3)}(\omega_a) &= \frac{3}{4}\varepsilon_0\chi^{(3)}(\omega_a;\omega_a,-\omega_a,\omega_a)\left|E(\omega_a)\right|^2 E(\omega_a) + \\ &+ \frac{6}{4}\varepsilon_0\chi^{(3)}(\omega_a;\omega_b,-\omega_b,\omega_a)\left|E(\omega_b)\right|^2 E(\omega_a) \end{aligned} \tag{2.10}$$

and

$$\begin{aligned} P^{(3)}(\omega_b) &= \frac{3}{4}\varepsilon_0\chi^{(3)}(\omega_b;\omega_b,-\omega_b,\omega_b)\left|E(\omega_b)\right|^2 E(\omega_b) + \\ &+ \frac{6}{4}\varepsilon_0\chi^{(3)}(\omega_b;\omega_a,-\omega_a,\omega_b)\left|E(\omega_a)\right|^2 E(\omega_b) \end{aligned} \tag{2.11}$$

These particular expressions for nonlinear polarization can then be used in the wave propagation equation (Eq. 2.2) yielding

$$\nabla\times\nabla\times\mathbf{E} + \frac{1}{c^2}\frac{\partial^2\mathbf{E}}{\partial t^2} = -\mu_0\frac{\partial^2\mathbf{P}^{(3)}}{\partial t^2} \tag{2.12}$$

It is apparent that the nonlinear polarization term acts as a driving force for the considered electric field. In its absence we would have solutions in a form of free-propagating waves. For our case, we can write two propagation equations for the two inputs considered, which are coupled through the nonlinear polarization term. With some loss in generality which can be ignored for the purpose of our discussion, we can assume the input fields to have the form

$$E_i(z,t) = \frac{1}{2}\left(E_{0,i}(z)e^{j(k_i z-\omega_i t)} + c.c.\right) \tag{2.13}$$

where the index i corresponds to either input frequencies i.e $i = a,b$. Using this form in Eq. 2.12 we obtain

$$\frac{1}{2}\left[\left(\frac{\partial^2 E_{0,i}(z)}{\partial z^2}+2ik_i\frac{\partial E_{0,i}(z)}{\partial z}-{k_i}^2 E_{0,i}(z)+\frac{\varepsilon{\omega_i}^2}{c^2}E_{0,i}(z)\right)e^{j(k_i z-\omega_i t)}+c.c.\right]=-\mu_0\frac{\partial^2 P^{(3)}}{\partial t^2} \quad (2.14)$$

In general, the term containing the second derivative with *z* of the amplitude is neglected if the amplitude changes are very small over propagation distances of the order of the wavelength. This is called the *Slow Varying Envelope Approximation* (SVEA) [18]. We shall make use of this approximation and by selecting the terms driven at the frequencies of interest from the expression of the third-order nonlinear polarization we obtain the following general set of coupled equations

$$\frac{\partial E_{0,a}}{\partial z}=i\frac{\omega_a}{n_a c}\chi^{(3)}_{self}(\omega_a;\omega_a,-\omega_a,\omega_a)\left|E_{0,a}\right|^2E_{0,a}+i\frac{\omega_a}{n_a c}\chi^{(3)}_{cross}(\omega_a;\omega_b,-\omega_b,\omega_a)\left|E_{0,b}\right|^2E_{0,a} \quad (2.15)$$

$$\frac{\partial E_{0,b}}{\partial z}=i\frac{\omega_b}{n_b c}\chi^{(3)}_{self}(\omega_b;\omega_b,-\omega_b,\omega_b)\left|E_{0,b}\right|^2E_{0,b}+i\frac{\omega_a}{n_a c}\chi^{(3)}_{cross}(\omega_b;\omega_a,-\omega_a,\omega_b)\left|E_{0,a}\right|^2E_{0,b} \quad (2.16)$$

Here we used “self” and “cross” to designate the effects induced by the beams on themselves and the mutual interaction, respectively. We won’t give an explicit expression for these terms as in general they depend on material symmetry on the polarization of the input beam. Such expressions will be calculated however for zincblende structures in Chapter 7. Writing the complex fields in terms of real amplitudes $\rho_{a,b}(z)$ and phases $\varphi_{a,b}(z)$ we obtain

$$\frac{\partial\rho_a(z)}{\partial z}+i\rho_a(z)\frac{\partial\varphi_a(z)}{\partial z}=i\frac{\omega_a}{n_a c}\chi^{(3)}_{self}(\omega_a;\omega_a)\rho_a(z)^3+i\frac{\omega_a}{n_a c}\chi^{(3)}_{cross}(\omega_a;\omega_b)\rho_b(z)^2\rho_a(z) \quad (2.17)$$

$$\frac{\partial\rho_b(z)}{\partial z}+i\rho_b(z)\frac{\partial\varphi_b(z)}{\partial z}=i\frac{\omega_b}{n_b c}\chi^{(3)}_{self}(\omega_b;\omega_b)\rho_b(z)^3+i\frac{\omega_b}{n_b c}\chi^{(3)}_{cross}(\omega_b;\omega_a)\rho_a(z)^2\rho_b(z) \quad (2.18)$$

Writing explicitly the nonlinear susceptibilities as sums of real and complex numbers we find

$$\frac{\partial\rho_a(z)}{\partial z}=-\frac{\omega_a}{n_a c}\chi^{(3),I}_{self}(\omega_a;\omega_a)\rho_a(z)^3-\frac{\omega_a}{n_a c}\chi^{(3),I}_{cross}(\omega_a;\omega_b)\rho_b(z)^2\rho_a(z) \quad (2.19)$$

$$\frac{\partial \rho_b(z)}{\partial z} = -\frac{\omega_b}{n_b c}\chi^{(3),I}_{self}(\omega_b;\omega_b)\rho_b(z)^3 - \frac{\omega_b}{n_b c}\chi^{(3),I}_{cross}(\omega_b;\omega_a)\rho_a(z)^2\rho_b(z) \tag{2.20}$$

$$\frac{\partial \varphi_a(z)}{\partial z} = \frac{\omega_a}{n_a c}\chi^{(3),R}_{self}(\omega_a;\omega_a)\rho_a(z)^2 + i\frac{\omega_a}{n_a c}\chi^{(3),R}_{cross}(\omega_a;\omega_b)\rho_b(z)^2 \tag{2.21}$$

$$\frac{\partial \varphi_b(z)}{\partial z} = \frac{\omega_b}{n_b c}\chi^{(3),R}_{self}(\omega_b;\omega_b)\rho_b(z)^2 + i\frac{\omega_b}{n_b c}\chi^{(3),R}_{cross}(\omega_b;\omega_a)\rho_a(z)^2 \tag{2.22}$$

For the intensity effects considered, Eq. 2.19-2.22, describe in a basic form the self and mutual interaction of the two input fields. The decoupling of the amplitude and the phase allows for the determination of both the 2PA and nonlinear Kerr index coefficients for “self” and “cross” effects. Specifically, Eq.2.19 and 2.20 give the intensity variations for the beams, in a mutual interaction scenario which will be discussed further in Chapters 3, 5 and 7, when describing the pump-probe experiments. Eq. 2.21 and 2.22 express the cumulative effects in phase which are just proportional to the irradiances of the two interacting fields. They describe the self-phase modulation (SPM) and cross-phase modulation (XPM). These effects will be further discussed in Chapters 3 and 7.

The topic of Chapter 6 is the degenerate three-photon absorption (3PA) in zincblende structures. Following a similar approach we can write an equation for the variation of the amplitude related to the imaginary part of $\chi^{(5)}$ in the form

$$\frac{\partial \rho(z)}{\partial z} = -\frac{\omega}{nc}\chi^{(5),I}_{self}(\omega;\omega,-\omega,\omega,-\omega,\omega)\rho(z)^5 \tag{2.23}$$

which will be used in the analysis of the experimental Z-scan data.

For the specific case of direct-gap semiconductors, the bound electronic nonlinearities described in this section are associated with electronic transitions from a valence band to a conduction band when the frequencies involved are outside the linear absorption range. The

absorptive and refractive effects associated with the imaginary and real parts of $\chi^{(3)}$, respectively, are studied using these coupled equations while the "self" and "cross" coefficients are generally obtained through quantum mechanical calculations taking into account the specifics of transitions considered. For the absorptive effects such calculations will be detailed in Chapter 4.

2.2. Free-carrier effects

The transitions between electronic states lead to a redistribution of population between the participating levels. These population changes may induce by themselves absorptive and refractive effects which are proportional to the existing carrier densities. Let us consider the case of absorption over the bandgap in a semiconductor, when the energy difference between the final and the initial state is equal to the sum of the energies of at least two incident photons.

The changes in absorption at the incident frequency and the associated refractive effects can be analyzed using the formalism presented in the previous section. The transition results in a promotion of an electron in the conduction band and of a hole in the valence band. While in these states the carriers can still interact with the incident radiation. Electrons in the conduction band can further absorb the incident radiation (linearly and involving a phonon for momentum conservation) and move to a higher energetic state within the band. Similarly, the promoted holes in the heavy-hole band can be excited into a higher energetic state. If we consider for instance hole transitions between the light-hole and heavy-hole bands, these are direct transitions i.e. non-phonon assisted, and therefore more probable. The absorption will then be proportional to the densities of carriers in the initial states and the respective transition cross-sections. The carrier

densities depend nonlinearly on the incident intensities, with generation rates related to the particular multiphoton absorption process involved. In the same way, the change in index associated with n_2 will depend linearly on the input irradiance while the change in index associated with the free-carriers will depend linearly on the number of carriers at a given time.

Essentially, these processes are $\chi^{(1)}$ processes and can be described by standard classical models. Both absorption and refraction however depend on the photo-generated carrier densities and are nonlinear in the input irradiance. This is the reason why sometimes these consecutive $\chi^{(3)}:\chi^{(1)}$ effects give a behavior similar to $\chi^{(5)}$ effects. However, a clear separation of their nature can be made by looking at the characteristic times, as the population buildup follows an integral over the temporal shape of the incident pulse.

The absorptive and refractive effects of free-electrons can be calculated using a simple Drude-Lorentz model [19]. We write the equation of motion for a bound electron in an electric field using the Lorentz model

$$m\frac{d^2\mathbf{r}(t)}{dt^2}+m\Gamma\frac{d\mathbf{r}(t)}{dt}+m\omega_0^2\mathbf{r}(t)=-e\mathbf{E}(t) \tag{2.24}$$

where Γ is the damping parameter. Using the Fourier transform we obtain an equivalent equation in the frequency domain

$$\left(-m\omega^2-i\omega m\Gamma+m\omega_0^2\right)\mathbf{r}(\omega)=-e\mathbf{E}(\omega) \tag{2.25}$$

The displacement is then given by

$$\mathbf{r}(\omega)=\frac{-e}{m}\frac{\mathbf{E}(\omega)}{\left(\omega_0^2-\omega^2-i\omega\Gamma\right)} \tag{2.26}$$

We can write the dipole moment as

$$\mu(\omega)=-e\mathbf{r}(\omega)=\tilde{\alpha}(\omega)\mathbf{E}(\omega) \tag{2.27}$$

where $\tilde{\alpha}(\omega)$ is the polarizability tensor. Using the relation $\chi(\omega) = \frac{N\alpha(\omega)}{\varepsilon_0}$ we obtain the linear susceptibility

$$\chi(\omega) = \left(\frac{Ne^2}{\varepsilon_0 m}\right)\frac{1}{\omega_0^2 - \omega^2 - i\Gamma\omega} \tag{2.28}$$

For a free electron we can assume $\omega_0 = 0$ no resonance and writing ${\omega_p}^2 = \frac{Ne^2}{\varepsilon_0 m}$ we obtain

$$\chi(\omega) = \frac{{\omega_p}^2}{\omega_0^2 - \omega^2 - i\Gamma\omega} \tag{2.29}$$

where ω_p is the plasma frequency.

Using this model one can further obtain approximate expressions for the index of refraction and absorption assuming small damping due to electron collisions. Even though this treatment is very basic it gives some insight on the variation with the optical frequencies and this issue will be re-visited in Chapter 7.

CHAPTER 3: PARAMETRIC DEVICES FOR NONLINEAR MATERIAL CHARACTERIZATION AND EXPERIMENTAL TECHNIQUES

Most of the experiments described in this work were carried out using picosecond and femtosecond light sources. Frequency doubling, sum frequency generation (SFG), parametric conversion and amplification, and difference frequency generation (DFG) were routinely employed to generate the diverse wavelengths used in our nonlinear experiments. The laser systems used consisted basically of a main source (laser with either ~30 picoseconds or ~140 femtoseconds pulse duration) pumping one or two tunable devices, which in our case were based on optical parametric generation and amplification (OPG/OPA) followed by a DFG process to produce the mid-IR pulse required for some of the experiments.

To characterize the linear properties of our materials we used a combination of measurements carried out with a Carry spectrophotometer for the visible and near-IR ranges and Fourier Transform Infrared Spectroscopy (FTIR) for wavelengths in the mid-IR. To determine or confirm particular sample orientations we used X-ray diffraction experiments.

In this chapter, the devices used will be described in some detail along with the typical experimental techniques, stressing the type of information that can be extracted using each one of these techniques.

3.1. Laser systems and parametric devices

3.1.1. Picosecond laser

The laser used in our picoseconds experiments was an EKSPLA PL-2143 Nd:YAG laser operating at 1064 nm, operating at 10 Hz. It is a regenerative amplified laser system which

produces about 110 mJ pulses with a duration of ~30 ps (FWHM). The general layout is shown in Fig 3.1. The oscillator part consists of a main cavity and a regenerative cavity. Mode-locking is achieved both actively, by driving the voltage on Pockels cell PC1 and passively using a solution of dye in ethanol, acting as a saturable absorber. The duration of the pulse train in the main cavity is in the range of 6 to 10 μs. An important process controlling the amplitude and the

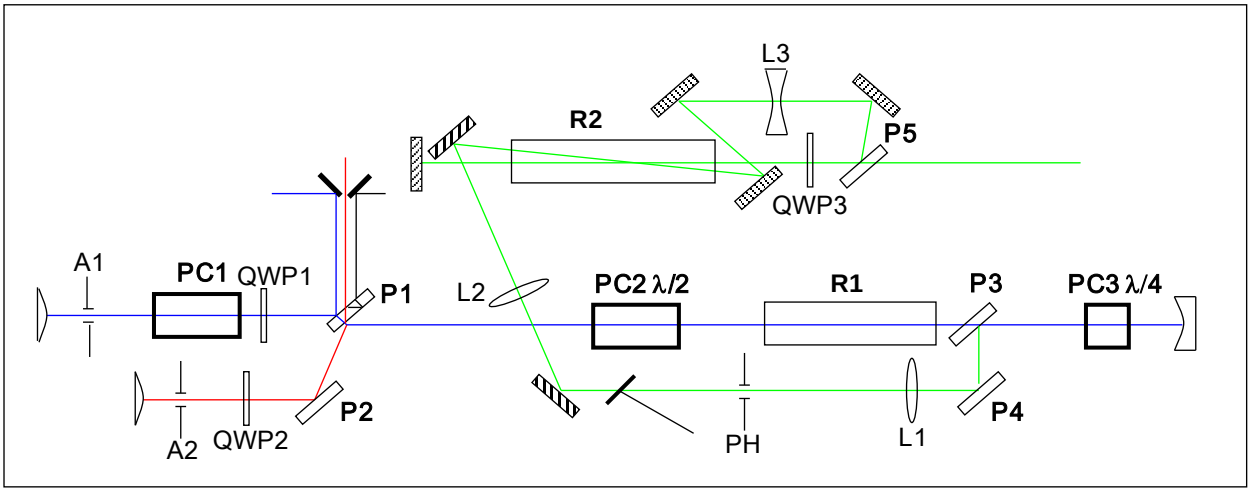

Figure 3.1 Layout of the picosecond Nd:YAG laser. PC-Pockels cell, P-thin film polarizer, A-aperture, L-lens, PH-pinhole, QWP-quarter-wave plate, R-Nd:YAG rod.

stability of the train is the negative feedback loop. Part of the light in the cavity is taken out using a prism and guided through a fiber to a detector. The information on the amplitude is then conveyed to PC1 which adjusts through the voltage applied the losses in the cavity. This way the amplitude of pulses in the train is kept low and fairly constant. The goals here are to obtain a train long and stable and with a reasonably low amplitude to not significantly deplete the gain in the YAG rod which could lengthen the pulse. After a set time the pulse is switched to the regenerative cavity using PC2 to rotate its polarization by 90 degrees. The thin film polarizer then acts as a mirror reflecting the pulse which consequently is allowed to travel a set number of times (modifiable using a pulse selector) through the gain medium until it reaches maximum

amplification. The pulse switched out from the regenerative cavity is however allowed one extra trip through the rod. Even though the gain is saturated at that point, this is done in order to insure a minimal energy variation from shot to shot.

After being taken out from the regenerative cavity the pulse goes through a spatial filtering system which effectively insures that only a TEM_{00} mode is present. The amplification stage is done using three passes through the pumped amplifier rod, in a slightly divergent geometry in order to take full advantage of the larger size of the amplifier rod. In this stage the energy in the pulse is increased from about 500 μJ to as much as 110 mJ. Different levels of amplification are obtained by setting different delays between the arrival of the pulse and the firing time for the flash lamps. The amplifier chamber has a specific design to allow turbulent flow of the cooling water in order to avoid any temperature gradients which would cause thermal lensing and deterioration of the desired beam profile.

3.1.2. Picosecond OPG/OPA and DFG

In order to pump the parametric devices, the 1064 nm beam from the laser needs to be converted to 355 nm. The wavelength conversion is done using two K*DP (KD_2PO_4) crystals, by doubling to 532 nm and then adding residual 1064 nm through SFG. Originally, the crystals were placed right after the amplifier. The irregularities in the fundamental profile (consisting mainly of high frequency spatial components) were further amplified such that upon focusing the 355 nm beam onto the parametric crystal a highly modulated distribution was created (hot spots) which was negatively affecting the generated beam profiles and limiting the pumping energies to avoid crystal damage. Several attempts were made to alleviate the problem and as a final

solution, a spatial filtering setup for the 1064 nm beam was built outside the laser. The laser beam was focused using long focal length lenses in a glass tube under vacuum. The vacuum is monitored on a daily basis with a continuously run vacuum pump and attached gauge. The ends of the tube had AR coating for 1064 nm and the pinhole inside the tube, of 500 μm in diameter, was made out of a highly resistant ceramic and later replaced by a diamond one.

The spatially filtered 1064 nm beam enters then the harmonic unit box containing the K*DP crystals and a few separating optics producing five output beams, two each at the fundamental and the 3rd harmonic frequencies for pumping the two parametric devices, with a fifth one at 532 nm, having an energy of about 1 mJ.

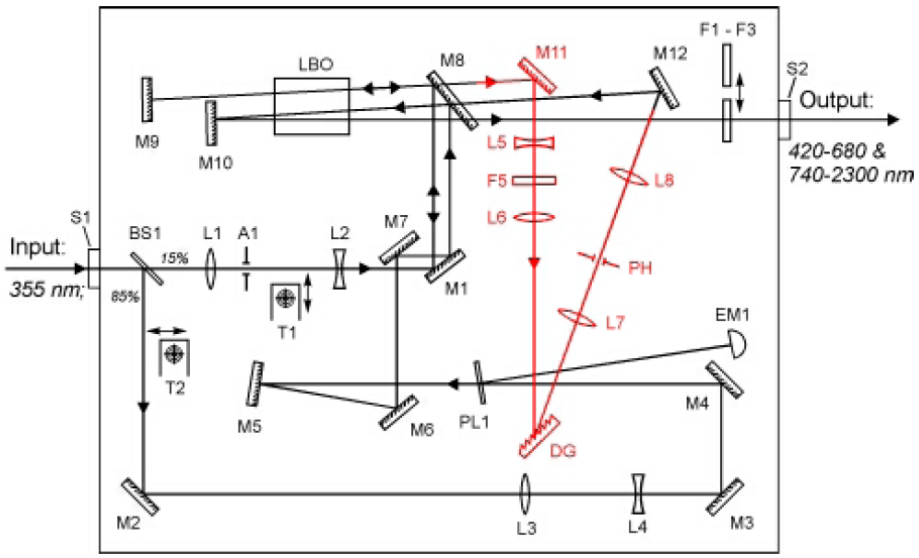

Figure 3.2 Layout of the picosecond OPG/OPA and DFG system.

The two parametric devices are almost identical with a few minor differences related to the seeding wavelengths and the type of DFG crystal used, which will be discussed in the next paragraphs. The 355 nm pump is split in two beams at the entrance, with very different energies, as seen in the Fig. 3.2. The weaker beam (about 20% of the total energy) is resized with a

telescope and clipped by a large aperture (in order to create an almost flat-top beam) before being focused onto the LBO (Lithium Tri-Borate) crystal. The mirror behind the crystal assures a double pass and the parametrically generated beams are further modified to construct the seed beam for the amplification process. The initial parametric signal is passed through a band pass filter which selects either the signal or the idler to be used for amplification. Then the seed beam is reflected off a diffraction grating and passed through a telescope with a pinhole, effectively

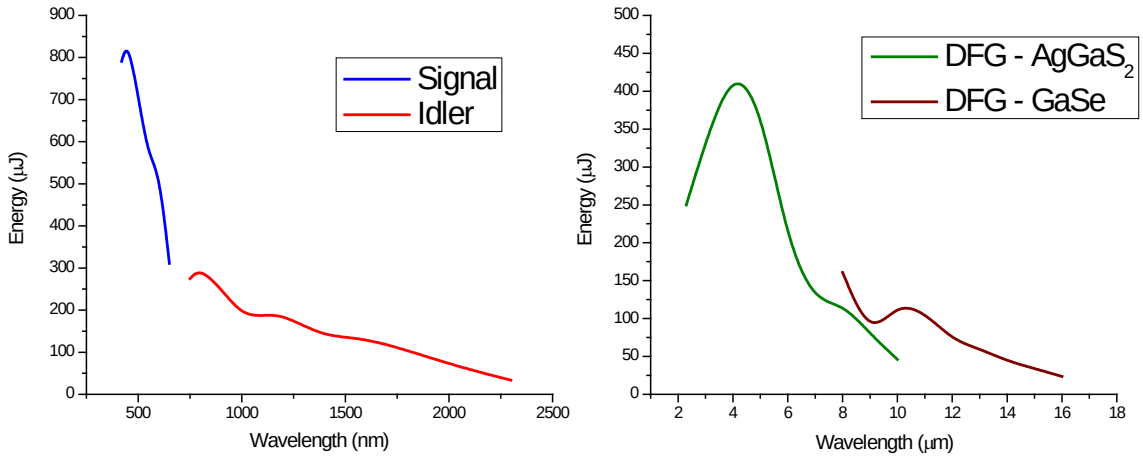

Figure 3.3 Tunable range for the picosecond parametric system.

producing the right spatial distribution with the right spectral width. This seed then travels at the same time through the crystal as the stronger 355 nm beam (delayed and reshaped appropriately), is amplified, again in two passes, and the output wavelength is in the end selected using a set of band pass filters, picking either the amplified signal or idler. The tunability range of the system is from 420 nm up to 2.3 μm, with a small gap between 680 nm and 740 nm, around the degeneracy point and is shown in Fig. 3.3.

The mid-IR wavelengths are generated through a DFG process using the idler (approximately from 1100 nm to 1150 nm) and part of the fundamental beam. Two different

crystals are used in the two devices, $AgGaS_2$ and GaSe, giving a tunable range from 2.3 μm to 11.5 μm and from 8 μm to 18 μm, respectively. Typical beam profiles prior to spatial filtering are shown in Fig. 3.4.

Figure 3.4 Typical beam profiles for signal, idler and DFG beams. The wavelengths shown are (a) 500 nm, (b) 1100 nm, (c) 10 μm and (d) 12 μm. The mid-IR wavelengths are produced in the GaSe crystal.

3.1.3. Femtosecond laser

The femtosecond laser used for experiments is a Clark CPA-2210 system. The oscillator is an Erbium doped fiber ring laser, pumped by a diode laser at 980 nm, operating at the 1550 nm and at a 27 MHz repetition rate. Using a PPLN (periodically poled Lithium Niobate) crystal the radiation is converted into its 2nd harmonic at 775 nm. The output (seed) is sent to a stretcher, which consists of a reflecting diffraction grating, spreading the pulse in time before the amplification process in order to lower the peak power level and to prevent damage of the gain medium and optical components. An electro-optic modulator (Pockels cell) allows a single pulse to enter the amplifier cavity, shown in Fig. 3.5. The gain medium is Ti:Sapphire (Titanium doped Al_2O_3) and it is pumped by a Q-Switched, frequency doubled Nd:YAG laser operating at 532 nm and 1kHz repetition rate. The amplification takes place through tens of passes through the

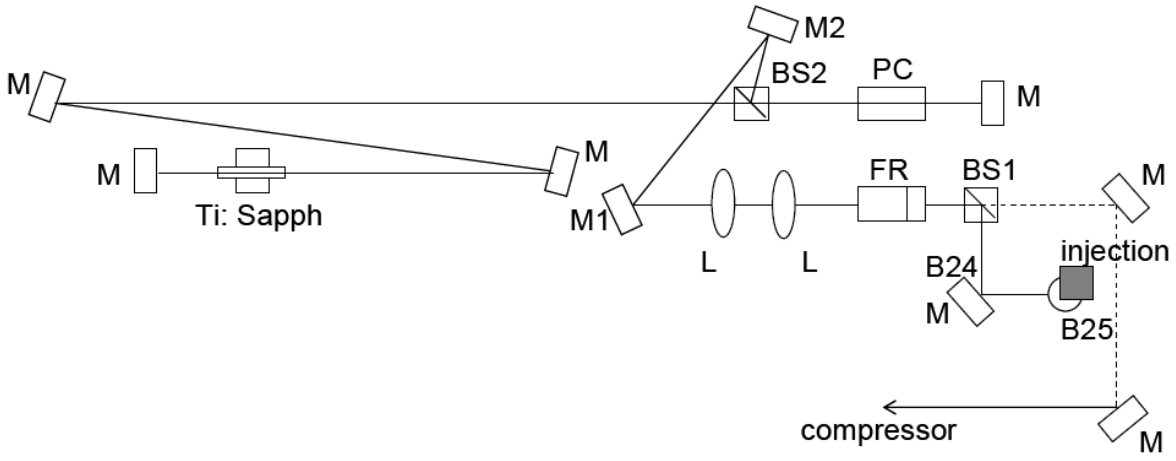

Figure3.5 Layout of the Ti:Sapphire amplifier. L-lens, BS-beamsplitter, PC-pockels cell, FR-Faraday rotator.

Ti:Sapphire crystal, extracting the stored energy. Once the energy in the cavity approaches the mJ level, the same Pockels cell is used to switch the pulse out of the cavity. This switching is accomplished as in the case of the previously described system by rotation of the pulse

polarization in conjunction with a polarizing beamsplitter. The pulse is then compressed using a transmission grating in four passes. This process in which a short pulse is first stretched then amplified and finally compressed to achieve large amplification levels is called Chirped Pulse Amplification (CPA). The total output is about 1.7 mJ per pulse at a 1 kHz repetition rate having a duration of about 140 fs (FWHM).

3.1.4. Femtosecond OPG/OPA and DFG

The parametric device used in our femtosecond experiments is a TOPAS 800 model produced by Light Conversion. It is a little bit different from the picosecond one described above in the sense that five total passes through the BBO (Beta-BaB_2O_4) nonlinear crystal are required (see Fig. 3.6). The first stage consists of generation of a superfluorescence signal (SFL) while the

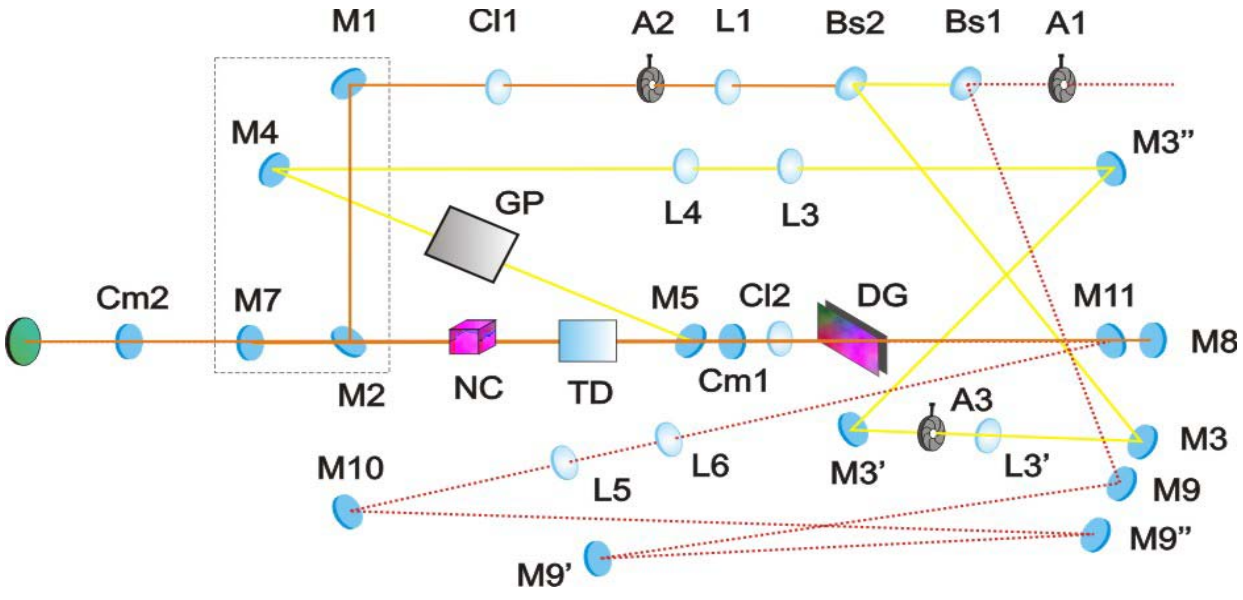

Figure 3.6 Femtosecond TOPAS layout in horizontal plane.

consequent stages consist of parametric amplification processes in the BBO crystal. The initially generated SFL serves a broadband seed. The incoming pump beam is separated in three

components using beamsplitters. The SFL produced in the first pass is amplified in the second pass. To reduce the spectral width and to stabilize its shape, a diffraction grating is used between the pre-amplification stages. After the third pass, during which the amplification is minimal, the beam is reflected by the diffraction grating. In the fourth pass, only a part of the spectrum of the diffracted seed beam will be amplified, such that the amplified seed will follow the divergence characteristics of the pump beam. Basically, the role of the grating is to narrow the spectrum of the amplified signal, while separating spatially the beams present and making tuning more precise.

The wavelength selection is achieved by rotating the nonlinear crystal in the phase matching plane. The inherent displacement is adjusted by using a small quartz compensating plate. All the movements of the crystals, grating and optical delay lines are driven by stepper motors controlled through the TOPAS software. Finally, the bulk of the pump energy goes a fifth pass through the BBO crystal together with a pre-amplified seed having a similar size, thus achieving the maximum amplification in a collinear geometry.

TOPAS uses a type II phase matching which produces narrow bandwidth gains suitable for the generation of femtosecond pulses close to transform limited. Here, there is no full degeneracy so that there is no increase in bandwidth when signal and idler approach similar frequencies while still separating them by taking advantage of their orthogonal polarizations.

3.2. Techniques for nonlinear materials' characterization

The experimental work described in this dissertation used either single beam techniques (Z-scan) or time resolved excite-probe experiments in frequency degenerate and non-degenerate

configurations. By performing Z-scans one can obtain information on both nonlinear amplitude and phase, whether they are related to the real and imaginary part of the respective nonlinear susceptibilities or to the free carrier effects which dominate in most of experiments performed with picoseconds pulses in InSb. The two-beam experiments described were aimed mostly at quantifying the absorptive effects and the lifetimes of the processes studied, dealing with either or both the imaginary part of $\chi^{(3)}$ or the free-carrier effects. The following sections are aimed at describing these nonlinear characterization techniques in detail and discus the type of information that can be extracted from these experiments.

3.2.1. The Z-scan technique

The Z-scan was developed in 1990 by Sheik-Bahae and co-authors [20] and it's a simple way of characterizing both the amplitude and the phase changes that an intense optical beam would experience when propagating in nonlinear media. This single beam technique is generally used to measure either or both the real and imaginary parts of the $\chi^{(3)}$ coefficient, but it is also extremely useful for cases when higher order nonlinearities are present as well.

It is well known that the strength of the nonlinear interaction varies with the irradiance of the electric field. Therefore, one can extract the magnitudes of the nonlinear coefficients of interest by studying the dependence of the nonlinear effect as a function of the incident irradiance. A simple approach is to use a focusing geometry (see Fig. 3.7 (a)) and translate a sample of the material studied along the propagation direction of the beam through the focal point. The output beam energy is then measured in the far field using a detector. If all the energy is collected one can get full information on the absorptive effects present in the sample (2PA,

3PA, FCA, ESA, etc.) and the transmittance curve, measured as a function of position, will show a dip at the focus for nonlinear loss or a peak for saturation effects. However, if the beam is apertured in the far field, the nonlinear phase acquired isn't averaged out anymore and integration of the signal over the aperture area yields a result which depends on the sample position. This happens since upon propagation the phase variations are coupled into amplitude variations at the aperture plane through diffraction. If we have no absorptive effects in the sample, we can associate the induced change in index with the creation of a nonlinear lens of variable focal length. For example, in the case of a positive Kerr index coefficient (n_2) a positive lens would be created both before and after the focus. If the lens would be placed before the focus the net effect would be an increase of the size of the beam in the far field consequently reducing the amount of energy collected through the aperture. For a lens placed after the focus we would have a decreased size at the aperture and an increase of the signal measured. This explains the shape of the signal, dip followed by a peak, as shown in Fig. 3.7 b.

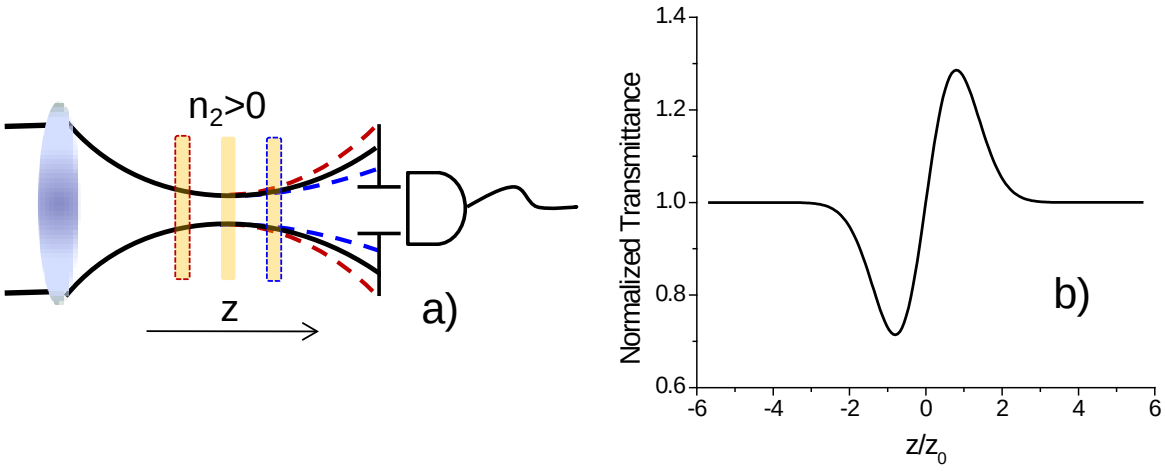

Figure 3.7 Typical Z-scan setup. (a) Divergence of beam in the far field for multiple sample positions with $n_2>0$ and the corresponding (b) normalized transmittance at the detector.

A quantitative analysis can be done for such experiments. There are, however, two assumptions that can greatly simplify the calculations without affecting the generality of the problem. They are known as the “thin sample” approximations, linear and nonlinear. The “linear" approximation is that $L<<z_0$, where L is the sample thickness, and z_0 is the Rayleigh range or confocal parameter within the sample. This basically states that the sample is thin enough that, for no nonlinear effects, the beam maintains a constant size when propagating through the sample. The “nonlinear” approximation is that $L<< z_0/\Delta\Phi(0)$ where $\Delta\Phi(0)$ is the maximum nonlinear phase shift. The assumption here is that the nonlinear phase shift is small enough to not affect the beam size (and irradiance) during propagation through the sample. When measuring small phase shifts, the second condition is satisfied automatically. Within the range of validity of these assumptions, using the SVEA, one can effectively decouple the refractive effects from the absorptive ones and use the following set of coupled equations [20]

$$\frac{dI}{dz'} = -\alpha(I)I \tag{3.2}$$

Assuming a TEM_{00} Gaussian beam, one can write the electric field as

$$E(z,r,t) = E_0(t)\frac{w_o}{w(z)}\exp\left(-\frac{r^2}{w^2(z)} - \frac{ikr^2}{2R(z)}\right) \tag{3.3}$$

where we ignore all phase factors uniform in r. For the case when only third-order nonlinearities are present we can calculate both the nonlinear phase and the amplitude change after propagation through the sample and we write the electric field exiting the sample as [20]

$$E_e(z,r,t) = E(z,r,t)e^{-\frac{\alpha L}{2}}(1+\beta I(z,r,t)L_{eff})^{\left(\frac{ikn_2}{\beta}-\frac{1}{2}\right)} \tag{3.4}$$

where $L_{eff} = (1 - e^{-\alpha L})/\alpha$, α is the linear absorption coefficient (m^{-1}), β is the 2PA coefficient (m/W), n_2 is the Kerr coefficient or nonlinear refractive index (m^2/W) and k is the wavevector in the medium (m^{-1}). The electric field can then be propagated to the aperture plane and integrated in modulus squared over the area of the aperture to give the transmitted energy.

In the case of pure refractive or absorptive effects simple analytic expressions can be obtained, propagating the complex phase to the aperture plane using a Gaussian decomposition method [21]. Also, for small signals the refractive effects can be separated by division of the closed aperture curve to the open aperture one rendering these simple expressions extremely useful.

By analyzing the Z-scan curves, one can gain some insight that can be used to qualitatively interpret the experimental data. For example, in the case of pure refractive effects $\chi^{(3)}$ and thin samples, it can be shown that the distance between the positions of the peak and the dip depends only on the confocal parameter z_0, while the difference between the maximum and the minimum normalized transmittances is directly proportional to n_2 and the peak irradiance. The same analysis can be done for the case of pure absorptive effects, where the width of 2PA and 3PA curves can be shown to be proportional to the confocal parameter, with different proportionality coefficients. These observations are very useful, particularly when several nonlinearities are present. For instance, just by analyzing the widths of the curves one can differentiate between 2PA and 3PA or between a pure 2PA process and a 2PA process followed by ESA or FCA for the case of semiconductors. However, it can be difficult to differentiate between 3PA and 2PA produced ESA without additional information from, for example, pump-probe data. Similarly, pure n_2 effects can be separated from an additional FCR with population generated through 2PA,

by plotting the maximum change in transmittance divided by the input irradiance. This can yield good estimates for the magnitude of refractive carrier effects for small signals. As a general rule, higher order effects tend to narrow the curves and such differentiations can simplify things very much.

In practice however, an easy separation of the refractive effects from the absorptive ones or of different order nonlinearities is usually hard to accomplish just by analyzing single beam experiments data. As it will be seen in Chapter 5 large absorptive effects can complicate greatly the analysis. Therefore, numerical simulations to account exactly for all effects present are useful. In this work, a Matlab beam propagation code in the "thin sample" approximation was utilized to quantitatively analyze the Z-scan data and extract the parameters of interest such as 2PA and 3PA coefficients, Kerr index coefficient and refractive and absorptive carrier cross-sections. The initial phase and amplitude distribution is sampled for the incident beam at each Z-scan position, in the radial direction. Temporal sampling is then used in conjunction with the nonlinear parameters (n_2, β, FCA, FCR) to calculate the distribution of the complex amplitude of the field exiting the sample and the photo-generated carrier population distribution within the sample. Given the assumed cylindrical symmetry, the complex field is then propagated using a Hankel transform to the detector plane. Finally, the transmitted energy is calculated using the complex field distribution by either doing a full integration over the spatial domain, to determine the absorptive effects, or over the aperture size only, to compute both the absorptive and the refractive effects.

3.2.2. The pump-probe technique

As discussed in Chapter 2, the nonlinearly induced polarization acts as a driving term for all fields present, inducing changes of various magnitudes that can be separately monitored. A strong beam (pump) will affect the medium in which it propagates and then the changes in its properties can be monitored via a weak beam (probe) which by itself isn't able to produce a comparable effect. If we consider the case of two optical pulses propagating in a medium, by controlling their separation in time, one can study both the instantaneous (for some temporal overlap) and long lived effects (for a trailing probe pulse). This is extremely important since adding a temporal dimension to the problem can reveal new information. The limiting factor here is given by the duration of the measuring tool (pulse) as compared to how fast the studied physical process is. Short pulses can therefore produce "snapshots" of the temporal evolution on a system affected by a perturbation until a steady-state is reached.

In the experiments presented in this work, the pump-probe technique was solely utilized to quantify the absorptive effects, specifically non-degenerate 2PA processes for cases when the self-effects were either not present or extremely weak (Chapter 5) or to help separate and monitor the bound electronic effects from the longer lived free-carrier effects (Chapter 7).

For the case of $\chi^{(3)}$ nonlinearities of interest for this work are the nonlinear polarization terms related to an intensity dependent absorption and refraction. A simple analysis can be made considering two different input frequencies, an "excite" (or "pump") frequency ω_e and a "probe" frequency ω_p. The intensity dependent terms are $|E_e|^2 E_e$, $|E_p|^2 E_p$, $|E_e|^2 E_p$ and $|E_p|^2 E_e$. The first two terms are responsible for "self" effects (degenerate 2PA and self-phase modulation), while the last two correspond to the "cross" effects (non-degenerate 2PA and cross-phase modulation).

Considering now only the absorption, from the wave equation under SVEA we obtain the following coupled equations

$$\frac{dI_e(z)}{dz} = -\alpha_2(\omega_e,\omega_e)I_e(z)^2 - \alpha_2(\omega_e,\omega_p)I_e(z)I_p(z) \tag{3.5}$$

$$\frac{dI_p(z)}{dz} = -\alpha_2(\omega_p,\omega_p)I_p(z)^2 - \alpha_2(\omega_p,\omega_e)I_p(z)I_e(z) \tag{3.6}$$

where the 2PA coefficients shown have the following expressions for the case of co-polarized fields

$$\alpha_2(\omega_e,\omega_e) = \frac{3\omega_e}{2n_e^2\varepsilon_0 c^2}\chi^{(3)}_{I,xxxx}(-\omega_e;\omega_e,-\omega_e,\omega_e) \tag{3.7}$$

$$\alpha_2(\omega_p,\omega_p) = \frac{3\omega_p}{2n_p^2\varepsilon_0 c^2}\chi^{(3)}_{I,xxxx}(-\omega_p;\omega_p,-\omega_p,\omega_p) \tag{3.8}$$

$$\alpha_2(\omega_e,\omega_p) = \frac{3\omega_e}{n_e n_p\varepsilon_0 c^2}\chi^{(3)}_{I,xxxx}(-\omega_e;\omega_e,-\omega_p,\omega_p) \tag{3.9}$$

$$\alpha_2(\omega_p,\omega_e) = \frac{3\omega_p}{n_e n_p\varepsilon_0 c^2}\chi^{(3)}_{I,xxxx}(-\omega_p;\omega_p,-\omega_e,\omega_e) \tag{3.10}$$

As a side note, as it will be explicitly shown in Chapter 7, these expressions for the 2PA coefficients are generally more complicated for non-isotropic media as they depend on material symmetry and the mutual polarizations of the interacting fields. The first terms in Eq. 3.5 and 3.6 correspond to the situation when the two absorbed photons are from the same beam (degenerate 2PA), while the second terms correspond to the absorption of one photon from each beam (non-degenerate 2PA). For the case of a weak probe beam we can ignore the first term in Eq. 3.6 allowing us to describe the loss experienced by the probe beam in the following manner

$$\frac{dI_p(z)}{dz} = \alpha_{eff} I_p(z) \tag{3.11}$$

where the "effective" absorption coefficient depends on the non-degenerate 2PA coefficient at the probe frequency and the pump irradiance. By delaying the probe pulse with respect to the pump pulse the absorption of the probe beam will follow the temporal profile of the pump beam.

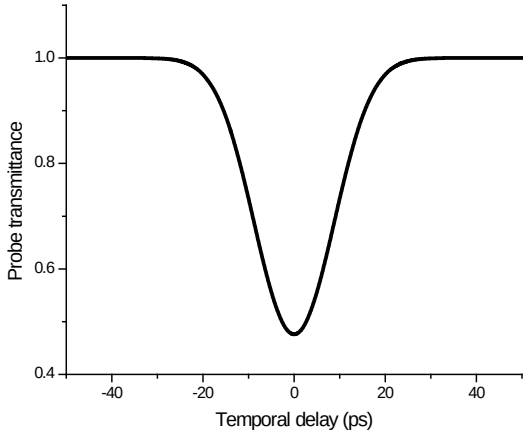

Figure 3.8 Calculated pump-probe curve with pure 2PA.

The detected signal is however the result of the integration over the temporal profile of the probe pulse and when plotted as a function of the temporal delay will basically yield a cross-correlation function with a width which depends on the two pulsewidths and an amplitude given by the pump irradiance and the non-degenerate 2PA coefficient (see Fig. 3.8), of interest in experiments described in Chapter 7. This curve assumes minimal group velocity dispersion (GVD) effects (see Chapter 5) or frequencies close to degeneracy. When the frequencies are highly non-degenerate the curve will be distorted and this situation will also be discussed in detail in Chapter 5.

The effects mentioned in previous paragraphs are accurately describing situations where only instantaneous or bound electronic effects are present. This is not the case in general when

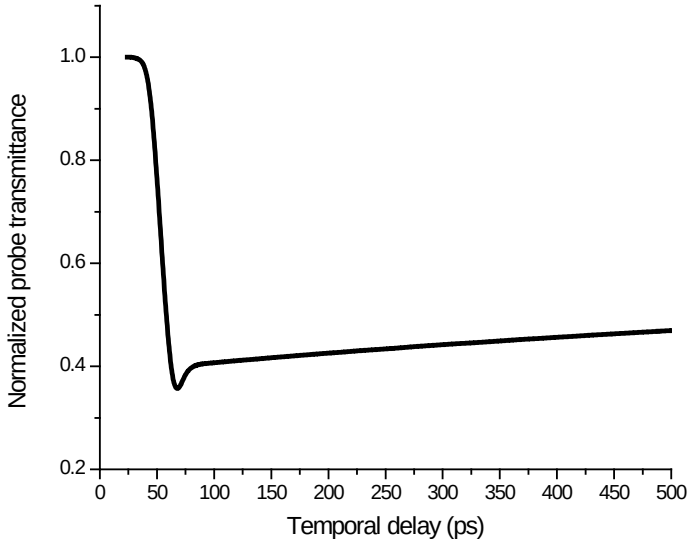

Figure 3.9 Calculated pump-probe curve for 2PA and carrier effects (FCA and Auger recombination).

the generation of excited states, the byproduct of 2PA, plays an important role. For semiconductors, the absorption of two photons is coupled with the promotion of an electron from the valence band to the conduction band or, equivalently, the promotion of a hole to the valence band. These photo-generated free carriers also absorb the incident light, with an “effective” absorption coefficient and lifetime which depend on their density. It will be shown, based on the frequency degenerate 2PA experiments presented in Chapter 7, that the transmittance of the probe is influenced by both FCA and 2PA over the temporal overlap of the two pulses. At much larger delays (~ 1 ns), the experiment gives complete information on the carrier dynamics, strongly influenced by the Auger recombination process at large photo-generated carrier

densities. A theoretically calculated curve for a pump-probe experiment in InSb is shown in Fig. 3.9, showing a complex time dependence of the probe transmittance.

CHAPTER 4: MODELS FOR CALCULATING MULTIPHOTON ABSORPTION IN SEMICONDUCTORS

It is well known that experimental advances allow for refining any existing theories or push towards developing new ones. The reverse is also true. Some theoretical analyses may yield results that cannot be immediately verified and in turn stimulate experimental work and lead to perfecting of the experimental methods. Connecting the theoretical treatments with experimental data allows for significant advances in the way we understand physical problems.

Experimental investigation of multiphoton processes had to practically wait for the invention of the laser. The foundations of the theoretical methods used for calculations were laid before, but the lack of experimental results, or the large uncertainties in their validity, produced a plethora of predictions, with very different degrees of accuracy. Fortunately, the advances in the development of highly tunable laser sources with intense and short pulses helped settle disagreements and better the understanding level for the phenomena investigated.

In this chapter the main theoretical approaches to calculating multiphoton absorption rates in semiconductors will be reviewed. A discussion on the accuracy level (expected and verified) and the possibility of extending the analysis to more complex models and/or higher order nonlinearities will be made.

4.1. Electron-field interaction

The phenomena described in this work relates almost exclusively to the interaction of physical systems with intense incident fields. In a general sense, the behavior of a complex system, crystalline solid and external electromagnetic field, for instance, is dictated by the

characteristics of the constituent parts and their interaction. We can therefore assume that the Hamiltonian for the total system of radiation plus atom can be written as a sum of three terms[]. It includes the Hamiltonian for the material, with given eigenstates and eigenvalues, a Hamiltonian for the radiation field, and an interaction Hamiltonian, assumed to be weak enough [8]Hamiltonian for the electron in an electromagnetic field can be written as [22]

$$H = \frac{1}{2m}(\mathbf{p} + \frac{e}{c}\mathbf{A}(\mathbf{r},t))^2 - e\phi(\mathbf{r},t) + V_0(\mathbf{r}) = H_0 + \frac{e}{2mc}\left[\mathbf{p}\cdot\mathbf{A} + \mathbf{A}\cdot\mathbf{p}\right] + \frac{e^2A^2}{2mc^2} - e\phi(\mathbf{r},t) \quad (4.1)$$

where H_0 is the unperturbed electron Hamiltonian and $\mathbf{A}(\mathbf{r},t)$ and $\phi(\mathbf{r},t)$ are the magnetic write the interaction Hamiltonian as

$$H_{\text{int}} = \frac{e}{2mc}(2\mathbf{A}\cdot\mathbf{p} - i\hbar\nabla\cdot\mathbf{A}) + \frac{e^2A^2}{2mc^2} - e\phi(\mathbf{r},t) \quad .(4.2)$$

For radiation with no electrostatic source $\phi(\mathbf{r},t) = 0$ and in the Coulomb gauge $\nabla\cdot\mathbf{A} = 0$. The term containing the square of the field can be ignored in the expression of the interaction Hamiltonian since it won't have contributions when calculating the transition matrix elements [8, 22]. However, it does modify the energy of the states through the so-called ponderomotive energy as will be shown later on. Thus the form of the electron-field Hamiltonian interaction is given by

$$H_{\text{int}} = \frac{e}{mc}\mathbf{A}\cdot\mathbf{p} \quad (4.3)$$

For a specific system, this expression allows for the calculation of the transition rates when the system is perturbed by H_{int}, given that the full description in terms of eigenstates and eigenvalues is known for the unperturbed system.

4.2. Perturbation approach

Let us assume the case of an n level system described by the Hamiltonian H_0 such that $H_0|\Psi_n\rangle = E_n|\Psi_n\rangle$, where E_n and $|\Psi_n\rangle$ are the known eigenvalues and eigenstates. Any general initial state can be written as a linear superposition in the form $|\Psi\rangle = \sum_n c_n|\Psi_n\rangle$. The time-dependent Schrödinger equation allows us to predict the temporal evolution of the system such that after time *t* the system will be in a state defined by

$$|\Psi(t)\rangle = \sum_n c_n|\Psi_n\rangle e^{-iE_n t/\hbar} \tag{4.4}$$

If a time dependent small perturbation $\lambda H'(t)$ is present then the coefficients acquire a time dependence and we can express the new state in the following form

$$|\Psi'(t)\rangle = \sum_n c_n(t)|\Psi_n\rangle e^{-iE_n t/\hbar} \tag{4.5}$$

such that Schrödinger's equation is again satisfied

$$i\hbar\frac{\partial|\Psi'(t)\rangle}{\partial t} = (H_0 + \lambda H'(t))|\Psi'(t)\rangle \tag{4.6}$$

Using the fact that $|\Psi_n\rangle$ are the eigenfunctions of the H_0 operator we obtain

$$i\hbar\sum_n \frac{dc_n(t)}{dt}|\Psi_n\rangle e^{-iE_n t/\hbar} = \lambda H'(t)\sum_n c_n|\Psi_n\rangle e^{-iE_n t/\hbar} \tag{4.7}$$

Taking the inner product with $\langle\Psi_m|e^{iE_m t/\hbar}$ we find

$$i\hbar\frac{dc_m(t)}{dt} = \lambda\sum_n \langle\Psi_m|H'|\Psi_n\rangle c_n e^{i(E_m - E_n)t/\hbar} \tag{4.9}$$

This allows us to calculate the probability of finding the system in state *m* after a time *t* by calculating $|c_m(t)|^2$ using a set of matrix elements. Eq. 4.9 allows for finding of an accurate solution for the time-dependent wavefunction, which is a complicated problem for a large number of eigenstates. In order to simplify it, the coefficients c_m are expanded into a power series of λ as $c_m = c_m^0 + \lambda c_m^{'} + \lambda^2 c_m^{''} + ...$, where the primed coefficients shown here are the first and second-order corrections. Using this expansion in Eq.4.9 and equating all the terms having the same power in λ we can obtain the first order correction by using the 0^{th}-order correction (time-independent or steady-state solutions) and the respective matrix elements. The second-order correction will be calculated via the the 0^{th} and 1^{st} order corrections and will therefore have products of two matrix elements and so on.

At this point we will avoid a more detailed analysis, unnecessary for our general goal, and we shall restrict ourselves to just identifying the correlations to the situation of a harmonic perturbation, like the case of an electromagnetic field of interest to us. For this case, the first order correction gives Fermi's Golden Rule which expresses the transition rate between two states as a function of the matrix element of the interaction Hamiltonian. Following the same analogy, in general, the n^{th}-order correction will allow the calculation of the *n*-photon absorption rate. For example, in the case of a perturbing field of frequency ω, the degenerate 2PA and 3PA rates can be calculated according to

$$W_{2PA}^{if} = \frac{2\pi}{\hbar}\sum_n \frac{\langle \Psi_f | H_{\text{int}} | \Psi_n \rangle \langle \Psi_n | H_{\text{int}} | \Psi_i \rangle}{(E_n - E_i) - \hbar\omega} \delta(E_f - E_i - 2\hbar\omega) \tag{4.10}$$

$$W_{3PA}^{if} = \frac{2\pi}{\hbar}\sum_n \sum_m \frac{\langle \Psi_f | H_{\text{int}} | \Psi_n \rangle \langle \Psi_n | H_{\text{int}} | \Psi_m \rangle \langle \Psi_m | H_{\text{int}} | \Psi_i \rangle}{[(E_n - E_i) - 2\hbar\omega][(E_m - E_i) - \hbar\omega]} \delta(E_f - E_i - 3\hbar\omega) \tag{4.11}$$

For the case of semiconductors, these calculations are fairly straight-forward. The main issue here is how well described are the steady state solutions for the wavefunctions of the unperturbed states. As it will be seen in Chapters 5 and 6, using complex models such as Kane's 4-band model [23] can produce very good results for non-degenerate 2PA and degenerate 3PA. An even more general model, consisting of 7 bands (4 conduction and 3 valence) was successfully used for the calculation of anisotropy of the $\chi^{(3)}$ tensor related to the pure absorptive (2PA) and refractive (n_2) effects [24, 25]. For much simpler cases, the use of such involved models can be avoided. For 2PA, a 2-parabolic band model can give fairly good agreement with experiment [8].

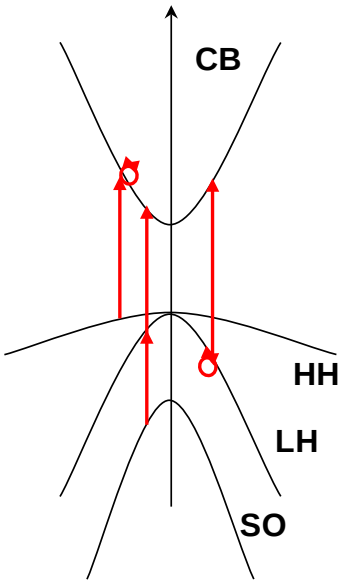

Figure 4.1 Diagram showing possible paths for the two-photon transitions when considering a 4-band structure. Circles denote "self" transitions and the direct arrows denote direct inter-band transitions.

In the case of such simple models however, the issue is the correct estimation of the magnitude of the matrix elements associated to the intra-band or self-transitions, transitions between states in the same band (see Fig. 4.1). These elements were in general taken to have the form

$p_{ii} = m\hbar k / m_i$ where the i corresponds to either the conduction or the valence band and this approach was the most common one for the early calculations, regardless of the number of bands used in the model [26]. As will be seen in Chapter 6, these types of transitions depend on band mixing (forbidden for the unmixed states) and great care needs to be taken since certain contributions may not be properly considered [27].

As a general statement, the perturbative approach can be as accurate as the original description in terms of eigenvalues and eigenstates of the physical system considered, assuming of course small perturbations. It can be easily extended to higher order nonlinearities and has the advantage that all paths of evolution for the system are considered. For the more complex cases, the calculations tend to become increasingly complex and the use of numerical calculations becomes a necessity. Obtaining simple analytical formulas may prove impossible without neglecting certain terms, an approach which is not suggested without careful considerations.

4.3. Tunneling or semi-classical approach

Another approach that was widely used in the past is based on first evaluating the effect of the field on the system and then calculating the transition rates using 1^{st}-order perturbation theory. The electronic states in the conduction and valence bands are "dressed" in the sense that the effect of acceleration of the electrons due to the oscillating field is taken into account. The foundation for this type of calculation was set by Keldish [28] who introduced tunneling and showed a non-zero probability of ionization under the effect of a strong electromagnetic field with a frequency lower than the ionization potential. This method was used by Jones and Reiss [29] who compared the results to a perturbative calculation, using circular input polarizations.

Following Ref. [8] , these “dressed” states can be approximated by Volkov-type wavefunctions of the form

$$\Psi_i(\mathbf{k},\mathbf{r},t) = u_i(\mathbf{k},\mathbf{r})\exp\left[i\mathbf{k}\cdot\mathbf{r} - \frac{i}{\hbar}\int_0^t E_i(\tau)d\tau \right] \tag{4.12}$$

where the index i refers to either the conduction or the valence band and $u_i(\mathbf{k},\mathbf{r})$ are the Bloch wavefunctions of the unperturbed system. The Volkov states are the exact solutions of the time-dependent Schrödinger equation for a single particle in an electromagnetic field obtained by applying a unitary transformation

$$\Omega = \exp\left\{ -\int_0^t \frac{e}{m}\mathbf{A}(\tau)d\tau\cdot\nabla \right\} \tag{4.13}$$

to the solution obtained in the absence of the external fields. By analogy, these Volkov-type states are therefore Bloch states with an envelope phase modulated by the classical trajectory of the electron oscillations. The optical field modifies the electronic states participating in the transition, through the so-called ac Stark effect by analogy to the well known dc Stark effect of splitting the transition lines in the presence of a strong electric field. The effect of the oscillating field is to modify the oscillator strength through the transition matrix elements (time dependent term) and also to modify the energies of the electronic states (time-independent term). The time-dependent and time-independent ac Stark shifting terms are given by

$$E_c(\tau) = E_{c0} + \Delta E_{cc}(\tau) + \Delta E_{cv} \tag{4.14}$$

$$E_v(\tau) = E_{v0} + \Delta E_{vv}(\tau) + \Delta E_{vc} \tag{4.15}$$

where the conduction and valence bands are considered to be parabolic with effective masses of m_c and m_v and the respective Stark shifts are given by

$$\Delta E_{ii} = -\frac{e\hbar}{m_i c}\mathbf{k}\cdot\mathbf{A}(\tau) \tag{4.16}$$

$$\Delta E_{cv} = \frac{e^2 {A_0}^2}{4m_{cv}c^2} \tag{4.17}$$

The last term is the classical ponderomotive energy of the electron/hole in an oscillating electromagnetic field known also as the "mass energy shift". From this point on, 1st order perturbation theory is used to calculate the transition rates according to a scattering matrix approach

$$S = -\frac{i}{\hbar}\int_{-\infty}^{\infty} dt \int d\mathbf{r}\, \Psi_c^{*}(\mathbf{k},\mathbf{r},t) H_{\text{int}} \Psi_v(\mathbf{k}',\mathbf{r},t) \tag{4.18}$$

Substituting the dressed states in Eq. 4.18 we obtain the following form

$$S = \frac{i}{\hbar}\frac{e\,\mathbf{a}\cdot\mathbf{p}_{vc}}{mc}\int_{-\infty}^{\infty} dt A_0 \cos(\omega t)\exp[i\eta\sin(\omega t)]e^{i\omega_{vc}t} \tag{4.19}$$

where $\mathbf{p}_{vc}$ is the momentum matrix element given by

$$\mathbf{p}_{vc} = \frac{i}{\hbar}\int d\mathbf{r}\, u_c^{*}(\mathbf{k},\mathbf{r})\nabla u_v(\mathbf{k},\mathbf{r}), \tag{4.20}$$

the effective energy transition is given by

$$\hbar\omega_{vc} = E_G - \Delta E_{vc} + \Delta E_{cv} + \frac{\hbar^2 k^2}{2}\left(\frac{1}{m_c} - \frac{1}{m_v}\right) \tag{4.21}$$

and

$$\eta = \frac{eA_0\mathbf{k}\cdot\mathbf{a}}{c\omega}\left(\frac{1}{m_c} - \frac{1}{m_v}\right) \tag{4.22}$$

with **a** being the unit vector for the magnetic vector potential. In order to avoid the oscillatory exponent an expansion in terms of Bessel functions is used

$$\exp[i\eta\sin(\omega t)] = \sum_{n=-\infty}^{\infty} J_n(\eta)e^{in\omega t} \tag{4.23}$$

to obtain

$$S = \frac{i\pi}{\hbar}\frac{e\,\mathbf{a}\cdot\mathbf{p}_{\mathrm{vc}}}{\mathrm{mc}}\sum_{n=-\infty}^{\infty} J_n(\eta)A_0[\delta((n+1)\omega+\omega_{vc})+\delta((n-1)\omega+\omega_{vc})] \tag{4.24}$$

A similar expression can be obtained for a two-beam input of the following form, this time using the Bessel function expansion method twice

$$S \sim \sum_{m,n=-\infty}^{\infty} J_m(\eta_1)J_n(\eta_2)\begin{Bmatrix} A_{01}\left[\delta((m+1)\omega_1+n\omega_2+\omega_{vc})+\delta((m-1)\omega_1+n\omega_2+\omega_{vc}\right]+ \\ A_{02}\left[\delta(m\omega_1+(n+1)\omega_2+\omega_{vc})+\delta(m\omega_1+(n-1)\omega_2+\omega_{vc})\right] \end{Bmatrix} \tag{4.25}$$

This expression is useful because it allows for identifying particular physical processes by isolating terms of the type $-2\omega_1+\omega_{vc}$ corresponding to degenerate 2PA, $-\omega_1-\omega_2+\omega_{vc}$ corresponding to non-degenerate 2PA or $-\omega_1+\omega_2+\omega_{vc}$, $\omega_1-\omega_2+\omega_{vc}$ corresponding to Raman processes, for example.

Performing the integration in *k* space one has to deal with integrating $\mathbf{a}\cdot\mathbf{p}_{vc}$ and $\mathbf{k}\cdot\mathbf{a}$ factors. The angular dependences of these factors yield different results on integration depending on the specifics of the bands considered. However, a total contribution from heavy-hole and light-hole bands can be calculated for degenerate 2PA [30] and the results were shown to better match the experimental data.

Important to note at this point is that if one uses the same band structure, the perturbative and tunneling calculations yield identical results for 2PA as "dressing" the states is equivalent to a self-transition in the second-order perturbation theory approach. However, the tunneling approach cannot be easily applied in conjunction with more complex models (e.g. Kane band structures) as problems arise when dealing with multiple valence band degeneracies and

accounting for inter-valence band transitions cannot be done properly. These types of transitions happen to play a minor role for the case of 2PA. For higher order processes, like the case of degenerate 3PA, the tunneling approach is equivalent to considering one inter-band transition and two intra-band ones which yield terms which are less significant than the three-fold inter-band transition terms which we show to be dominant. For the 3PA case also, considering contributions from transitions originating from multiple valence bands turns out to be extremely important as interference from multiple evolution paths greatly affects the final result and this has been demonstrated in this work, both theoretically and experimentally, for the first time [31]. This shows that tunneling theory might be less suitable for such types of analyses. One advantage is however, the fact that such “dressed” state calculations can be useful for strong interaction scenarios where perturbative methods cannot be employed anymore [32].

CHAPTER 5: NON-DEGENERATE TWO-PHOTON ABSORPTION

The two-photon absorption (2PA) process in semiconductors has been extensively studied in the past both experimentally and theoretically. A large amount of the data gathered was on degenerate 2PA and the spectral variety of the laser sources available allowed the buildup of a fairly comprehensive set of degenerate nonlinear spectra for many semiconductors [33, 34]. The scarcity of laser sources in the early years limited the experiments on non-degenerate 2PA to excitations with common laser wavelengths and using the broadband emission from inert gas lamps to probe the nonlinear effects [22, 35]. Development of highly tunable laser systems and of high intensity and short duration broadband continuum sources increased the accuracy of the values reported and extended the spectral ranges studied [35-37]. The large amount of experimental data published also helped to refine the theoretical models for nonlinearities in semiconductors as very good agreement with the calculations has already been demonstrated [8, 34].

An important result of the comprehensive work done on 2PA is the establishing of the scaling rules, giving an accurate prediction of 2PA and n_2 in semiconductors [8]. This allows for comparisons between nonlinearities in different semiconductors measured at various wavelengths. It has been shown both theoretically and experimentally that 2PA is inversely proportional to the bandgap energy cubed (Fig. 5.1). This implies that the already large degenerate nonlinearities measured in large gap semiconductors (cm/GW) can increase by 2 or 3 orders of magnitude in narrow gap semiconductors (InSb, InAs) [33, 38, 39]. Unfortunately, these extremely large nonlinearities (cm/MW) have to be measured at mid-IR wavelengths. The

general consequence is that for visible or near-IR wavelengths, degenerate 2PA will be limited to values of the order of cm/GW.

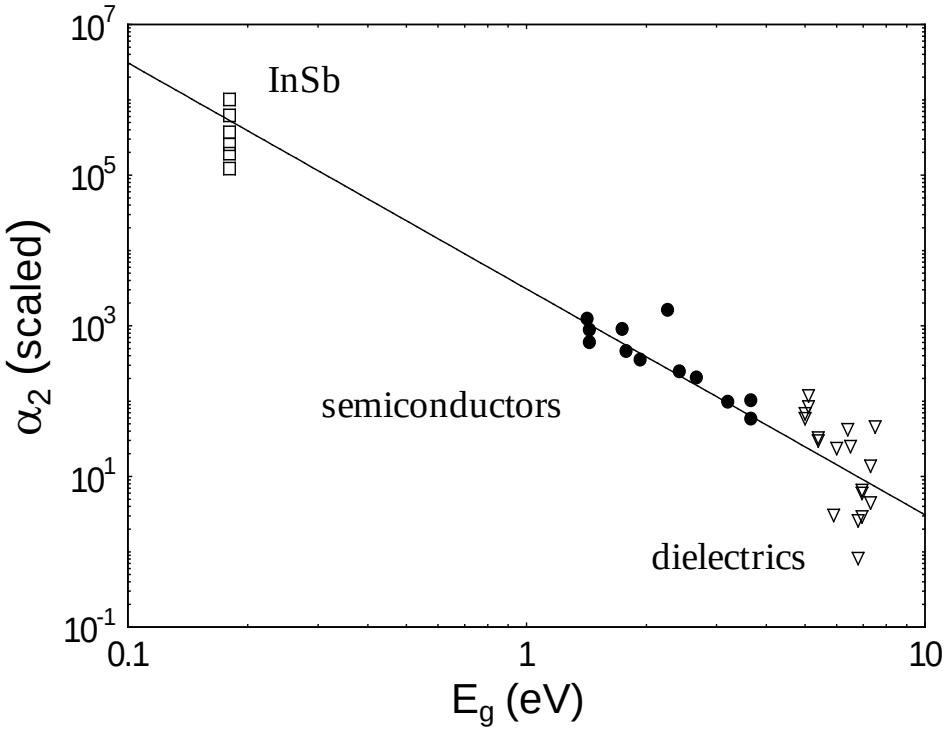

Figure 5.1 Scaled 2PA coefficient vs. bandgap energy from Ref. [8]. The straight line has a -3 slope.

There is, however, an alternative that would allow much larger nonlinearities to be measured at longer wavelengths. In the case of nondegenerate 2PA, the frequencies may approach intermediate state resonances which would significantly increase 2PA to values much larger than in the degenerate case. In this chapter, it will be shown that extremely nondegenerate (END) 2PA coefficients can exceed their degenerate counterparts by more than 2 orders of magnitude. This allows the extremely large 2PA coefficients, previously seen only in narrow-gap semiconductors, to be observed in large gap semiconductors such as GaAs or CdTe. This large enhancement of 2PA can be useful for optical switching and could have important consequences

for lasers and amplifiers based on 2-photon gain [32]. By applying Kramers-Kronig relations to nondegenerate nonlinear absorption to obtain the dispersion of the nonlinear refraction [40], an enhancement of the nondegenerate Kerr index coefficient (n_2) is predicted; however, positive and negative contributions from Raman and AC Stark terms lead to a smaller enhancement but an extremely rapid dispersion around the zero crossing, shifting it to near the band edge.

5.1. Theoretical analysis

While data for nondegenerate 2PA spectra exist from the earliest experimental papers [22], no data was published for extremely nondegenerate 2PA, e.g. ratio of photon energies ~10x. As seen from Eq. 5.1 this is an interesting realm to investigate since as either or both photons approach a linear absorption resonance, the 2PA is expected to diverge (of course adding in decay avoids divergence). In the case of extremely nondegenerate 2PA there are actually two resonances; the low energy photon is near resonant for the self transition and the large energy photon is nearly one-photon resonant. This can be easily seen qualitatively from the expression for the nondegenerate two-photon rate, W_2^{ND}, which can be written in the perturbative framework as [41]

$$W_2^{ND} = \frac{2\pi}{\hbar}\sum_{vc}\left|\sum_i\left[\frac{\langle c|H_2|i\rangle\langle i|H_1|v\rangle}{E_{iv}(\mathbf{k})-\hbar\omega_1}+\frac{\langle c|H_1|i\rangle\langle i|H_2|v\rangle}{E_{iv}(\mathbf{k})-\hbar\omega_2}\right]\right|^2\delta[E_{cv}(\mathbf{k})-\hbar\omega_1-\hbar\omega_2] \qquad (5.1)$$

with indices *1* and *2* designating the two photons, *H* the electron-field interaction Hamiltonian and *v*, *c* and *i* the valence, conduction and intermediate states, respectively. If one considers the simple model of a 2-band semiconductor, the virtual state can be taken as either the initial or the

final state for the electron transition. For this case, one can write explicitly the contributions from different paths of evolution for the system and obtain

$$W_2^{ND} \sim \left| \frac{M_{vc}^{2} M_{vv}^{1}}{-\hbar\omega_1} + \frac{M_{vc}^{1} M_{vv}^{2}}{-\hbar\omega_2} + \frac{M_{cc}^{2} M_{vc}^{1}}{\hbar\omega_2} + \frac{M_{cc}^{1} M_{vc}^{2}}{\hbar\omega_1} \right|^2 \tag{5.2}$$

where $M_{ij}^{1,2} = \langle j | H_{1,2} | i \rangle$ are the corresponding matrix elements, i, j correspond to a state in either the valence or the conduction band, while the superscript denotes the field frequency. Lower photon energies will decrease the denominator values thus increasing the 2PA. It's important to observe here that each of the two different possible transition sequences yields a term enhanced significantly by the presence of a low energy photon. This effect is similar to the intermediate state resonance enhancement (ISRE) predicted and seen in molecular systems [42]. In direct-gap semiconductors the 1-photon absorption edges are sharper than those of organics and therefore larger enhancements may be obtained when probing very close to the linear absorption range.

Theoretical calculations of third-order nonlinearities in semiconductors are very well documented, and there are a couple of approaches commonly used in the past, which have been discussed in more detail in Chapter 4. One of the methods involves the use of second-order perturbation theory, as in Eq. 5.1, to directly calculate the transition rates using a quantum mechanical description (eigenvalues and eigenstates) of the considered systems. Reasonable predictions can be made either using a simple 2-parabolic band model [27, 43] or one can employ complex 4- or 7-band calculations for better accuracy [44, 45], which can go as far as predicting the anisotropy of the nonlinear coefficients for particular systems like the ones exhibiting zincblende symmetry [24]. Another theoretical method that was successfully used in the past and in the calculations shown in this work is based on Keldysh's tunneling theory [28]. It uses a scattering matrix formalism with Volkov-type "dressed" wavefunctions for the

electronic states in order to account for the effect of the electric field on the system [46]. This provides similar 2PA spectra to the perturbation methods with excellent predicted absolute magnitudes [8]. The nondegenerate 2PA coefficient is written as

$$\alpha_2(\omega_1;\omega_2) = K\frac{\sqrt{E_p}}{n_1 n_2 {E_g}^3} F_2\left(\frac{\hbar\omega_1}{E_g};\frac{\hbar\omega_2}{E_g}\right) \tag{5.3}$$

where

$$F_2(x_1;x_2) = \frac{(x_1+x_2-1)^{3/2}}{2^7 x_1 {x_2}^2}\left(\frac{1}{x_1}+\frac{1}{x_2}\right)^2 \tag{5.4}$$

E_p is the Kane energy parameter, E_g is the bandgap energy, K is a material independent parameter and n_1 and n_2 the refraction indices associated with frequencies ω_1 and ω_2, respectively. Fig. 5.2 shows the effects on 2PA when pumping with photons of different frequencies, with calculations made using Eq. 5.3. The logarithmic scale indicates a strong expected increase of the magnitude of 2PA coefficient as the frequency of the pump photons decreases.

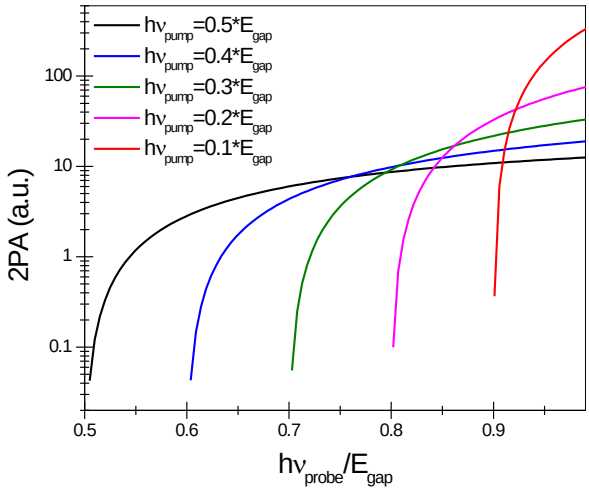

Figure 5.2 Enhancement of 2PA as a function of probe photon energy for several pump photon energies.

5.2. Experimental setup and results

There are multiple ways of measuring non-degenerate 2PA including four-wave mixing, pump-probe with single wavelengths or a continuum and 2-color Z-scan. The non-degenerate 2PA data presented in this work were taken in a standard pump-probe non-collinear geometry with a small angle (~7 degrees) between the pump and the probe beams. In all our experiments, the pump beam (most intense) always has the longer wavelength, with photon energies less than 30% of the bandgap energy.

There were two main reasons for this choice. First, we want to avoid any 2PA or 3PA caused by the pump itself which would complicate the experiment and the analysis of the experimental data. Also, self-absorption effects lead to the creation of free-carrier pairs which would cause extra losses especially for the longer (i.e. picoseconds) pulses. In our case the only loss in irradiance experienced by the pump happens during the temporal overlap and it's solely caused by non-degenerate 2PA with one photon being absorbed from each beam. This absorption term does produce free carriers as well; however, the density of carriers produced is proportional to the photon density from the weak probe beam which is deliberately kept very small (at least 20 times smaller irradiance than the pump for the femtosecond pulses and 100 times smaller for picosecond pulses). This way, effects of free-carrier absorption and refraction can be ignored altogether. The second reason the pump is the low photon energy beam is related to the magnitude of the 2PA coefficient. In a nondegenerate experiment there are two possible choices in terms of excite-probe photon pairs. Different experimental configurations can however lead to very different measured values as 2PA scales with the photon frequency at which the absorption is monitored. The frequency dependence of the 2PA coefficient (Eq. 5.3 and 5.4) through the F_2

function leads to the relation $\alpha_2(\omega_1;\omega_2)/\alpha_2(\omega_2;\omega_1) = \omega_1/\omega_2$. In other words, if the frequencies of the pump and the probe would be switched the ratio of the measured 2PA coefficients would be equal to the ratio of the respective frequencies. Pumping with lower energy photons and probing with higher energy photons leads to the maximum possible depletion of the probe beam for a given irradiance level of the pump beam. This way, our experimental configuration then allows us to measure the highest non-degenerate 2PA coefficient possible.

The use of a small frequency pump allows for the variation of the probe frequency only over a limited range. For a given pump, the lower limit is set by the lowest energetically possible transition, and the higher limit is set by the absorption edge. In our experiments, the probe photon energy can be varied between E_g-$h\nu_{pump}$ and E_g.

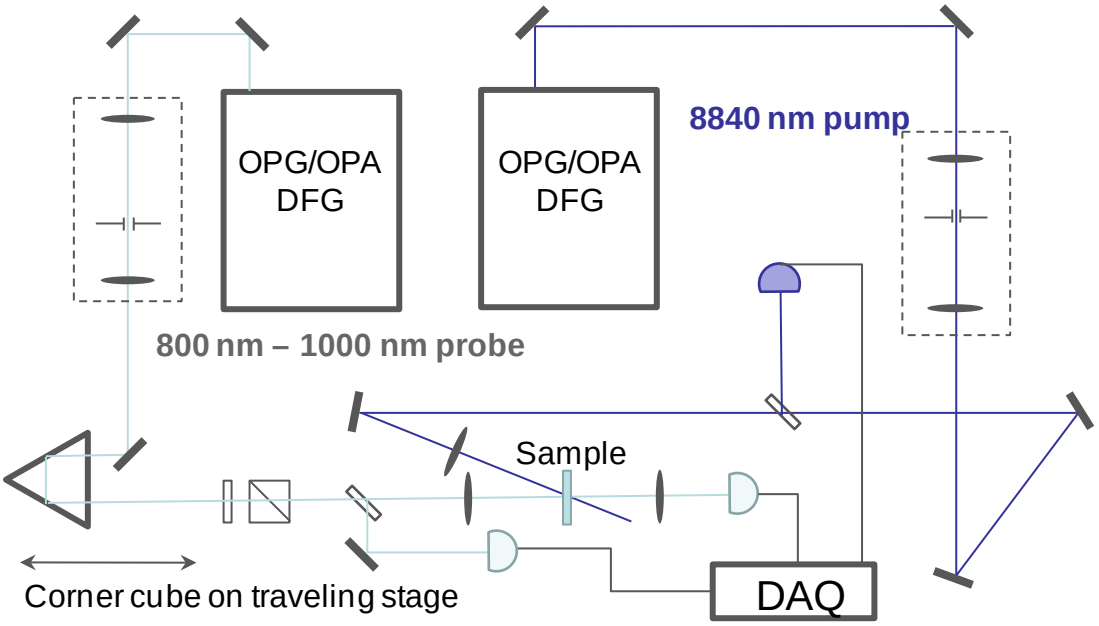

Figure 5.3 Experimental layout for the picosecond nondegenerate 2PA experiments.

The picosecond pump-probe experiments were performed using the picoseconds system described in detail in Chapter 3. The experimental layout is shown in Fig. 5.3. The IR pumping

wavelength was chosen to be 8840 nm corresponding to approximately 10% of the bandgap of GaAs, which together with CdTe were the two semiconductors studied in this configuration. Our choice of pump wavelength was also based on the available tunability range of the IR (8-14 μm) and taking into account the energy and beam quality at the output wavelengths. As mentioned before, the irradiance of the probe was kept much lower than that of the pump (for picosecond pulses ~100 times). Our probe beam had a maximum energy of a few nJs and a smaller spot size than that of the pump, as measured by knife-edge scans, with a ratio of 1:2. In our configuration, this causes minimal losses through degenerate 2PA (< 0.5% which is at our noise level).

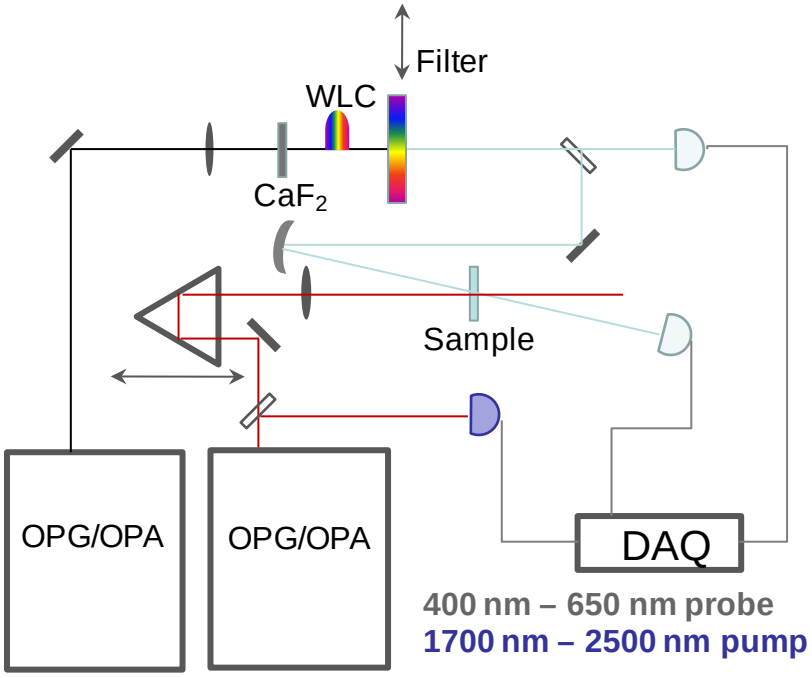

Figure 5.4 Experimental layout for the femtosecond pump-probe experiments.

A similar setup (Fig. 5.4) was used for our femtosecond experiments. The pump used for these experiments is in the wavelength range of 1200 nm to 2500 nm, corresponding to approximately 30% to 15.5% of the bandgap energy for the semiconductors studied (ZnSe, ZnS, ZnO). The probe in this case was a white-light continuum (WLC) generated using the 1300 nm

signal beam from the TOPAS into a 2 mm thick piece of CaF_2. Individual wavelengths were selected using a set of spike filters with a spectral bandwidth of ~ 10 nm. The temporal width of the pulses is between 140 fs and 160 fs as verified through autocorrelation experiments. The pump to probe spot size ratio is ~ 7 to 1 and, as in the previous experiments using picoseconds pulses, great care is taken to ensure that the irradiance in the probe is small enough that any self effects are negligible (at least 20 times smaller probe irradiance).

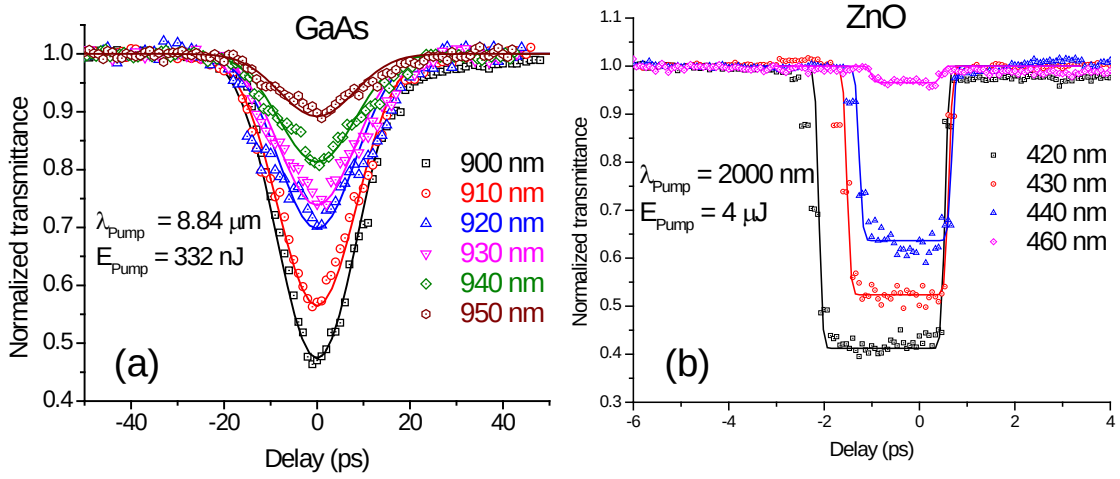

Figure 5.5 Experimental pump-probe data in GaAs (a) using picoseconds pulses and ZnO (b) using femtosecond pulses along with theoretical fits (solid lines).

Typical experimental pump-probe data are shown in Fig. 5.5 for GaAs (a) with picosecond pulses and for ZnO (b)with femtosecond pulses . In the picoseconds experiments, the pump photons' energy is approximately 10% of the bandgap of GaAs and 9.3% of that of CdTe. For the case of femtosecond experiments, there were more choices for the pump wavelength. In ZnO, for instance, we were able to choose five different pump photon energies equal to approximately 32%, 23%, 19.5%, 17% and 15.5% of the bandgap energy. The lowest pump photon energy corresponded to a wavelength of 2.5 μm which was at the end of the tunable range of our system.

Similar pump photon energies were chosen for ZnSe and ZnS. As mentioned before, the generated photo-carrier densities were low because of the small irradiance of the probe, rendering any free-carrier effects negligible. The cross-correlation picosecond data is easy to interpret and analyze quantitatively. For the much shorter femtosecond pulses however, group velocity dispersion (GVD) plays a very important role. This is apparent in the shape of our temporal pump-probe curves and how that shape changes with the probe wavelength. Specifically, the group velocity varies strongly with wavelength, and for a large range of initial delays the pump (fast) and probe (slow) pulses effectively walk through each other as they propagate through the sample. The recorded effect is therefore an average of "effective" temporal overlaps, and as this "effective" overlap distance is smaller than the sample thickness we obtain the same change in transmittance for a range of initial delays as seen in Fig. 5.5 (b). The GVD effects on nondegenerate 2PA were analyzed in detail in Ref. [37]. To fit our data we use the following formula for the nonlinear transmittance of the probe

$$T(\tau_d, W, \rho, \Gamma) = \frac{1}{W\sqrt{\pi}} \int_{-\infty}^{\infty} \exp\left\{ -\left(\frac{\tau + \tau_d - \rho}{W} \right)^2 - \frac{\Gamma\sqrt{\pi}}{\rho} \left[erf(\tau) - erf(\tau - \rho) \right] \right\} d\tau \qquad (5.5)$$

where τ_d is the probe delat normalized to the pump pulse duration, W is the ratio of probe and pump pulse durations, $\Gamma = \alpha_2 I_{pump} L$ is the nonlinear absorption coefficient and ρ is the GVD coefficient defined as

$$\rho = \frac{L}{t_{pump} c} \left[n_g(\lambda_2) - n_g(\lambda_1) \right] \text{with } n_g(\lambda) = -\left(\lambda \frac{dn(\lambda)}{d\lambda} - n(\lambda) \right) \qquad (5.6)$$

We used Sellmaier equations [47] for the frequency dependence of the refractive index. For a given sample length the width of the curves depends only on GVD and is not a fitting parameter,

as the GVD coefficient is calculated. The amplitude however, depends on both GVD and the 2PA coefficient, which needs to be extracted through fitting.

It should be mentioned here that in our femtosecond experiments the pump is actually delayed and the slope seen at shorter times corresponds to pulses overlapping at the back of the sample. The probe pulse gets chirped (particularly for frequencies closed to linear absorption edge) and the induced temporal broadening results in an increase of the above mentioned "effective" overlap distance as the pulse propagates through the sample. This lowers the largest temporal delay for which the pump and the probe completely walk through each other in the sample, narrowing the plateau seen in the data. Over a 10 nm range, the nondegenerate 2PA coefficient varies from about 25% when probing close to the band edge to as much as 100% at longer wavelengths. However, based on our estimates, these effects aren't as critical when calculating the nonlinear coefficients for our thin samples for ~150 fs pulses, and the net result is an overestimation of the largest 2PA value of less than 15%., for the probe wavelength closest to the resonance.

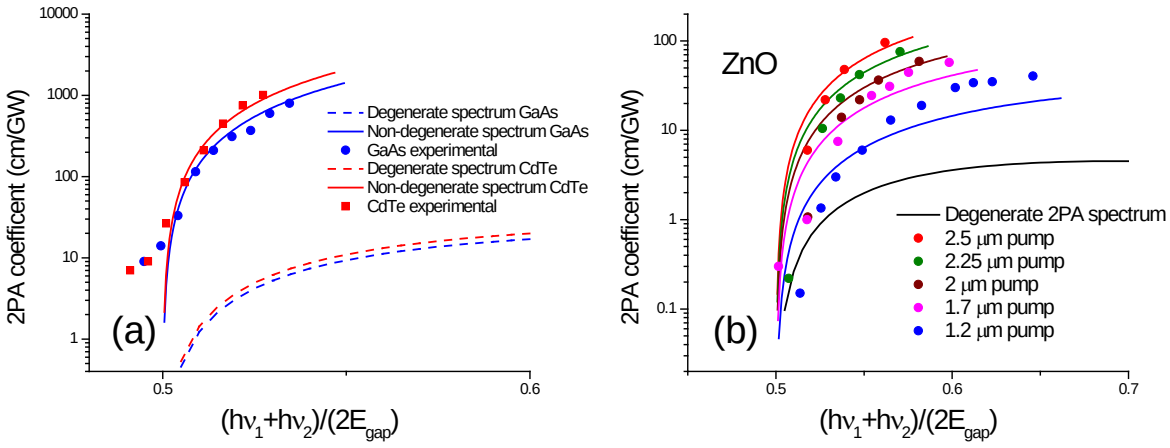

Figure 5.6 Non-degenerate 2PA spectra of CdTe and GaAs measured with picoseconds pulses (a) and of ZnO measured with femtosecond pulses (b). The calculated non-degenerate spectra are shown with straight lines, while the dashed lines denote the corresponding degenerate spectra.

In Fig. 5.6 (a) we show the measured non-degenerate 2PA spectra of GaAs and CdTe using picoseconds pulses and Fig. 5.6 (b) the measuerd spectra of ZnO using femtosecond pulses,along with the respective degenerate spectra, plotted versus the corresponding degenerate photon energy. The corresponding degenerate energy is simply taken as the average of the energies of the pump and probe photons. In other words, we compare the coefficients for two transition processes between the same energy levels. In all our plots the photon energies are shown scaled to the respective bandgap energies since this allows comparing different semiconductors on the same scale and makes the comparison to the respective degenerate values easier. The theoretical values are represented with solid lines together with measured degenerate data where available. The measured non-degenerate values get as large as 1 cm/MW in CdTe, ~180 times larger than the corresponding degenerate ones and about 40 times larger than the peak degenerate 2PA. There is a remarkable agreement between the measured and the predicted values using the simple 2 parabolic-band model, over a large range of photon energies. This agreement isn't entirely

surprising since in experiments with very non-degenerate photons the states involved in transitions are close to the center of the Brillouin zone (k=0), where the parabolic approximation works best.

We were able to measure some small signals in GaAs and CdTe when the sum of the energies of the two photons falls within the Urbach tail. There are a two of possible explanations for this. We could be accessing states below the band edge and because of the large enhancement we are able to measure such small contributions which would otherwise be impossible to do using degenerate photons. Another possibility is that we actually deal with a three-photon process in which two photons from the pump and one from the probe are absorbed, exciting a valence electron over to the conduction band. Normally, a clear differentiation can be done by analyzing data taken at different irradiance levels, since a 2PA process would give a linear variation of transmittance with pump irradiance while a 3PA process would give a quadratic dependence. Unfortunately, the signals were low and obtained using the maximum available pumping energy so that such clear delimitation wasn't possible.

A summary of results obtained for ZnSe and ZnS is presented in Fig. 5.7 (a) and (b), respectively. For these cases the choices of pump and probe photon energies were limited by the specifics of our experimental setup. Taking data with small photon energies in the pump beam proved difficult for the largest bandgap semiconductors, since for these cases the probe photons were close to the UV, and in our continuum the energies available for this part of the spectrum were low. This made the measurements difficult for some of the pump and probe photon pairs.

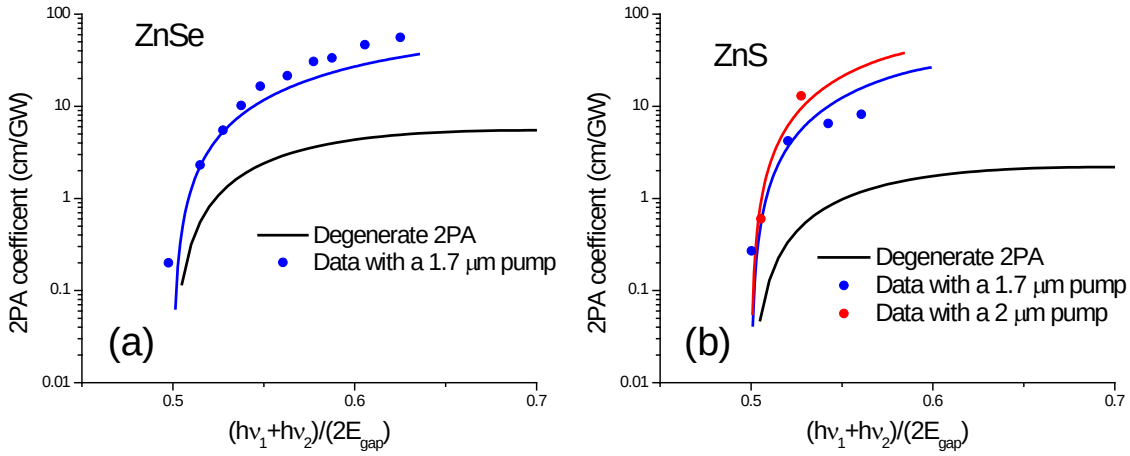

Figure 5.7 Non-degenerate 2PA spectra of ZnSe (a) and ZnS (b) measured with femtosecond pulses.

For the femtosecond measurements, the smallest pump photon energy corresponded to approximately 15.5%, 26.5% and 17% of the bandgap of ZnO, ZnSe and ZnS, respectively. Consequently the measured enhancement of the non-degenerate values with respect to the degenerate ones was smaller than in the case of picosecond measurements, with a maximum value of ~40 in ZnO. As shown, there is also a good agreement between theory and femtosecond experimental data. For the larger energy pump photons, the experimental data seems to be slightly larger than predicted with a sharper falloff towards the edge. However, these discrepancies appear at wavelengths very close to the band edge and should be best resolved using spectrally narrower pulses and, as mentioned for picoseconds pulses, using a larger range of input irradiances, unavailable to us. Even so, we believe that the simple theoretical model employed can give good estimates (within a factor of 2) for the magnitude of the non-degenerate 2PA coefficient on any direct-gap semiconductor using any pump-probe photon pair.

The data taken on ZnO (Fig. 5.6 (b)) best illustrates the strong dependence of the measured values on the pump wavelength. The longer the pump wavelength, the stronger is the

enhancement seen in the 2PA. The largest overall magnitude we measure are about 1 cm/MW using a mid-IR pump. We point out here that these nonlinearities are measured at visible and near IR wavelengths and their magnitudes come close to the degenerate values measured in narrow-gap semiconductors (e.g. InSb, InAs, etc.), at wavelengths in the mid-infrared [13, 39]. This can be easily understood by considering again the perturbative expression (Eq. 5.2) of the 2PA rate when using a simple 2-band model for a given pair of initial and final states. For the non-degenerate case, the energy term in the denominator gets as small as the pump energy, with one of the two terms being highly enhanced for either of the transition paths possible (a first "self" transition followed by a direct transition or vice versa). If we now consider the case of degenerate 2PA in a narrow-gap semiconductor at the pump wavelength ω_2, we obtain two terms with the same denominator energy values

$$W_2^{\,D} \propto \left| \frac{M_{vc}^2 M_{vv}^2}{-\hbar\omega_2} + \frac{M_{cc}^2 M_{vc}^2}{\hbar\omega_2} \right|^2 \tag{5.7}$$

Since the momentum matrix elements depend mainly on the symmetry of the bands involved, for similar systems (zincblende structures for instance), we should expect values of the same order of magnitude. The disadvantage is, however, the necessity of having long wavelength pump photons. To obtain the highest nonlinearities it is necessary to probe close to the linear absorption edge, effectively narrowing the available spectral range. To overcome this, a very good quality sample should be used, possibly at a lower temperature, in order to minimize any linear losses in the probe beam. However, there is an upper limit to the nonlinearities that can be obtained in a non-degenerate configuration. The main limitation is the linear absorption at the probe wavelengths under the bandgap. Assuming the upper energy limit for the probe photons set to 0.97 of bandgap energy, by using pump photons at about 5% of the bandgap energy one

would obtain only a moderate increase of the 2PA coefficient (only about 2 times) versus pumping with photons at 10% of the bandgap.

For the highly non-degenerate experiments, the behavior of the Kerr index in some particular spectral ranges is rather interesting. We mentioned before that the non-degenerate nonlinear index can be obtained using the general expression of the change in absorption caused by the presence of a pump beam and performing a Kramers-Kronig transformation [8, 40]. The nonlinear refractive index contains contributions from the 2PA, Raman and AC-Stark processes (Fig. 5.8). Explicitly, the AC-Stark term, which is the analog of saturation but below the gap, gives always a negative contribution to the nonlinear index while the Raman term adds positively.

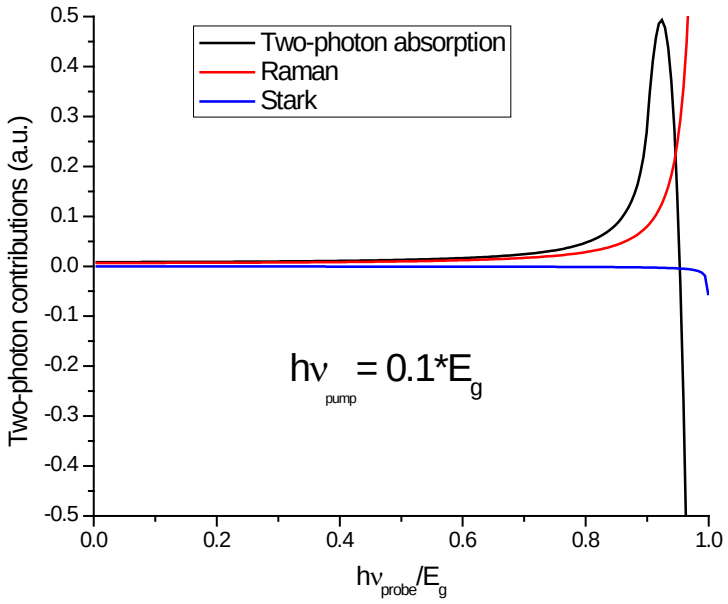

Figure 5.8 Contribution to nonlinear refraction from the two-photon, Raman and Stark terms for an energy of the pump photons of 10% of bandgap energy.

For the nondegenerate case, the calculated overall enhancement relatively is smaller when using small photon energy pumps. The nonlinear index takes positive values (focusing nonlinearity) for small probe frequencies and turns negative (defocusing nonlinearity) for frequencies close to the 1-photon absorption edge. The probe frequency for which the nonlinear index becomes zero depends strongly on the pump frequency. This particular point is near the peak 2PA position for the degenerate case and approaches frequencies very close to the linear absorption edge when the energy of the pump photons is further decreased. The slope of the spectrum near to the zero crossing point also changes strongly with the pump energy and becomes extremely steep for small energy pump photons. This leads to changes in the sign of the refractive nonlinearity over very narrow spectral ranges. These trends are shown in Fig. 5.9 for the particular case of GaAs. When pumping for instance at about 10% of the bandgap energy (8.84 μm), by varying the probe wavelength by ~13 nm, from 903 nm to 916 nm, we can vary the Kerr index coefficient from $-2*10^{-12}$ cm^2/W to $2*10^{-12}$ cm^2/W, numbers that in absolute value correspond to about 50% of the peak nonlinear index magnitude. To verify this effect, picosecond pulses are more suitable because of their narrower spectral widths. It would be however interesting to study the effect of this spectral dependence on a femtosecond pulse with a large bandwidth and centered on the zero crossing frequency.

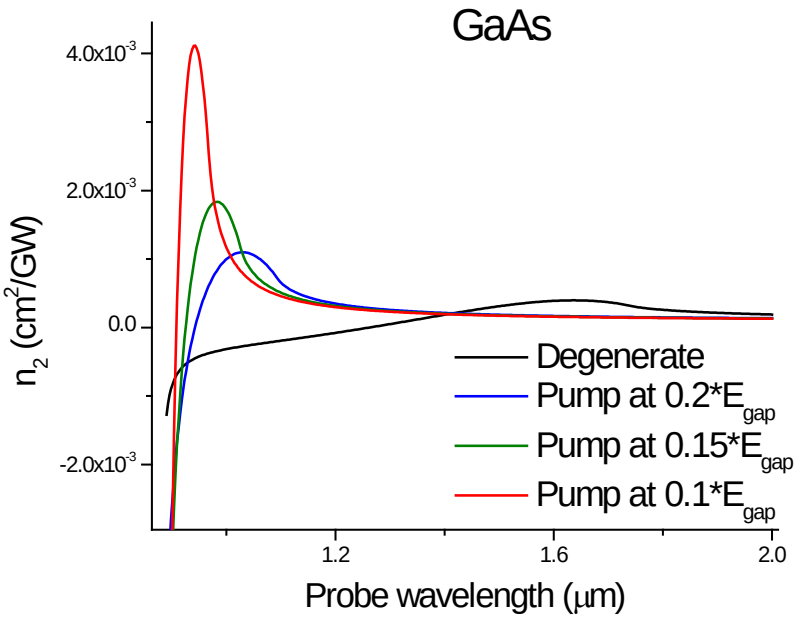

Figure 5.9 Calculated non-degenerate induced refraction index of GaAs for pump energies equal to 70% (1), 40% (2) and 10% (3) of the bandgap energy.

5.3. Possible applications

The large enhancements seen in these extremely non-degenerate frequency schemes look promising for some applications and a few ideas will be proposed in this section. The experiments described in this chapter have shown strong nonlinearities in a probe beam only in the presence of a strong beam with a very different frequency. Essentially our pump beam is a "control" beam, able to turn on and off the nonlinearity. This suggests that such effects may be used in optical switching. Traditionally, it is the change in the refractive index that is being

utilized and for this a large nonlinear Kerr coefficient is required to minimize the input power requirements [48].

The calculations from the previous section have shown an enhancement of n_2 of about an order of magnitude for the short wavelength beam as compared to the peak n_2 for the degenerate case when the long wavelength beam photons have energies of about 10% of the bandgap. Unfortunately, when these strong refractive effects are accompanied by strong absorptive effects, the figure of merit, given by $n_2/(\alpha_2\lambda)$ [49] is smaller than 1 due to the large 2PA coefficient. This suggests that for practical purposes, the probe photon energy has to be lower than the difference between the bandgap energy and the pump photon, thus preventing 2PA. In this range the maximum nondegenerate n_2 is still larger by about a factor of 5.5 than the peak degenerate n_2. One problem that needs to be pointed out is that if we require large enhancements we would be forced to use spectral regions where there is a strong variation of the nonlinear Kerr coefficient, effectively restricting the maximum allowed bandwidth for the probe pulse.

Another approach would be to use the absorptive effects to effectively "turn off" the probe beam by inducing an absorption of at least 90%. For our largest measured 2PA coefficient of 1 cm.MW, this condition would be met for a pump irradiance 29 GW/cm^2. This can be a viable option as long as such power levels in the pump beam are feasible for the given geometry. However, in this spectral range there are large variations of the magnitude of $n_2$and these should be taken into consideration. Also in this case, the spectral range over which n_2 stays positive (focusing) might be useful. Whether the absorptive or refractive effects can be employed there is the general issue of having two beam of very different frequencies co-propagating and this may pose considerable difficulties in guiding geometries, although not impossible.

Another possible idea is that of gated detection. Taking for instance a semiconductor detector irradiated with a beam having photons of energy slightly less than the bandgap energy can turn on and off the detector response by using a mid-IR pulse, which by itself would not produce any detector response. This can be accomplished with femtosecond resolution while such a cross-correlation experiment would also effectively extend the detector's spectral response range.

The analysis done in this chapter emphasized that the enhancement is caused by the intrinsic resonance present when calculating the probability for an electronic transition to higher energy states, mediated by the absorption of two photons. It is however possible that a transition from a higher energy state to a lower one can happen through the emission of two photons and experimentally this has been observed in atomic systems [50-52]. Should inversion of population be present, the spontaneous emission of two photons has a much smaller probability than the emission of one photon. However, stimulating such transitions using either one or two photons would increase the transition rate making it large enough to be observed experimentally. The possible scenarios for two-photon emission (2PE) are shown in Fig. 5.10. The two-photon stimulated processes should be described using a similar formalism to the one used for 2PA and this was pointed out by Ironside [53]. This suggests that any enhancement seen in the 2PA should be present in the process of 2PE as well.

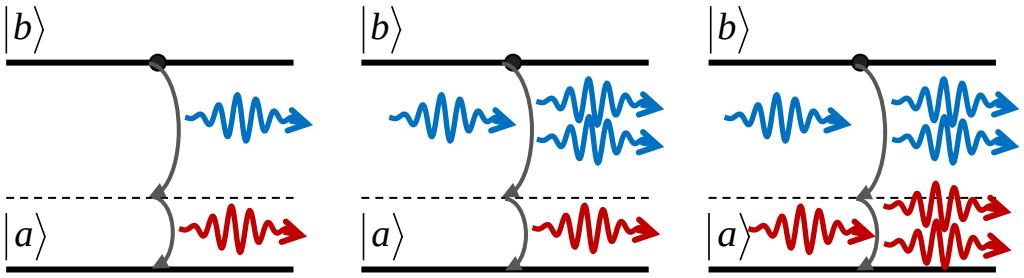

Figure 5.10 Schematic of possible two-photon emission process. The diagrams correspond to spontaneous, singly stimulated and doubly stimulated processes.

Recently, an experiment by Hayat et al [54] demonstrated spontaneous and stimulated 2PE in bulk GaAs and in quantum well structures. The inversion of population was produced by pumping linearly with a cw beam. The signals were detected using femtowatt detectors and were spectrally resolved with a monochromator. The authors recorded both the spontaneous and the induced 2PE when stimulating transitions with a frequency outside the linear absorption range and close to the degeneracy point (half the energy of the bandgap). A peak in the recorded spectrum was identified at the complementary wavelength and its amplitude was demonstrated to vary with the power input of the “seed” beam.

We attempted to perform a similar experiment using this time frequencies further away from the degeneracy point. We used a 1 mm thick piece of CdSe pumped by a 15 mW 532 nm cw laser. The stimulating beam was chosen to be very close to the linear absorption (energy of ~ 92% of the bandgap energy). The complementary wavelengths’ spectrum is limited at the higher wavelengths by a minimum energy corresponding to a transition from a state at the bottom of the conduction band and at the smaller wavelengths by the conduction band population as determined by the pumping power. We used the same HgCdTe detectors from our InSb experiments to detect the emitted radiation. The Ge window blocked any wavelength larger than

1.7 μm and to detect the signals we used a lock-in amplifier. In our experiment we used a chopper in the seed beam, rotating to give a modulation at 285 Hz. A plot of the recorded signals as a function of the seed (stimulating) beam energy is shown in Fig.5.11. The signal was recorded at the chopper's frequency and disappeared when the pump was blocked or the beam's overlap was lost. There was however a small signal detected in the absence of the pump which also depended on the seed beam. The 2PA of the seed beam itself produces carriers high up in the conduction band and in the relaxation process to the bottom of the band IR photons may be emitted [32]. We also plotted the difference of the signals recorded with the pump and in absence of the pump, which has a different behavior.

The very small signals obtained (μVs) made practically impossible any attempt at spectrally resolving the observed signal. Some limited conclusions were drawn, however, as we independently used two samples of InAs and InSb to act as long pass filters (3.5 μm and 7 μm respectively). Using the InAs we were able to greatly decrease the signal due solely to the seed beam (under the noise level), while being able to still detect a reasonable signal when pumping was present. We observed a similar behavior when we used the InSb sample, but in this case the reduction in the signal detected when the pump was turned on was much larger. This seems to suggest that the bulk of our emitted radiation had a wavelength between 3.5 and 7 μm. There is a spectral response of our detectors that increases with wavelength and that, at least qualitatively, does not contradict our conclusions.

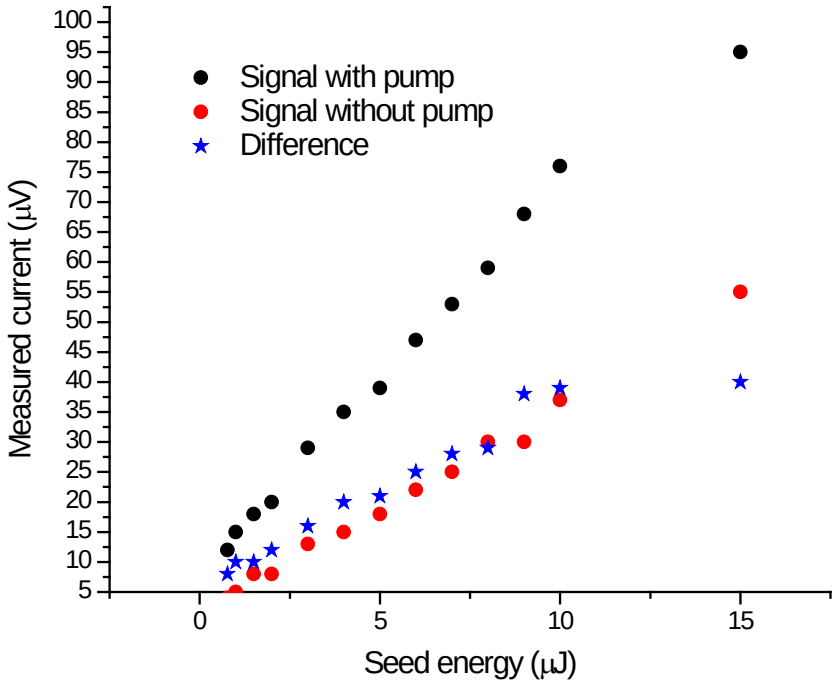

Figure 5.11 Mid-IR two-photon emission signal in a singly stimulated experiment.

This data, although still far from being conclusive, is very promising. The small signals recorded suggest that better collecting configurations should be used while using IR wavelengths to stimulate the transitions may result in larger measured signals, hopefully large enough to spectrally resolve.

CHAPTER 6: THREE-PHOTON ABSORPTION IN ZINBLENDE STRUCTURES

The experimental work done in semiconductors to confirm the validity of the calculations of [27, 43] consisted mainly of two-photon absorption data. Data on 3PA was (and still is) relatively scarce and even the more recent comparisons with the available theories were inconclusive [9]. 3PA is a higher order ($\chi^{(5)}$) process and that means it is weaker and consequently more difficult to study since comparatively, much larger irradiances are needed. For moderate irradiances when both 2PA and 3PA processes are present, 2PA will dominate and separation of the two absorptive effects is probably not possible. By increasing the irradiance, the relative contribution to the total absorption changes and the 3PA process will eventually become the dominant one; however, damage will probably occur first. This scenario is also not a very practical one since for this high an irradiance the total nonlinear absorption will be very high, while the photo-generated free carrier densities produced will be substantial, thus complicating the problem even more.

It is then apparent that 3PA data needs to be taken in a spectral region where 2PA is not energetically allowed. For most semiconductors, since the bandgap energies are in general not larger than 4-5 eV, this places the 3PA spectra in a wavelength range from the near to the mid IR. In the early years after the laser was invented this posed some problems since there were few laser sources in this part of the spectrum and the tunability of the available systems was limited. Right now this is hardly an issue since through parametric down-conversion and difference frequency generation this entire spectral range can be fully covered while also benefiting from a large range of pulse durations.

Most of the above mentioned difficulties still arise when attempting to measure 3PA with longer pulses (nanosecond or even picoseconds). It was mentioned before that since $\chi^{(5)}$ processes are weaker, larger irradiances are needed in order to observe such effects. When using longer pulses to obtain a large irradiance, fairly large fluence levels are unavoidable. This can lead to material damage even before the nonlinear effects can be observed making the use of ultrashort pulses a must. Another problem is the generation of large densities of photo-carriers. They complicate both the experiment itself as well as its interpretation since they can introduce large absorptive and refractive contributions.

Such issues are also present when measuring 2PA and in general either avoided by measuring small signals or by carrying out complementary experiments (e.g. time-resolved) which allow quantifying of all the effects present (we do this in Chapter 7 for InSb). For 3PA however, the photo-generated carrier densities are comparatively larger than for the 2PA case. This can be easily understood if one compares the carrier densities created through the two processes following the following crude analysis assuming the same minimum detectable signal and a given pulse duration. For small signals, considering the 2PA and 3PA processes, the changes in transmission are roughly given by $\beta I_{2PA}$and γI_{3PA}^2 while the generated densities are proportional to $\beta I_{2PA}^2$and γI_{3PA}^3, respectively. This means that when producing the same change in absorption, the ratio of the carrier densities produced varies with the ratio of the irradiances used. Since the irradiances used in 3PA experiments are generally at least an order of magnitude larger than those used for 2PA, this would make the free-carrier effects much more significant and great care needs to be taken in order to properly account for such effects. This suggests that experiments made using ultrashort (femtosecond) pulses while measuring moderately small signals may help avoid such problems, thus increasing the reliability of the extracted values. This

is particularly important since without reliable data one cannot identify the limitations of the available theories nor refine the models proposed.

6.1. Previous measurements of 3PA and comparisons with existing theories

The early measurements on 3PA were performed in configurations with Nd:YAG lasers pumping tunable dye lasers and using gas Raman cells for frequency down conversion [55-66]. The pumping was done using either degenerate or nondegenerate schemes while monitoring the emitted luminescence. The excitations were in a narrow spectral region just above bandgap. Direct gap (ZnS, ZnO, ZnSe, CdS and GaP) [56-58, 62] and indirect gap (CdI_2) [63] semiconductors were investigated, together with a large number of alkali halides [55, 59].

Kang *et al*.[67] measured 3PA in AlGaAs just outside the 2PA range using a NaCl color center laser operating from 1.48 to 1.66 μm using ~1 ps pulses. The scope of the study was to determine the limits posed by 3PA on all-optical switching experiments. Recently, measurements on GaN, GaAs, ZnO and ZnS were reported over larger spectral domains employing femtosecond pulses [9, 61, 65]. The newer data was obtained using single beam experimental methods. Transmittance was measured as a function of the input irradiance by varying the pulse energy (optical limiting) or the beam size (Z-scan) or in a slight variation of the Z-scan technique, by measuring the photo-induced current at several positions along the focused beam [65]. The data on GaAs was taken in order to characterize losses directly induced by 3PA or by the photo-generated carriers in devices generating THz waves [61]. The spectral range covered was large, but since values at only four different wavelengths were measured, the results didn't allow for definitive conclusions. Similarly, the data taken by He *et al*. [9] on ZnO and ZnS spans

a large wavelength range but unfortunately shows no measurements closer to the three-photon edge. Not surprisingly, the comparison with the simple available theories (scaled arbitrarily to match the measured magnitudes) was rather inconclusive and seemed to produce more questions rather than answer any.

We discussed in Chapter 4 the two main approaches when calculating nonlinear absorption coefficients in semiconductors. One method is to use time-dependent perturbation theory to calculate transition rates from the valence band to the conduction band resulting from N-photon absorption, taking into account all possible transition routes. The perturbation approach was used by Wherrett [43] for calculating 2PA spectra and generalized for higher-order nonlinearities as well using a two parabolic band model. The second method was originally proposed by Keldysh [28] and uses first-order perturbation theory with "dressed" states approximated by Volkov-type electronic wave-functions to account for the acceleration of the electrons by the incident ac field [29]. This method, referred to as tunneling theory, essentially assumes that the transitions take place between Stark-shifted energy bands. It is important to note here that if the same band structure assumptions are used (2-parabolic band approximation), the two approaches yield identical results when calculating 2PA up to an angular averaging factor f_2 / f in Ref. [43] which is determined to be $1/5$ in Ref. [8]. As mentioned in Chapter 4, this happens since in the case of 2PA, the dressed wave-function approach is essentially equivalent to a self-transition in the second-order perturbative approach.

The perturbative method can be easily used, in principle, for any higher order nonlinear process. The difficulty arises mostly from how well the band structure is described and whether only some (or all) transitions are taken into account. However, for higher order processes calculations become complicated. In order to simplify the problem, previous attempts have

restricted the types of transitions considered (keeping the dominant ones, i.e. larger momentum matrix elements among the various bands and smaller detuning energies) [27, 43]. An attempt to calculate 3PA in direct-gap semiconductors using perturbation theory and a more complex band structure was made by Mitra [64]. Again, in order to simplify the problem, only interband transitions were considered in a model consisting of three conductions bands and one valence band, while spin degeneracy was accounted for through an overall multiplicative factor of 2.

The tunneling approach is even more difficult to use when dealing with higher-order nonlinearities, since it cannot account for intervalence band transitions when using more than one valence band [41]. It therefore ignores some potentially large contributing transition routes which significantly affects the predicted magnitude of the nonlinear absorption coefficient [31].

Using models with two parabolic bands, Wherrett [43] (using the perturbative approach) and Brandi and de Araujo [27] (using tunneling theory) obtained similar formulas for the 3PA coefficient of the type $\alpha^{(3)}(\omega) = K\frac{P^3}{n_0{}^3 E_G{}^7} F_3\left(\frac{\hbar\omega}{E_G}\right)$, where K is a material-independent constant and F_3 contains the spectral dependency. However, both the predicted constants and spectral functions were different (Eqs. 6.1 and 6.2 respectively), yielding very different magnitudes for the 3PA coefficient

$$K^{(W)} = \frac{3^{10}\sqrt{2}}{8}\pi^2\left(\frac{e^2}{\hbar c}\right)^3\hbar^2 \text{ with } \mathrm{F}_3{}^{(W)}(x) = \frac{(3x-1)^{1/2}}{(3x)^9} \tag{6.1}$$

$$K^{(BA)} = \frac{3^{10}2\sqrt{2}}{5}\pi^2\left(\frac{e^2}{\hbar c}\right)^3\hbar^2 \text{ with } \mathrm{F}_3{}^{(BA)}(x) = \frac{(3x-1)^{5/2}}{(3x)^9} \tag{6.2}$$

Here $e^2/\hbar c$ is the fine-structure constant in *cgs* units, $\hbar$ is the reduced Planck constant, n_0 is the material's refractive index, P is the Kane momentum parameter defined later (Eq. 7.5),

E_G is the bandgap energy and $\hbar\omega$ is the photon energy. We obtained Eq. 6.2 from Brandi's original formula (Eq. 8 in Ref. [27]) assuming the same curvatures for the two parabolic bands and making use of the identity $\frac{P^2}{\hbar^2} \cong \frac{E_G}{2m_c}$, where m_c is the conduction band effective mass [8]. This relation can be obtained directly from $\mathbf{k}\cdot\mathbf{p}$ theory [23], while a slightly similar one was used in Ref [27] based on a Hartree-Fock calculation [68]. The lack of experimental data made it difficult to verify which was the most appropriate theoretical approach. More recent data raises further questions on the validity of the two theories since the trends observed match neither of the predicted spectra [9].

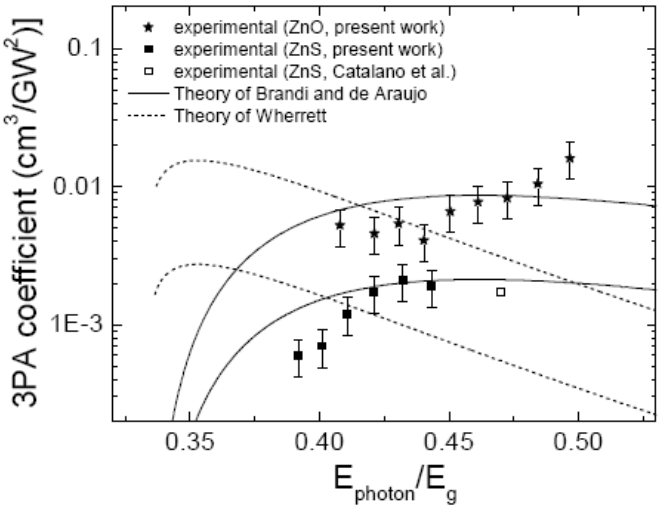

Figure 6.1 Experimental 3PA data on ZnO and ZnS from Ref. [10].

However, both theories predict an E_G^{-7} scaling of the 3PA coefficient for direct gap semiconductors. We attempted to verify this predicted dependence on the bandgap energy experimentally [10] by performing measurements of the 3PA coefficients in a large number of

semiconductors using various wavelengths. These data are shown on a logarithmic plot with scaled 3PA coefficients versus bandgap energy in Fig. 6.2.

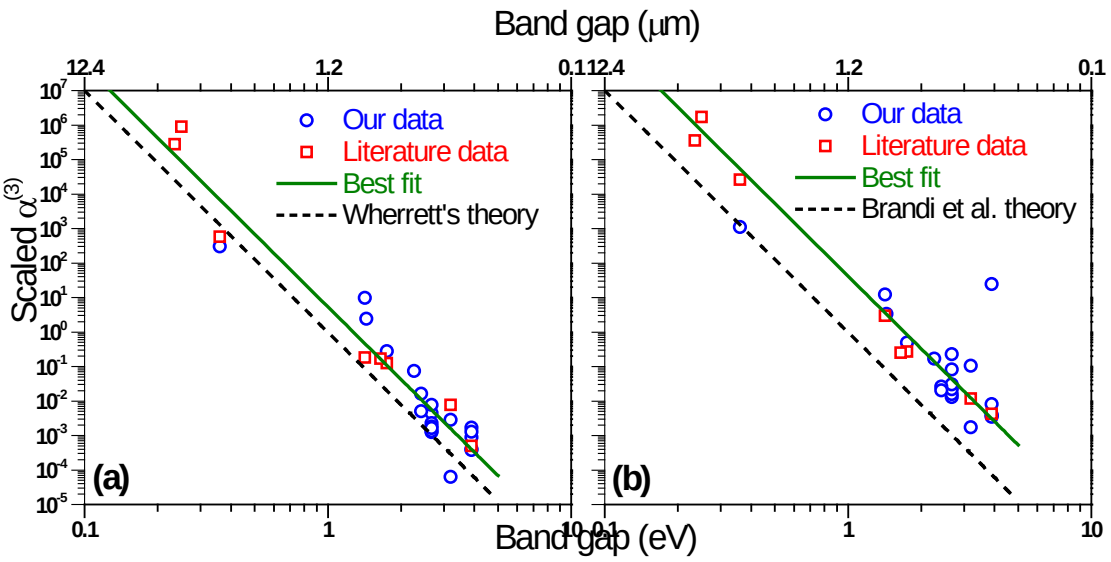

Figure 6.2Log-log plots of scaled 3PA coefficients (measured by Peter Olszak and some literature values [10]) vs. band gap energy using (a) Wherrett's and (b) Brandi and de Araujo's theories.

The scaling was done using both Wherrett's theory (a) and Brandi and de Araujo's (b). In each plot the dashed line is the theory while the solid line is a fit with a slope of -7 with $K_{fit}^{(W)} = K^{(W)} \times 5.5$ and $K_{fit}^{(BA)} = K^{(BA)} \times 42$. Even though the experimental data shows good overall agreement with the predicted bandgap scaling over several orders of magnitude, there is a significant spread in the experimental data with respect to the predicted values for individual semiconductors. This is due to inaccuracies in the modeling of the spectral behavior and indicates that a more refined approach is desired. Thus, the goal of the work presented here is to obtain the complete 3PA spectra of zincblende materials (ZnSe, ZnS, GaAs) from the 3PA edge

to the 2PA edge and compare it to our calculations using a 4-band model that overcomes the inadequacies of previous theories. A complete comparison of these theories to out numerical calculations is shown in Fig. 6.4.

6.2. Theoretical approach for calculating 3PA using the Kane 4-band model

In order to perform an accurate calculation of the 3PA coefficient in semiconductors, we need to use a realistic band structure which should account for the non-parabolicity and mixing of the bands considered. The model used in our theoretical calculations was developed by Kane [23]. We start by using the Schroedinger equation describing the motion of the electron in the following form

$$\left(\frac{\mathbf{p}^2}{2m} + V(\mathbf{r})\right)\Phi_n(\mathbf{r}) = E_n\Phi_n(\mathbf{r}) \tag{6.3}$$

Here $\Phi_n(\mathbf{r})$ and E_n are the wavefunction and the energy of an electron in an eigenstate labeled by *n*. Using the Bloch theorem, the solutions are expressed, in the reduced zone scheme, as

$$\Phi_{n\mathbf{k}} = \exp(i\mathbf{k}\cdot\mathbf{r})u_{n\mathbf{k}}(\mathbf{r}) \tag{6.4}$$

Substituting this particular form in Eq. 7.3 we obtain

$$\left(\frac{\mathbf{p}^2}{2m} + \frac{\hbar^2k^2}{2m} + V + (\hbar/m)\mathbf{k}\cdot\mathbf{p}\right)u_{n\mathbf{k}} = E_{n\mathbf{k}}u_{n\mathbf{k}} \tag{6.5}$$

At **k = 0** Eq. 6.5 reduces to

$$\left(\frac{\mathbf{p}^2}{2m} + V\right)u_{n0} = E_{n0}u_{n0} \tag{6.6}$$

In this form we can easily calculate the solutions since functions u_{n0} .are periodic. Once these solutions are found, we can treat the terms $\hbar^2 k^2 / 2m$ and $(\hbar / m)\mathbf{k} \cdot \mathbf{p}$ as perturbations and use standard non-degenerate perturbation theory (each eigenfunction corresponds to a distinct eigenvalue) to calculate the band dispersion [69]. This general method for calculating the band dispersion starting with known wavefunctions and energies at a particular point $\mathbf{k}_0$ is known as the $\mathbf{k} \cdot \mathbf{p}$ theory.

A direct result of this analysis is that the unperturbed conduction band wave-functions have a spherical symmetry and are denoted by $S\uparrow$ and $S\downarrow$ for the two spin states, while the ones corresponding to the valence bands have a p - like orbital symmetry denoted here by $X\uparrow$, $X\downarrow$, $Y\uparrow$, $Y\downarrow$, $Z\uparrow$ and $Z\downarrow$. These functions belong to the symmetry type Γ_1 and Γ_4 respectively, under the notation of Ref. [70]. Using this similarity to the atomic wavefunctions we can recall that the *s* states correspond to $l = 0$ while the *p* states correspond to $l = 1$ and are triply degenerate, with *l* being the orbital angular momentum. The three degenerate states can be chosen to be the eigenstates of l_z, the *z* projection of ***l***. The magnetic quantum numbers, eigenvalues of l_z, are -1, 0 and 1 for the *p* states.

Let us now consider the perturbation introduced by the spin-orbit interaction in the form

$$H_{SO} = \frac{\hbar}{4m^2c^2}(\nabla V \times \mathbf{p}) \cdot \sigma \tag{6.7}$$

where σ is the spin operator. The eigenfunctions of the spin-orbit Hamiltonian are eigenstates of the total angular momentum ***j***, the sum of orbital momentum and spin, and its *z* components. For the *p* states (valence) *j* can take either the values of 1-1/2=1/2 or 1+1/2=3/2 while for the *s* states (conduction) *j* is 1/2. Thus, the eigenfunctions of *j* and j_z are for the valence states

$$\left| jm_j \right\rangle \rightarrow \left\{ \begin{array}{l} \left| \frac{3}{2}, \frac{3}{2} \right\rangle, \left| \frac{3}{2}, -\frac{3}{2} \right\rangle \text{ corresponding to the heavy - hole band} \\ \left| \frac{3}{2}, \frac{1}{2} \right\rangle, \left| \frac{3}{2}, -\frac{1}{2} \right\rangle \text{ corresponding to the light - hole band} \\ \left| \frac{1}{2}, \frac{1}{2} \right\rangle, \left| \frac{1}{2}, -\frac{1}{2} \right\rangle \text{ corresponding to the split - off band} \end{array} \right\}$$

The spin-orbit interaction removes the triple degeneracy, splitting the $j = 3/2$ states from the $j = 1/2$ states. Thus, the split-off band is shifted by an energy of Δ at $\mathbf{k}$ =0.

In the most general form, including the interaction of the valence band and the conduction band via the $\mathbf{k} \cdot \mathbf{p}$ coupling and the spin-orbit interaction, the electron Hamiltonian for a cell-periodic structure is written as

$$H = \left(\mathbf{p}^2 / 2m\right) + \frac{\hbar^2 k^2}{2m} + V + (\hbar / m)\mathbf{k} \cdot \mathbf{p} + (\hbar / 4m^2 c^2)\left(\nabla V \times \mathbf{p}\right) \cdot \sigma \tag{6.8}$$

where $\mathbf{p}$ and σ are the momentum and spin operators, respectively, $\hbar$ is the reduced Planck constant, m is the electron mass, c is the speed of light, V is the one-electron potential and $\mathbf{k}$ is the wave vector. For the case of $\mathbf{k}$ oriented along *z*, the Hamiltonian can be represented as

$$\begin{bmatrix} H & 0 \\ 0 & H \end{bmatrix} \text{ where } H = \begin{bmatrix} E_s & 0 & kP & 0 \\ 0 & E_p - \Delta/3 & \sqrt{2}\Delta/3 & 0 \\ kP & \sqrt{2}\Delta/3 & E_p & 0 \\ 0 & 0 & 0 & E_p + \Delta/3 \end{bmatrix} \tag{6.9}$$

in the following basis

$$\left| iS\downarrow \right\rangle, \left| (X - iY)\uparrow / \sqrt{2} \right\rangle, \left| Z\downarrow \right\rangle, \left| (X + iY)\uparrow / \sqrt{2} \right\rangle, \left| iS\uparrow \right\rangle, \left| -(X + iY)\downarrow / \sqrt{2} \right\rangle, \left| Z\uparrow \right\rangle, \left| (X - iY)\downarrow / \sqrt{2} \right\rangle$$

where E_p and E_s correspond to the two eigenvalues obtained solving for E_{n0} in Eq. 67.6 for the valence and conduction band respectively, P is the Kane momentum parameter defined by

$$P = -i(\hbar / m)\left\langle S \left| p_z \right| Z \right\rangle = -i(\hbar / m)\left\langle S \left| p_y \right| Y \right\rangle = -i(\hbar / m)\left\langle S \left| p_x \right| X \right\rangle \tag{6.10}$$

and

$$\Delta = \frac{3\hbar i}{4m^2c^2}\left\langle X\left|\frac{\partial V}{\partial x}p_y - \frac{\partial V}{\partial y}p_x\right|Y\right\rangle \tag{6.11}$$

For an arbitrary orientation of the **k** vector, we can obtain the same form for the Hamiltonian using similar basis functions differentiated through the prime symbol. The primed functions are obtained through rotations from the original functions as given by

$$\begin{bmatrix} X' \\ Y' \\ Z' \end{bmatrix} = \begin{bmatrix} \cos\theta\cos\phi & \cos\theta\sin\phi & -\sin\theta \\ -\sin\phi & \cos\phi & 0 \\ \sin\theta\cos\phi & \sin\theta\sin\phi & \cos\theta \end{bmatrix}\begin{bmatrix} X \\ Y \\ Z \end{bmatrix} \tag{6.12}$$

and

$$\begin{bmatrix} \uparrow' \\ \downarrow' \end{bmatrix} = \begin{bmatrix} e^{-i\phi/2}\cos(\theta/2) & e^{i\phi/2}\sin(\theta/2) \\ -e^{-i\phi/2}\sin(\theta/2) & e^{i\phi/2}\cos(\theta/2) \end{bmatrix}\begin{bmatrix} \uparrow \\ \downarrow \end{bmatrix} \tag{6.13}$$

with $S' = S$ invariant under this rotation. Here the angles θ and ϕ are the usual polar angles of the **k** vector referred to the crystal symmetry axes *x*, y and *z* . The characteristic equation yields four double roots corresponding to the solutions to Eqs. 6.14

$$\begin{aligned} &E' = 0 \\ &E'(E' - E_G)(E' + \Delta) - k^2P^2(E' + 2\Delta/3) = 0 \end{aligned} \tag{7.14}$$

where $E_k = E'_k + (\hbar^2/2m)k^2$ is the energy of a state with a wavevector **k** .

The electronic wave functions are then given by

$$\begin{aligned} \Phi_{i\alpha} &= a_i\left[iS\downarrow\right]' + b_i\left[(X - iY)\uparrow/\sqrt{2}\right]' + c_i\left[Z\downarrow\right]' \\ \Phi_{i\beta} &= a_i\left[iS\uparrow\right]' + b_i\left[(-X - iY)\downarrow/\sqrt{2}\right]' + c_i\left[Z\uparrow\right]' \\ \Phi_{hh\alpha} &= \left[(X + iY)\uparrow/\sqrt{2}\right]' \\ \Phi_{hh\beta} &= \left[(X - iY)\downarrow/\sqrt{2}\right]' \end{aligned} \tag{6.15}$$

where α and β denote the two degenerate spin states (up and down). The index i refers to the conduction (c), light-hole (lh) and split-off (so) bands. The coefficients a, b and c are real and are obtained from

$$\begin{aligned} a_i &= kP(E_i'+2\Delta/3)/N \\ b_i &= (\sqrt{2}\Delta/3)(E_i'-E_G)/N \\ c_i &= (E_i'-E_G)(E_i'+2\Delta/3)/N \end{aligned} \tag{6.16}$$

where N is a normalizing factor such that $a_i^{\,2}+b_i^{\,2}+c_i^{\,2}=1$.

Using this formalism, we can obtain a complete description of the band structure taking into account the effects of non-parabolicity and non-zone center wave functions. We write the electron-radiation interaction (perturbation) Hamiltonian in SI units as [71]

$$H_{\text{int}} = \frac{e}{i\omega m_0}\left(\frac{I}{2\varepsilon_0 n_0 c}\right)^{1/2} \hat{\mathbf{a}}\cdot\hat{\mathbf{p}} \tag{6.17}$$

where I is the irradiance of the incident beam, n_0 is the material's index of refraction and $\hat{a}$ is a unit vector parallel to the direction of the incident electric field. Using third-order perturbation theory we can express the 3PA rate as

$$W_3 = \frac{2\pi}{\hbar}\sum_{v,c}\left|\sum_{i,j}\frac{\langle\Psi_c|H_{\text{int}}|\Psi_j\rangle\langle\Psi_j|H_{\text{int}}|\Psi_i\rangle\langle\Psi_i|H_{\text{int}}|\Psi_v\rangle}{\left(E_{jv}(k)-2\hbar\omega\right)\left(E_{iv}(k)-\hbar\omega\right)}\right|^2 \delta\left(E_{cv}(k)-3\hbar\omega\right) \tag{6.18}$$

The index v corresponds to a valence band (initial state), c corresponds to the conduction band (final state) including spin, while i and j are intermediate states and can be any of the four bands considered, while the Ψ's are the respective Bloch wavefunctions. This means that the summation is performed over all valence to conduction band routes considering all possible intermediate states (same as the four bands in our model). From this, the 3PA coefficient $\alpha^{(3)}$ can

be obtained using the relation $\alpha^{(3)}(\omega) = 3\hbar\omega W_3 I^{-3}$ [43]. We performed our calculations over the entire wavelength range where 3PA is possible while 2PA is not possible (i.e. $E_g/3 \le hc/\lambda < E_g/2$). For each wavelength, we consider the transitions conserving the total energy and calculate the contributions to the 3PA coefficient arising from transitions from all three valence bands. This way, contributions from each of the three valence bands can be independently analyzed as well as their total effect which is the simple sum.

In practice, Eq. 6.18 takes a more complicated form which is shown below and has to be

$$\alpha^{(3)} = 3\omega \frac{(2\pi)^5}{(nc)^3}\left(\frac{eP}{\hbar\omega}\right)^6 \sum_{c,v}\left(\int_{\theta} \sin\theta\, d\theta\, k_{res}^2 \left(\left|\sum_{i,j} \frac{M_{cj}(k_{res},\theta)M_{ji}(k_{res},\theta)M_{iv}(k_{res},\theta)}{(E_{iv}(k_{res})-\hbar\omega)(E_{jv}(k_{res})-2\hbar\omega)}\right|^2\right)\frac{1}{\left|\frac{\partial E_{cv}(k)}{\partial k}\right|_{k=k_{res}}}\right) \quad (6.19)$$

evaluated numerically. For this, a Mathematica code was written, using as inputs only a few parameters such as bandgap and split-off energy, Kane parameter (or Kane energy) and refractive index, which is considered constant over the 3PA spectrum.

The numerical results obtained for room temperature ZnSe, with $E_g = 2.7\,eV$, $\Delta = 0.42\,\text{eV}$, $\text{E}_\text{P} = 24.2\,\text{eV}$, and $\text{n} = 2.49$ [72] are shown in Fig. 6.3 separating contributions from each valence band. Over the wavelength range considered we assumed no dispersion for the refractive index.

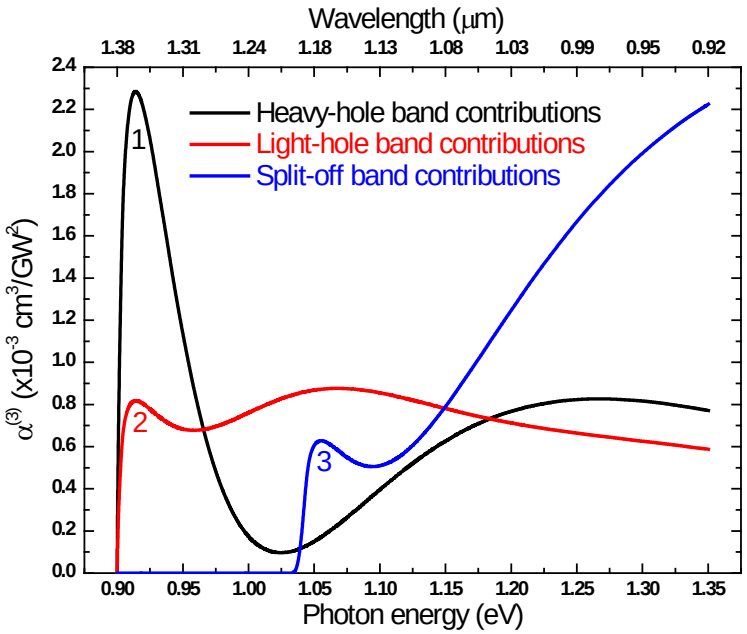

Figure 6.3 Contributions to the degenerate 3PA coefficient of ZnSe due to transitions from the (1) heavy-hole, (2) light-hole and (3) split-off band as a function of photon energy.

The most interesting feature common to all calculated spectra is the peak in 3PA at photon energies just above the onset of 3PA. The dip seen at higher energies is evidence of quantum interference. For each pair of initial and final electronic states separated by $3\hbar\omega$, there are several paths of evolution for the system. All these contributions add, with appropriate signs, while the measurable effect, the 3PA coefficient, is proportional to the absolute value of the sum squared. For example, the total contribution to the 3PA coefficient yielded by transitions from any of the valence bands is, in general, a sum of 256 terms. For the particular case of the heavy-hole band, there are only a total of 48 contributing non-zero terms, while for the other valence bands the number is larger. This happens because of the particular symmetries of the wavefunctions describing electronic states in the valence bands (band-mixing). This is apparent in the spectra calculated which show different magnitudes of the quantum interference effects depending on

the particular initial state (see Fig. 6.3). The coefficient at each wavelength can be greatly affected by this interference. As our calculations show, and as confirmed by our experimental data, choosing certain types of transitions to be dominant is not realistic when calculating these spectra, since several terms have a significant contribution in the summation.

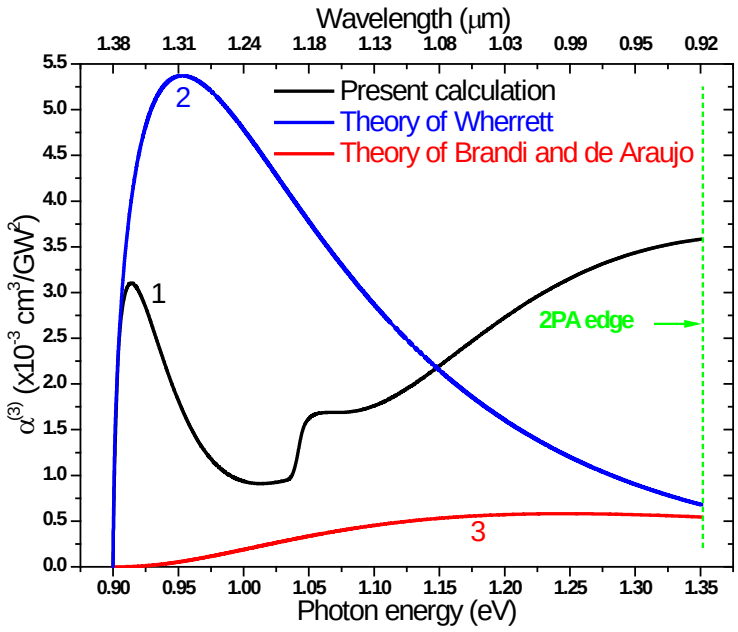

Figure 6.4 Calculated degenerate 3PA spectrum for ZnSe compared to previous theories of (2) Wherrett and (3) Brandi and de Araujo.

The previous theories [27, 43] using two-parabolic band models have predicted smooth, single peaked spectra as shown in Fig. 6.43, since these theories took into consideration only a restricted number of transition paths. Essentially, only *allowed-allowed-allowed* transitions between pairs of conduction and valence bands were considered by Wherrett [43], while Brandi and de Araujo [27] summed over transitions equivalent to *allowed-forbidden-forbidden*, *forbidden-allowed -forbidden* or *forbidden-forbidden-allowed* in our model. Simply adding the rates obtained by these previous calculations would ignore the interference effects.

These same types of calculations for the two-photon process were made by Hutchings and Van Stryland [41]. The spectra obtained (as our calculations confirm) were much smoother. The contributions from the split-off band produced a noticeable effect in the spectrum at the wavelength corresponding to a two-photon energy of $E_g + \Delta$, similar but smaller than the one seen in our 3PA spectrum. Nevertheless, the dip seen in the 3PA spectrum is absent in the calculated 2PA spectrum. This is understandable, in that for 2PA there is only one intermediate state required and consequently fewer evolution paths. Also, for this case, the *allowed-forbidden* and *forbidden-allowed* transitions are dominant terms and the interference has a much smaller effect.

The very good agreement shown for 2PA with two-parabolic band theories suggests that for this process, magnitudes and trends can be easily obtained using simple models. Unfortunately, this is no longer possible for 3PA spectra, and the full 4-band calculation is required.

3PA spectra were calculated for other cubic semiconductors and are shown in Fig. 6.5. Overall, the spectra have similar shapes but there are some differences arising from the specifics of the band structures. In particular, the feature due to transitions originating from the split-off band varies depending on the split-off energy. In GaAs, as compared to ZnSe, it is less pronounced since it appears further away from the dip, while in the case of narrow gap semiconductors (InAs, InSb), it is completely missing since these transitions would only be possible at much higher photon energies, within the 2PA spectra. For ZnS the split-off energy is very small, 0.07 eV [72], and thus this particular feature appears at about 980 nm, very close to the 3PA edge and just before the peak.

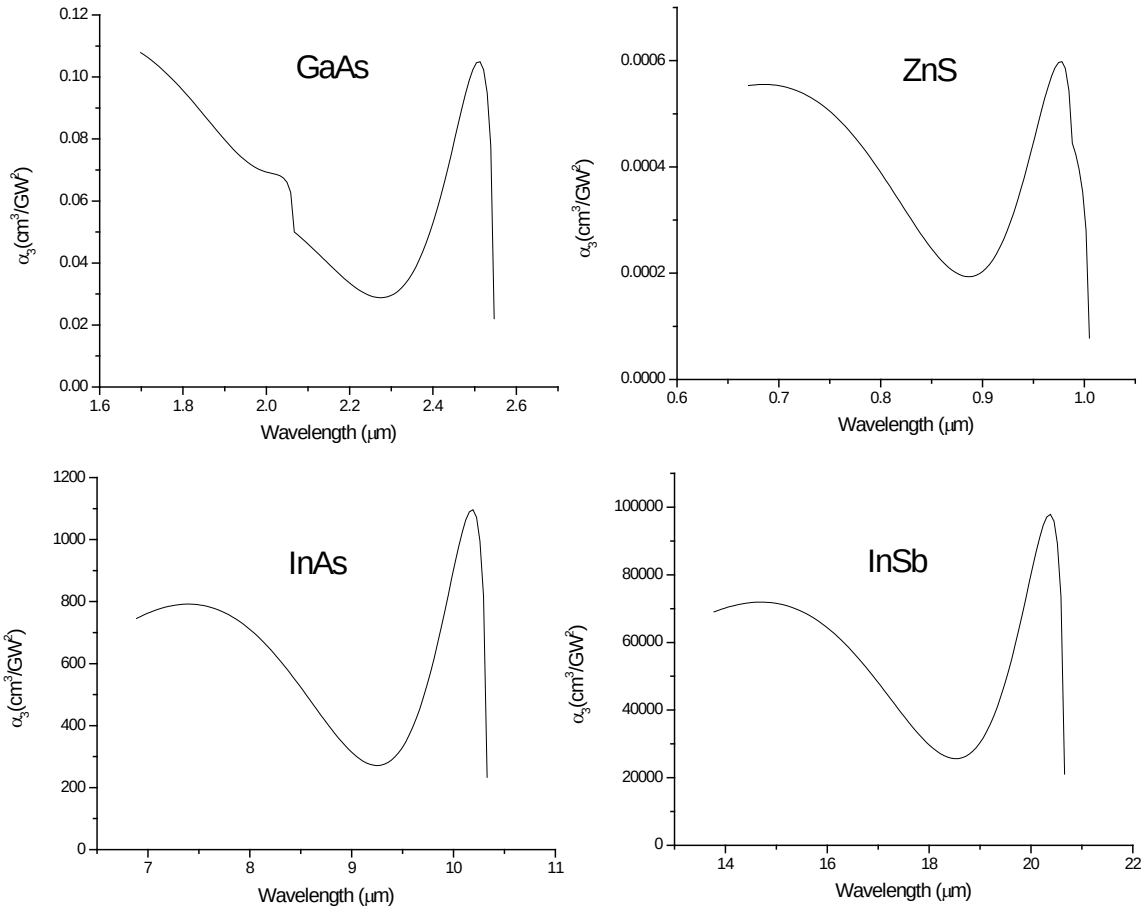

Figure 6.5 Theoretical spectra for GaAs, ZnS, InAs and InSb.

Such complex, numerically calculated spectral shapes pose difficulties when attempting to produce any type of scaling with the bandgap energy. However, specific trends related to the peak amplitude or positions of the peak and the dip can be identified through calculations. Also, by scaling the calculated 3PA coefficient with bandgap energy, Kane parameter and index of refraction we can obtain "effective" F3 functions for each semiconductor and a comparison is shown in Fig.6.6. We can see that the scaled spectra are similar around the peak and the dip. The major differences appear where the contributions from the split-off add. In particular, ZnS doesn't scale well since the three valence bands are almost triply degenerate at the Γ point.

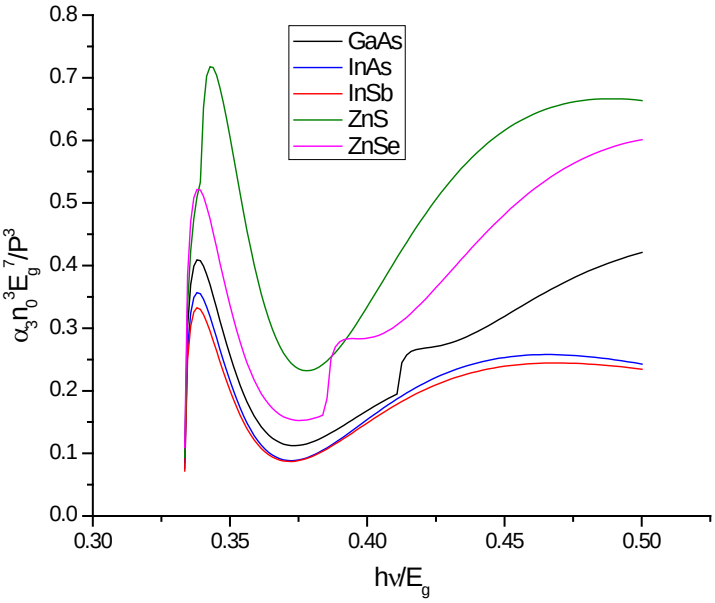

Figure 6.6 Comparison of scaled 3PA spectra for several semiconductors. The scaling is done using the refractive index, bandgap and Kane parameter, as shown.

6.3. Experimental data

In order to verify experimentally the calculations from the previous section, we used the femtosecond laser system and the parametric devices described in Chapter 3. For each wavelength we performed Z-scans at several energies on a 0.5 mm thick sample of CVD grown polycrystalline ZnSe purchased from Meller Optics. For the spot sizes used in our experiments, this sample is thin as defined by Kaplan [73]. We also carefully spatially filter the beam to obtain near Gaussian spatial profiles. At each wavelength we perform a detailed calibration to accurately determine the energy, the spot size and the pulsewidth (~140 fs) of the beam used.

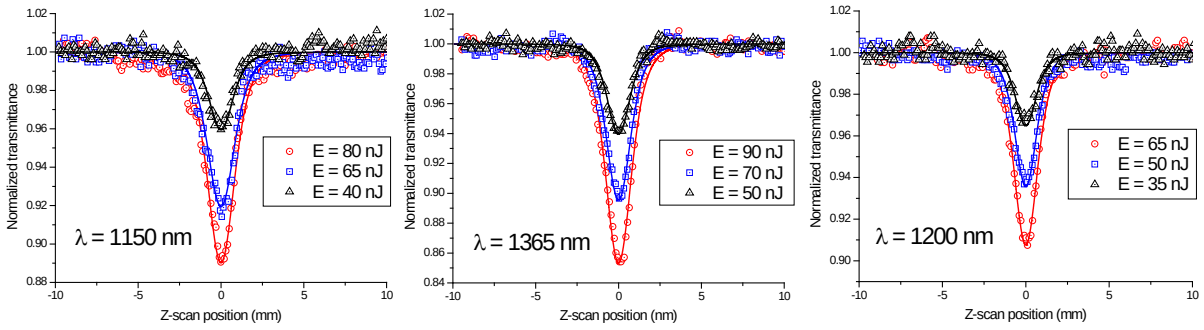

Figure 6.7 Typical experimental Z-scans of ZnSe taken at several wavelengths at the indicated energies.

The calibration is then checked by measuring 2PA in a known sample of CdTe with the same setup. Figure 6.7 shows some typical Z-scan traces along with theoretical fittings considering only 3PA at a few wavelengths. Each Z-scan curve is independently fit and the average 3PA coefficient for the energies s used is calculated. It is important to mention here that the values obtained from fitting individual sets of data are within ±10% of the average, suggesting that only the 3PA process is present for femtosecond pulses, with a negligible contribution from free-carrier absorption or other effects. Also, even though the absolute errors (in energy, spotsize and pulsewidth) of our measurements are estimated to be about ±35%, the

relative errors are smaller, increasing our degree of confidence in the relative magnitude of the features for the measured spectrum of ZnSe (Fig.6.8 (a)).

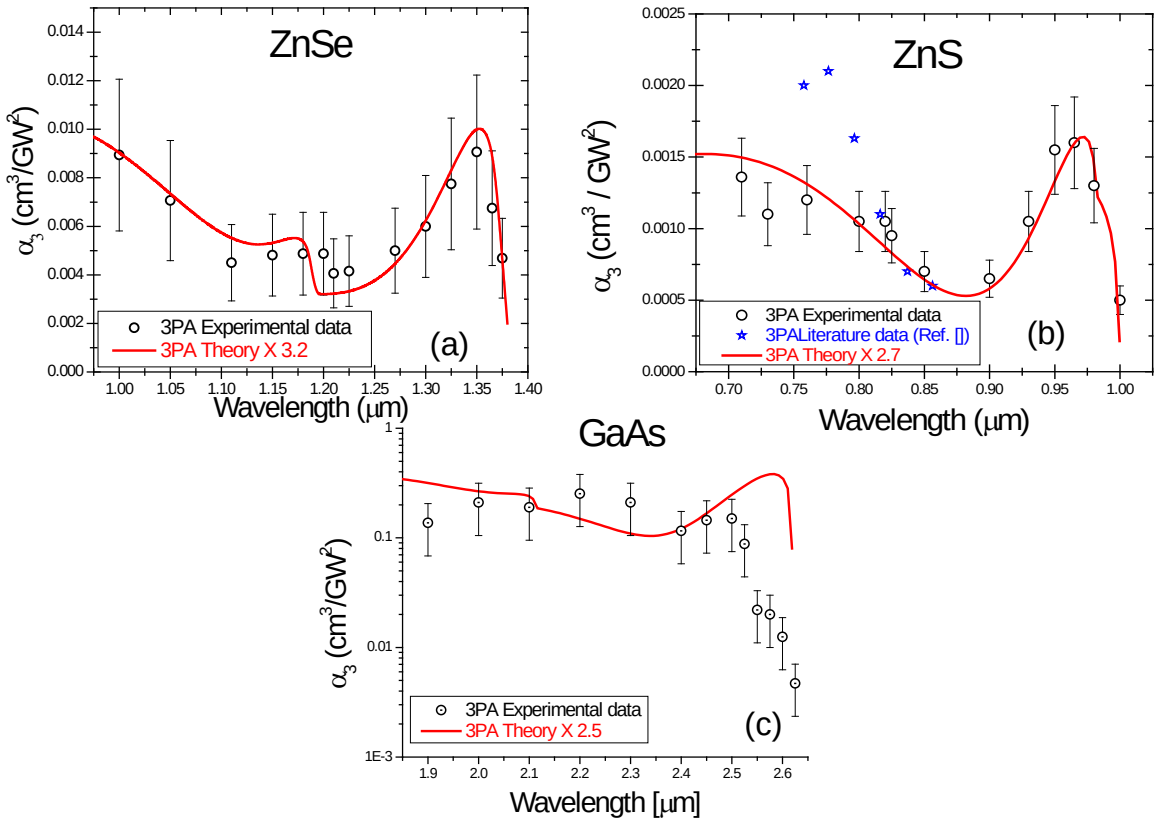

Figure 6.8 Experimentally obtained 3PA spectra of of ZnSe (a), ZnS (b) and GaAs (c), compared to our calculations.

A similar experimental procedure was employed for ZnS and GaAs. The data was taken by Peter Olszak and Trenton Ensley [74] and is shown in Fig. 6.8 (b) and Fig. 6.8 (c), respectively, together with some literature values. For ZnS, the spectral range studied is similar and we obtain very good agreement. For GaAs, the larger spectral width of our pulses (over 100 nm) complicates the comparison to the theory. A better analysis of the data can be done using the femtosecond pulse spectrum at each measured wavelength, yielding a reasonable agreement with the theoretical spectrum [74]. However, great care should be taken when using such linear

approaches for nonlinear spectra as these yield only approximate results at best, since the multiple frequencies in the spectrum can contribute in a non-degenerate manner to the overall measured magnitude.

6.4. Discussion of results

In the previous section, plots of our measured values for $\alpha^{(3)}$ are shown along with our theoretical calculations. The best match to our experimental data for ZnSe is obtained when using in our calculations 2.71 eV and 0.37 eV for the band-gap and split-off energies, respectively. Similarly, a bandgap value of 3.7 eV was used for ZnS and of 1.49 eV for GaAs. These energies are within the range of previously published values [72]. There is an overall discrepancy in absolute magnitude of $\alpha^{(3)}$, which is ~3.2 for ZnSe, ~2.7 for ZnS and ~2.5 for GaAs, respectively. In the plots, our calculated values are multiplied by the respective factors to allow for easier comparison. As can be seen, there is very good agreement between the experimental data and our theoretical calculations and the predicted dip is evident in the measured values. Also, the contribution from transitions due to the split-off band is apparent in the experimental data taken in ZnSe. An important aspect is the trend in the 3PA values as the wavelength gets closer to the 2PA edge. The previous theoretical work [27, 43] suggested smaller magnitudes for the 3PA coefficients as the wavelength gets closer to the 2PA edge, with decreasing values for increasing wavelengths. Our calculations and experimental data show that close to the 2PA edge the 3PA magnitude is in fact larger by almost an order of magnitude than what was previously estimated and has the opposite (increasing) trend.

This theory agrees with Wherrett's calculations close to the 3PA band edge since the allowed-allowed-allowed transitions dominate there and the band mixing effects are minimal. The rather remarkable fit of the spectral shape coupled with the relative closeness of the overall magnitude (within a factor of 3.2) shows that the essential physics of the interaction is well accounted for. However, the reasons for the discrepancy in absolute magnitude probably still arise primarily from the limitations of the theoretical model. The original model assumed a temperature of 0K and even though we use the room temperature values for the material parameters, we consider an empty conduction band with full valence bands. Also, away from the zone center, there should be less accuracy when predicting the band shapes using Kane's model since the calculated band structure deviates from measurements. In particular for ZnSe, this happens at ~1 eV above the band edge, corresponding to energies of about 330 meV above the 3PA edge [41, 72]. A better model needs to be used in order to obtain a more accurate shape for the conduction band and the heavy-hole band (parabolic here with an effective mass equal to the electron rest mass). For example, the model used by Hutchings and Wherrett [24] to describe anisotropy of the 2PA coefficient takes into consideration the effects of higher conduction bands. Such models should also allow for calculation of the anisotropy of the 3PA coefficient, as well as yield a more accurate value for the effective mass of heavy holes. For single crystal GaAs the anisotropy of the 3PA coefficient was reported in Ref. [61]. Nevertheless, such a detailed calculation, even though possible, would be considerably more complex for 3PA. Other factors possibly affecting measurements of 3PA are impurities, defects, and also excitonic effects for wavelengths close to band-gap resonance [75]. However, we believe that these would produce small changes to the overall relative shape of the calculated spectrum.

In conclusion, the degenerate 3PA spectra for several zincblende semiconductors were calculated using third-order perturbation theory based on a Kane band structure consisting of three valence bands (heavy-hole, light-hole and split-off) and a conduction band. This model is realistic for these structures since it accounts for the non-parabolicity of the bands and non zone-center wave functions obtained using Kane's $\mathbf{k}\cdot\mathbf{p}$ theory. It should be pointed out here that ideally, this model can be extended to other symmetries as well. The results obtained for cubic structures match the measured spectral shapes recovering all the details predicted although the predicted absolute magnitude is a factor of ~3 smaller than the experimental data, on average. The predicted dip in the 3PA spectrum due to the quantum interference effects and the onset of the contributions from the split-off band occur in a range close to the zone center where our theoretical description is fairly good. Further away, the non-parabolicity of the bands is probably insufficiently accounted for. However, the features aforementioned can be predicted only when a full calculation is performed. Simpler models cannot produce similar results since band-mixing and all possible evolution paths are not properly taken into consideration. Such calculations should be important for applications such as terahertz generation [61]. In these cases, intense femtosecond pulses experience significant losses through 3PA and ideal spectral ranges can be identified to minimize these unwanted effects.

CHAPTER 7: OPTICAL NONLINEARITIES IN InSb

Indium antimonide (InSb) is a direct band gap semiconductor from the III-V group of compounds comprising binary mixtures of elements from groups IIIb (B, Al, Ga, In, Tl) and Vb(N, P, As, Sb, Bi). The crystal structure of III-V semiconductors is a cubic, zincblende kind of structure. An average of 4 valence electrons per atom gives a tetrahedral bonding structure. This leads to a crystal lattice of two interpenetrating face-centered cubic cells.

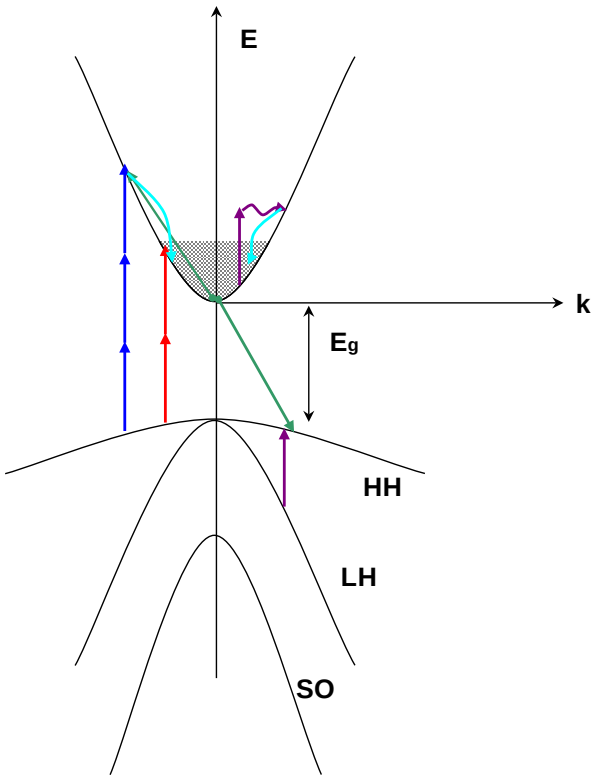

Figure 7.1 Band structure used for InSb showing some of the physical phenomena that can be investigated by optical means (2PA, 3PA, FCA and Auger recombination).

The band structure was calculated by Kane [23] using $\mathbf{k}\cdot\mathbf{p}$ theory. Several other publications addressed the non-parabolicity of the bands and these more involved treatments were further used to calculate other parameters of interest like nonlinearity, free-carrier

absorption, Auger coefficients, etc.(see for instance Ref. [76]). For the purpose of this work, we chose the standard Kane model. The main features are a single conduction band and three valence bands (Fig. 7.1). Two are degenerate at $k = 0$ and correspond to the so-called light and heavy hole bands (due to different parabolicity, or "effective mass") while the third one is the split-off band. In general, the conduction band is taken to be isotropic but non-parabolic.

At 77 K the bandgap is 0.23 eV while at room temperature it becomes 0.175 eV placing the linear absorption edge at about 7 μm. This range made InSb a promising material for nonlinear optical limiting in the operating range of CO_2 lasers, close to the peak 2PA of InSb, raising the interest toward characterizing its nonlinear optical properties [77].

The temperature dependence of the bandgap energy can be estimated using

$$E_g(T) = E_g(0) - aT^2/(b+T) \tag{7.1}$$

with a =0.6 meVK^{-1} and b =500K [72].Taking into account a Fermi distribution for electrons (and holes), we can calculate the thermal population of carriers. This yields densities of about $2*10^{18}$ cm^{-3} which produce large linear losses through intra-conduction band absorption (small due to phonon-assisted transitions) and inter-valence band absorption (large due to direct transitions between the light and heavy-hole bands), for mid-IR wavelengths higher than 7 μm (see Fig. 7.5). The cumulative free-carrier absorption cross-section is about $8*10^{-16}$ cm^{-2}, about 2 orders of magnitude larger than the typical values for large gap semiconductors [33]. The 2PA at these wavelengths is also extremely large, and this has been shown through the developed scaling laws for semiconductors [8] and confirmed experimentally [12, 14, 78]. This poses problems when doing nonlinear measurements since one has to deal with a complex interaction between the bound electronic effects (instantaneous nonlinearities) and the free-carrier ones (a

byproduct of the instantaneous effects and longer lived states). Unfortunately, except when using the shortest of pulses (fs) the free-carrier effects dominate their instantaneous counterparts making the extraction of reliable values a difficult process, reflected in the large dispersion (over 2 orders of magnitude) of the reported values in the early papers [8].

Over the years, the reported values appeared to converge towards smaller numbers, but when analyzing the experimental data it was common to assume/use for 2PA a value of ~2 cm/MW regardless of the wavelength, without doing a proper analysis. The scarcity of the laser sources in this range coupled with the use of larger pulsewidths were some of the adverse factors in the determination of the optical properties. To complicate the problem even more, the pyroelectric detectors which were often the detectors of choice, aren't sensitive to energies under 0.3 μJ and some experiments with shorter pulses had to employ large input energies, rendering some of the conclusions drawn inaccurate [12, 78]. Liquid N_2 cooled CdHgTe detectors offer a much better sensitivity as they can detect much lower energy levels, of the order of pJs. However they are typically only available in small area packages (less than 16 mm^2) since homogeneity is a problem and a careful determination of linearity ranges (or an accurate calibration) is necessary.

In this chapter we present a series of experiments using a large range of pulsewidths aimed at explaining physical phenomena seen at different wavelengths and with various response times. The idea is to quantify both the instantaneous and cumulative effects on a strong irradiance beam propagating through this narrow gap semiconductor. To better understand the approach used, we will write a set of coupled equations describing the variation of the irradiance and phase of an incident beam, together with an equation describing the temporal evolution of the density of photo-generated carriers as follows

$$\frac{dI(z,r,t)}{dz} = -\alpha_2 I(z,r,t)^2 - \sigma_{abs} N_{ph}(z,r,t) I(z,r,t) - \alpha I(z,r,t) \tag{7.2}$$

$$\frac{d\Phi(z,r,t)}{dz} = k(n_2 I(z,r,t) - \sigma_{ref} N_{ph}(z,r,t)) \tag{7.3}$$

$$\frac{dN_{pg}(z,r,t)}{dt} = \frac{\alpha_2 I(z,r,t)^2}{2\hbar\omega} - \frac{N_{pg}(z,r,t)}{\tau} - C_{Auger} N_{pg}(z,r,t)(N_{pg}(z,r,t) + N_0)(N_{pg}(z,r,t) + 2N_0) \tag{7.4}$$

In these equations, the free-carrier absorption and refractive cross-sections σ_{abs} and σ_{ref} are taken as the sum of their respective electron and hole contributions, α is the linear absorption coefficient which accounts for the absorption of thermally generated carriers and of any of the impurities present, τ is the natural lifetime and C_{Auger} is the Auger coefficient. It's easy to see that when all these effects are non-negligible the nonlinear interaction is relatively complex and exact determination of all parameters involved is difficult. Therefore one needs to find specific configurations which would greatly minimize certain contributions, hence simplifying the problem. For instance, the use of very short pulses (femtosecond) would produce negligible free-carrier densities (proportional to the pulse duration) which hopefully would allow us to neglect any cumulative effects. This way, one can measure 2PA and any refractive effects associated to the $\chi^{(3)}$ term. With these parameters independently determined, we can then use longer pulses resulting in larger photo-generated carrier densities. Consequently, we can determine the respective absorptive and refractive cross-section using the methods described in Chapter 3. Lastly, using a time-resolved experiment, one can study the time dynamics of the photo-generated carriers making use of their absorptive properties, yielding characteristic lifetimes. The experiments presented in the following sections follow this general approach and partial conclusions and comments on the results obtained will be mentioned in each section.

7.1. Experimental calibration

In order to extract reliable values from the measured data, a careful calibration of the experiment needs to be done. An independent determination of beam parameters, pulsewidth, size, input energy and spectrum, should be done in order to minimize as much as possible the inherent experimental errors. Last, but not least, the response of the detectors used should be fully characterized as a function of the input energy. Data should be taken in the detector linearity range if possible or a response curve needs to be constructed based on a known reference. These issues are discussed in the following paragraphs.

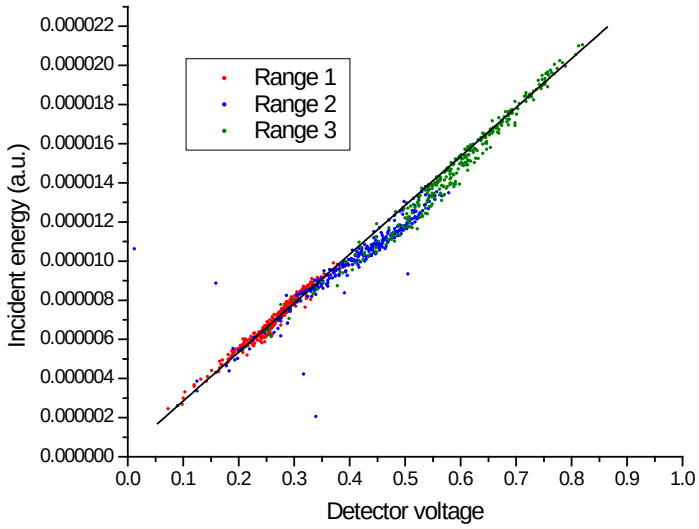

Figure 7.2 Detector response vs. input energy. Each point represents a single shot.

Signal detection in our picosecond and femtosecond experiments was done using a pair of liquid N_2 cooled CdHgTe 4X4 mm photo-conductive detectors kept in vacuum and having Ge AR coated windows. The response time of these detectors is about 10 μs and they offer a sensitivity of the order of pJ/V which is ideal for experiments using short pulses and low input

energies. The larger energies were measured with a calibrated Molectron and a PE-9 Ophir pyroelectric sensors. Within the calibrated range they are quoted to have a maximum deviation from linearity of about +/-5%. Unfortunately, when compared directly with each other, the values differ by about 25% to 30%. Therefore only one was chosen (Molectron sensor) to serve as a reference for all our experiments, as its calibration was verified directly at the company. However, because of better readout capabilities, the Ophir PE-9 sensor was used to verify the linearity range of out CMTs, by doing a relative measurement. This data is shown in Fig. 7.2.

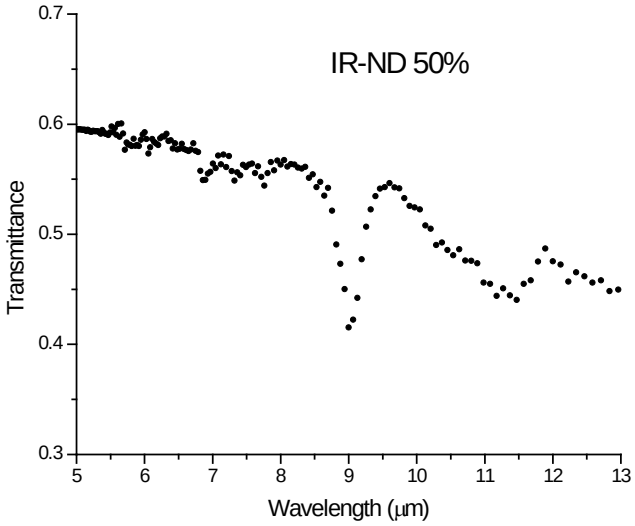

Figure 7.3 FTIR spectrum of a neutral density filter from Janos Technology with an average transmission of 50%.

Input energy variation was done using BaF_2 wire-grid polarizers from Specac and a set of calibrated IR neutral density filters from Janos Technology. These filters were extremely useful in reducing the energy incident on the detectors in the picosecond experiments since the input energies for these experiments were generally in the nJ range. For the femtosecond experiments we avoided using these filters however because their spectral response is not flat over the bandwidth of the pulses as can be seen in Fig. 7.3. For these experiments, we exclusively used

the wire-grid polarizers which assured a constant pulse broadening over the range of energies used, since the pulses were traveling through the same material thickness. For the polarization resolved experiments, we used the same polarizers in conjunction with a Babinet-Soleil compensator from Special Optics.

The spatial characterization of the optical beams was done through knife-edge beam scans (Fig.7.4 (a) and (b) or pinhole scans (Fig 7.4 (c)) for the time resolved measurements. The pinhole scans were usually de-convoluted as the pinhole sizes were not much smaller than the measured beam sizes.

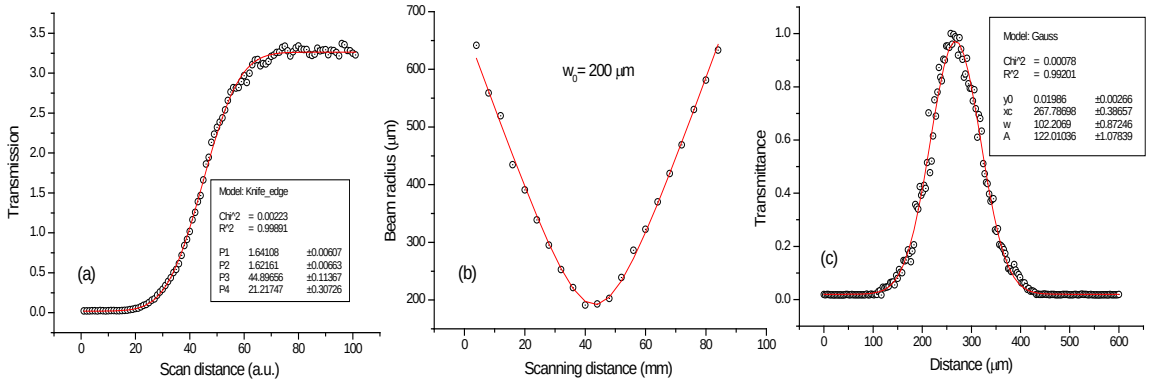

Figure 7.4 Beam characterization. Knife-edge scan (a) with a Gaussian fit (b) and pinhole scan (c).

The temporal profile of the pulses was obtained through fitting of the time-resolved data taken with perpendicular polarizations in a frequency degenerate scheme. These experiments allow for the separation of the free-carrier effects and measurement of the pulse duration making use of the instantaneous absorptive effects (see for example Fig. 7.19). The error in the pulsewidth measurements was estimated to be as much as $\pm$10%, with energy collection being the main source of error due to defocusing effects due to the photo-generated carriers, since pulsewidth measurements were relative measurements.

The spectral bandwidth of the femtosecond pulses was measured with a 1/8 m Oriel monochromator using a gold coated grating with 150 lines per mm. The spectra had widths of several hundreds of nm in the 8 to 11 μm range. For the picosecond pulses, the resolution was too small to reliably measure any spectra, but knowledge of the bandwidth wasn't really necessary at these durations.

The sample used for experiments (from AFRL) was intrinsic, (100) cut, AR coated on both sides and with a 450 μm thickness. The transmission and absorption spectra were determined experimentally (see Fig. 7.5) while the crystal orientation was verified by X-ray diffraction experiments.

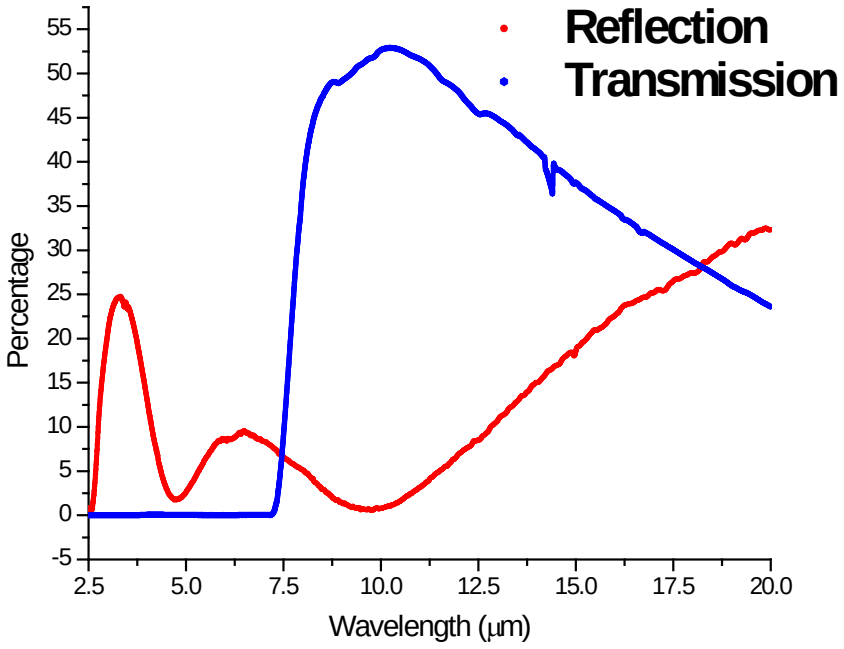

Figure 7.5 Reflection and transmission spectra for AR coated 450 mm thick InSb sample.

7.2. Femtosecond experiments

The femtosecond TOPAS system described in Chapter 3 was used to pump a 1 mm thick $AgGaS_2$ crystal. Through a DFG process using the idler and the signal beams in an (eoo) geometry, infrared beams are generated in the range from 3 to 11.5 μm. The optimal temporal overlap of the idler and the signal is obtained by rotating a piece of quartz before the crystal. The upper wavelength is however set by the linear absorption in the crystal. The output energies are in the range of a few μJs and a typical beam profile is shown in Fig. 7.6. Separation of the IR beam was done in two stages. First a 1 mm ZnSe coated piece was used at 45 degrees incidence angle. The coating strongly reflected the near-IR inputs and strongly transmitted the mid-IR.

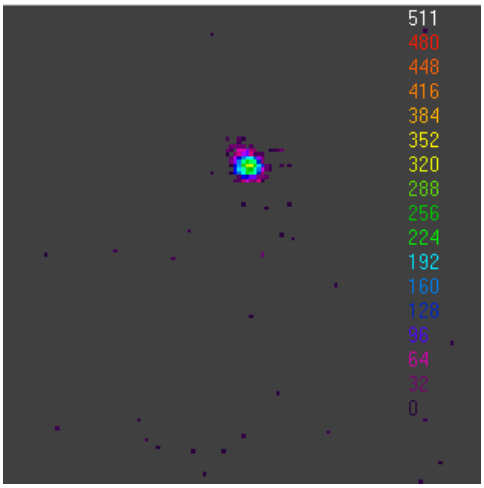

Figure 7.6 Femtosecond beam profile at 4 μm.

Secondly, a 1 mm piece of Ge was used at the Brewster angle for the p-polarized IR beam allowing maximum transmission. The germanium absorbs any residual pump beam as its wavelength is always lower than 1.7 μm.

A monochromator was used to measure the spectral widths of the pulses in the mid-IR range and the spectra obtained are shown in Fig. 7.7. We can see that Gaussian functions describe

fairly well the spectra of the pulses. At 8 μm there is a dip in the spectrum that has the same position as we tune the wavelength. The reason for its presence is still unclear while similar behavior has been observed in other systems from Light Conversion [79], suggesting possible issues with either the crystal or with the coating.

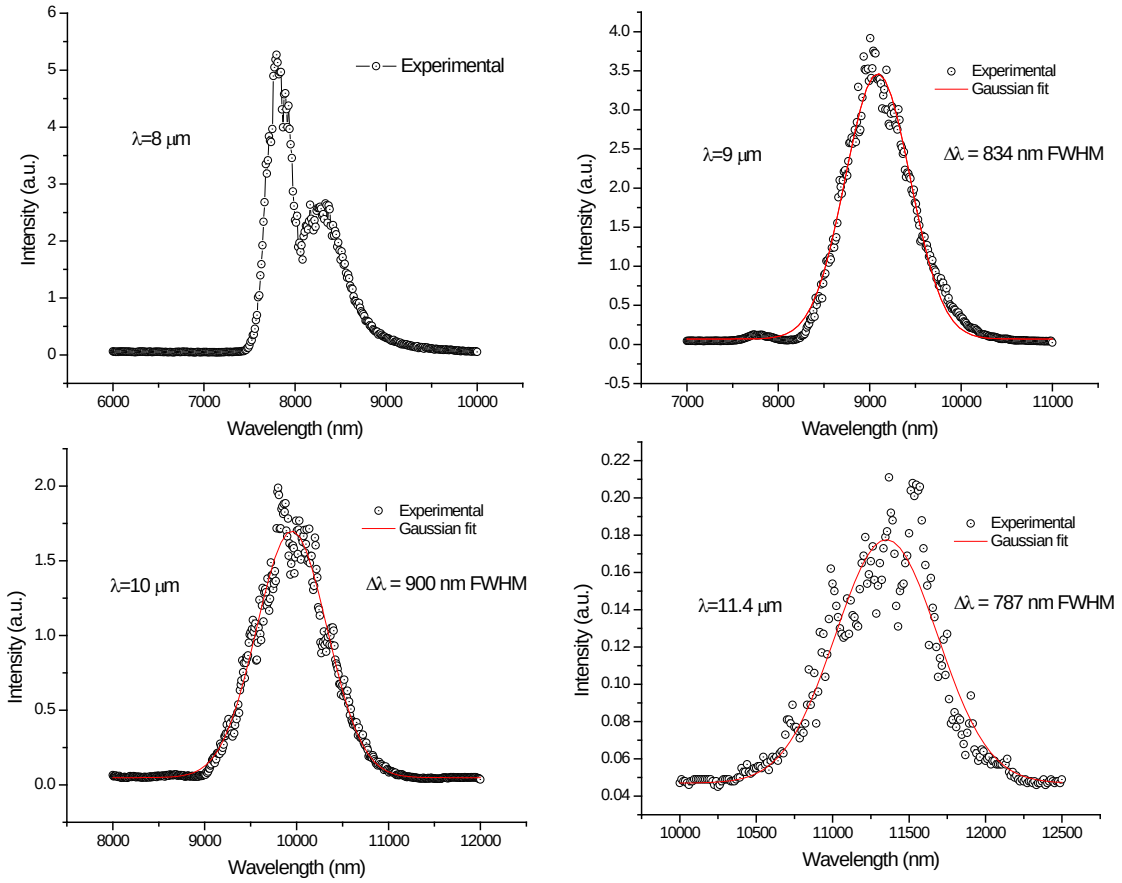

Figure 7.7 Measured spectra of the femtosecond IR pulses.

A temporal characterization was attempted using an old 300 μm area InSb detector as a 2PA based photo-voltaic detector in a Michelson configuration. Unfortunately, the response wasn't quadratic in input irradiance, possibly due to absorption by impurities. Consequent attempts made by P. Olszak to measure the temporal widths at slightly shorter wavelengths using a PbS

detector were also unsuccessful. In order to analyze the Z-scan data, we assumed a transform limited pulse at the output of the crystal, which is reasonable since both the idler and the signal beams are close to transform limited [80]. For each configuration we calculated the amount of broadening induced by the optics in the path of the beam before the sample and estimated the pulsewidth at the sample. The attenuation of the beam was done using two wire-grid polarizers to insure the same amount of broadening for each irradiance level used. The energies used in our experiments were very low, from hundreds of pJ (detection limit) to a few nJ. The energy calibration was done using an Rk-5100 pyroelectric radiometer. Even at such low energy levels, our pulses were short enough to give very large input irradiances and consequently producing very large changes in transmittance, over 50% in most of the cases.

In principle, analyzing the open-aperture data doesn't pose too many problems. Things are rather different when trying to measure nonlinear phase shifts over such large absorptive signals. As mentioned in Chapter 3, a Matlab code was written in the thin sample approximation which

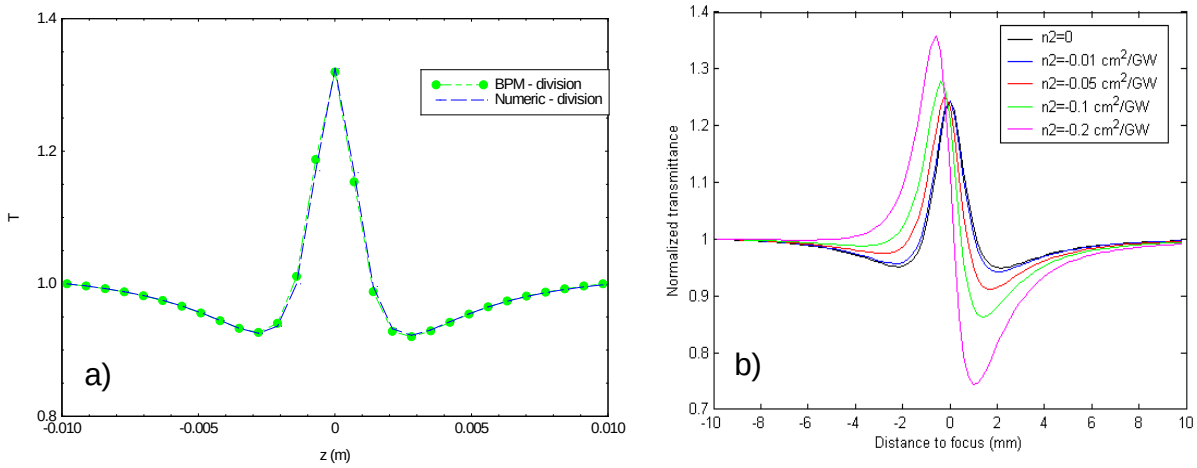

Figure 7.8 Numerical modeling of ratio of closed to open-aperture Z-scans for no self-phase modulation effects. Results are compared to (a) full BPM code calculations and (b) extended for several n_2 values.

assumes a cylindrical symmetry for our beams and propagates the field to the aperture plane using a Fresnel-Huygens formalism. The effects of such large absorption levels are exemplified in Fig.7.8. The first theoretical plot (a) shows the division of the open and closed aperture scans for large absorption which yields a fairly strong signal, added to any refractive signal. The theoretical curve was compared to the full beam propagation code developed in our group, confirming the validity of the calculated results in the thin sample approximation. The second theoretical plot (b) shows the division of closed and open-aperture curves for the strong absorption case and different values of n_2. A large Kerr coefficient is needed to produce the expected shape. The explanation for the peak in Fig. 7.8 (a) is rather straightforward. Simply put, a beam which will be strongly absorbed will tend to flatten as the largest irradiance

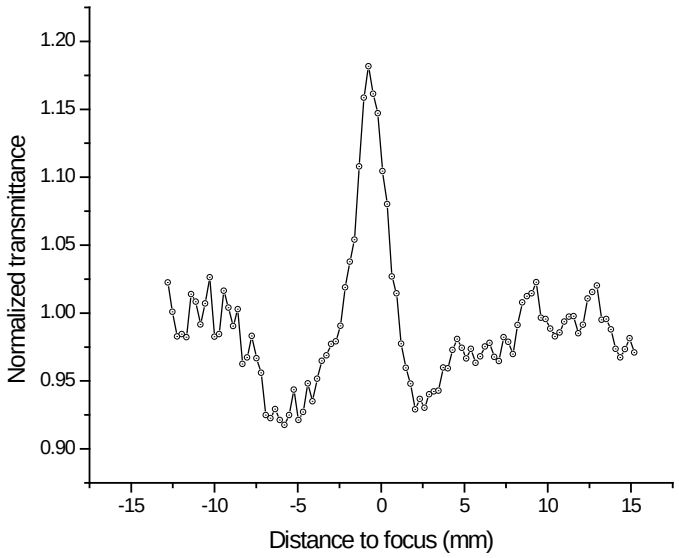

Figure 7.9 Division of closed and open-aperture scans at 10 μm in InSb using ~200 fs pulses and a focused spot size of 50 μm at room temp.

levels are on-axis. A flattened beam will have a narrower distribution in the far-field (Fourier transform) which would produce a larger transmitted signal through the aperture. A signal similar to the theoretically generated curve was recorded at 10 μm as n_2 was expected to be 0 or extremely small and is shown in Fig.7.9. One conclusion that can be drawn here is that large absorptive effects may put a limit on the measurable Kerr coefficient.

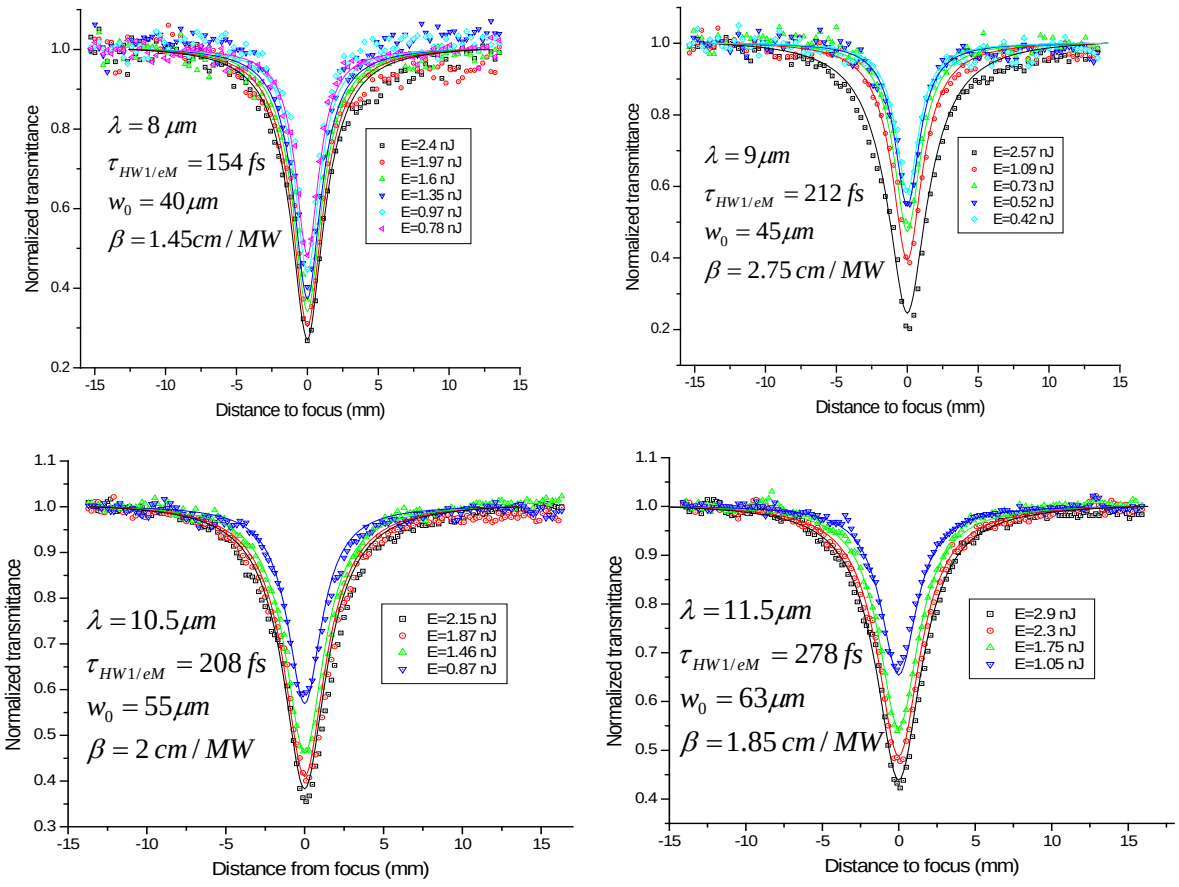

Figure 7.10 Open aperture Z-scans performed with femtosecond pulses at several wavelengths as shown on the figures. The respective parameters shown are used to generate fits for all individual energies.

We performed open and closed-aperture Z-scans at several wavelengths between 8 and 11.5 μm. The open aperture scans are shown in Fig. 5.10. The data were fit with the same parameters

shown in the respective captions, yielding 2PA values of about 2 cm/MW. From analyzing the data we can say that even for the maximum recorded signals the absorptive effects due to the photo-generated carriers were minimal as the densities produced by our short pulses were fairly small, consistent with our theoretical calculations. Our assumption of transform limited pulses yields a minimum possible pulse duration at the sample effectively setting a lower limit for the extracted 2PA magnitudes. A chirped pulse out of the $AgGaS_2$ crystal would have been broadened more, decreasing the irradiance and increasing the value measured. In conclusion, we can say that given our uncertainties in measuring the pulsewidths, the 2PA is not less than the measured values, but possibly larger by not more than about 30%. Of course, considering also the uncertainties when measuring the energy and beam width results in about $\pm$ 15% error in the absolute values, yielding a total uncertainty range from -15% to +45% for the absolute values.

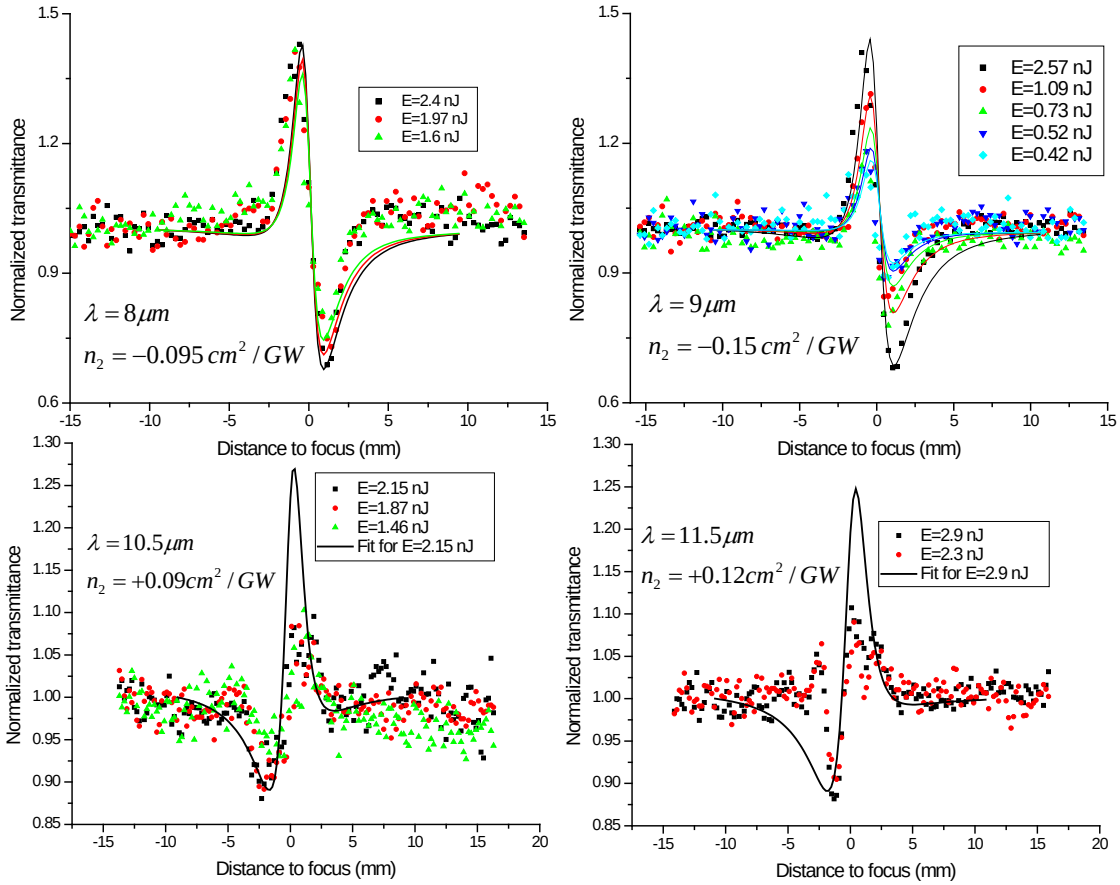

Figure 7.11 Experimental and theoretical curves showing nonlinear refraction in InSb at several wavelengths using femtosecond pulses. The indicated n_2 values are used to generate all the theoretical curves on the respective plots.

The ratios of the closed to the open-aperture scans are shown in Fig. 7.11. At 8 and 9 μm the shape denotes a negative n_2 (defocusing nonlinearity) as expected for these wavelengths. The data was however noisy and as the absorptive effects were extremely large, we should not consider the extracted values as very reliable. Overall, as in the case of open aperture scans, as much as the data allows such a conclusion, we can also say that the refractive effects due to the free-carriers are minimal. For the very low energies used the difficulties associated with the alignment of the setup can influence negatively the quality of the data. Data taken at 10.5 and

11.5 μm seems to indicate a positive n_2 (focusing nonlinearity). The noise in that data is even larger; however, we do believe that at least qualitatively we have shown the predicted change in the sign of the Kerr coefficient. For these longer wavelengths we generated theoretical curves using a positive n_2 at the largest energy to allow for some comparison to the experimental data. These curves shouldn't be considered as fits but rather a way of estimating an upper value of n_2.

The use of such broadband pulses should in general raise questions about the meaning of the extracted values for 2PA and the Kerr coefficients. The 2PA theoretical spectrum is fairly flat in the studied range and for pulses not extremely chirped our extracted values are meaningful. In the case of n_2 however, there's a large predicted dispersion around the 0 crossing point (around 10 μm) and much better quality data should be used to allow for definitive conclusions. The largely different frequencies in the pulses' spectra would experience very different focusing or defocusing effects. Effectively, "de-convoluting" such effects may prove difficult and a better approach would be to use the spectrum information in the analysis procedure. As mentioned, even though the phase measurements can be considered only qualitatively good, the 2PA measurements yield usable values, which set the lower possible level of 2PA coefficients and, as we will see, these values are consistent with data taken at longer pulsewidths.

7.3. Picosecond experiments

The femtosecond measurements have shown, as expected, minimal effects from the photo-generated carriers (absorptive or refractive) which allows for a direct measurement of bound electronic nonlinearities (α_2 and n_2). For the ~10 picosecond pulses available from our EKSPLA system comparable irradiances would produce much larger densities of electrons (and holes), by

about 2 orders of magnitude. For the absorptive measurements, decoupling can be achieved through time-resolved experiments, while the single beam techniques (Z-scan) are also used to characterize the relative contributions to the nonlinear change in index.

An important aspect that needs to be mentioned here is the anisotropy of the $\chi^{(3)}$ tensor. In general, whether we do single beam or two-beam experiments, the magnitudes of the measured nonlinear coefficients depend on the polarizations of the beams and the particular crystal cut. For the single beam case, "effective" 2PA coefficients will be expressed as a function of the non-zero $\chi^{(3)}$ tensor components and the anisotropy coefficient, for the standard (100), (110) and (111) cuts. Similarly, for the time resolved experiments, expressions of the respective 2PA coefficients will be given for parallel and perpendicular polarizations of the pump and probe beams.

7.3.1. Z-scan experiments

Given the importance of FCA in the picosecond experiments a proper characterization of the absorptive properties of the thermally generated carriers needs to be made. FTIR measurements were done using a N_2 cooled Joule-Thompson cryostat from MMR. Transmission spectra were recorded at several temperatures and the results are shown in Fig. 7.12. The population densities for each temperature were calculated using a Fermi-Dirac distribution and the behavior of the free-carrier absorption cross-section was estimated as a function of temperature and wavelength. The FCA was generally assumed to not depend on temperature. This turns out to be incorrect as discussed by Peter Olszak in Ref. [74]. This was based on the experiments of Kurnick and Powell [81], who studied it using several p and n-doped samples. Some previous nonlinear studies in InSb also used these results in the analysis performed [13, 78]. Newer theoretical

calculations [76, 82] emphasized however the importance of occupational factors at different temperatures in the calculation of both FCA and 2PA in InSb. The experimental results confirm the predicted dependence of FCA of wavelength and temperature [82].

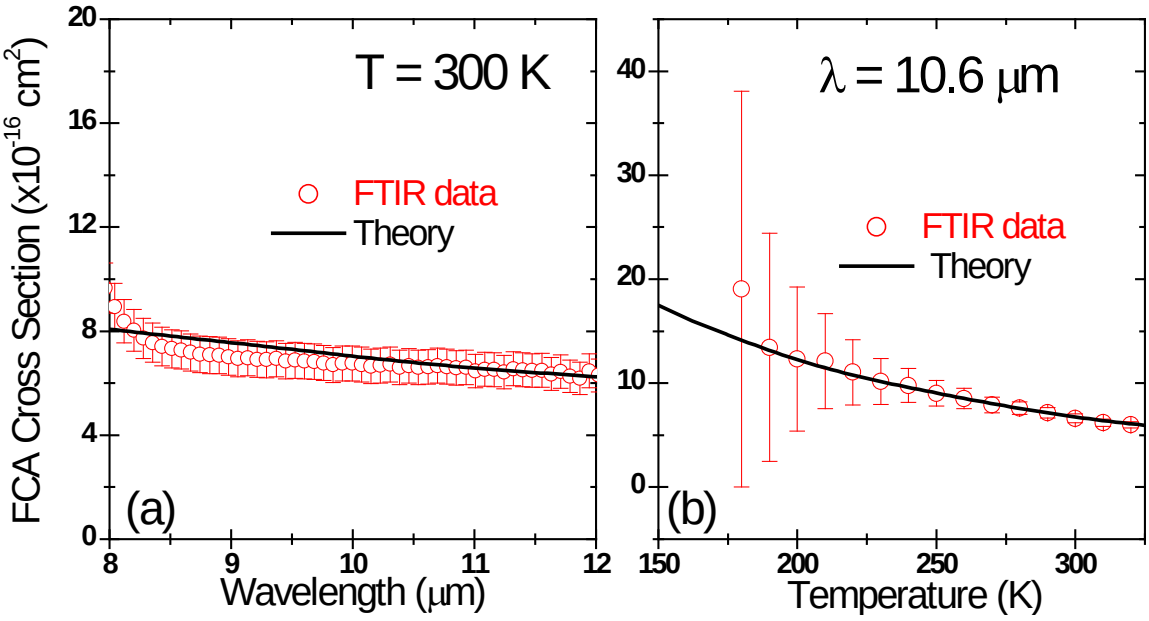

Figure 7.12 Experimental dependence of FCA with wavelength (a) and temperature (b). The theoretical values are obtained from Ref. [82].

A simple analysis regarding the relative contributions to absorption due to free carriers and bound electronic effects for the case of an arbitrary pulse duration can be made [77, 83]. Assuming that the pump is not significantly depleted we can write the free-carrier generation rate as proportional to the irradiance squared

$$\frac{dN}{dt} = \frac{\alpha_2 I^2}{2\hbar\omega} \tag{7.5}$$

and equating the two loss terms in the propagation equation we obtain

$$\alpha_2 I^2 = \sigma N I \approx \frac{\sigma \alpha_2 I^3 \tau}{2\hbar\omega} \tag{7.6}$$

where τ is the pulse duration. This way we can define the "critical" irradiance [83] as

$$I_{cr} = \frac{2\hbar\omega}{\sigma\tau}\ldots \tag{7.7}$$

It's important to note here that the value of the "critical" irradiance is independent of the 2PA coefficient and inversely proportional to the pulse duration. Experimentally, the use of irradiances smaller by at least an order of magnitude than the "critical" irradiance should result in minimal contributions to absorption from the free-carriers. Given a 2PA coefficient this "critical" irradiance level would produce a "critical" two-photon signal. If the measured signal is much smaller than the signal obtained at the "critical:" irradiance it can be safely assumed to be due to 2PA alone. For the 10 ps pulses used we obtain a value of about 2 MW/cm^2, which would yield a signal of about 6% in a Z-scan experiment for InSb. Assuming a minimum measurable signal of about 2 to 3% we can therefore conclude that in the picosecond experiments FCA will play an important role. As seen in the previous section, for the femtosecond pulses, shorter by about a couple of orders of magnitude, FCA can be neglected.

Another important aspect related to 2PA is understanding how the experimental configuration affects the values measured. The polarization state of an incident beam on particular crystal orientation determines the strength of the nonlinear interaction. For the zincblende structures ($\bar{4}3m$ class) there are a total of 21 non-zero $\chi^{(3)}$ tensor elements out of which 4 are independent components denoted by $\chi^{(3)}_{xxxx}, \chi^{(3)}_{xxyy}, \chi^{(3)}_{xyxy}, \chi^{(3)}_{xyyx}$, where the frequency arguments are omitted for simplicity. An anisotropy coefficient can be defined as

$$\sigma = \frac{\chi^{(3)}_{xxxx} - (\chi^{(3)}_{xxyy} + \chi^{(3)}_{xyxy} + \chi^{(3)}_{xyyx})}{\chi^{(3)}_{xxxx}} \tag{7.8}$$

such that it becomes 0 for the isotropic case, when the sum of the off-diagonal elements equals $\chi^{(3)}_{xxxx}$. Moreover, for degenerate experiments, we can switch indices according to $\chi^{(3)}_{ijji}(-\omega;\omega,-\omega,\omega) = \chi^{(3)}_{ijij}(-\omega;-\omega,\omega,\omega)$ since the corresponding frequency arguments are identical, leaving only three independent tensor components. The "effective" 2PA coefficient will be expressed as the imaginary part of the complex "effective" third-order susceptibility.

For a general orientation of the electric field vector, the projections on the crystal's principal axes will determine the expression of the induced nonlinear polarization through the respective $\chi^{(3)}$ tensor elements. A simple method of measuring the crystal anisotropy is to place the crystal in the focus of a linearly polarized beam (minimum transmittance point in the Z-scan curve) and change the electric field projection on the crystal axes by rotating the input polarization using a wire-grid polarizer. By analyzing the behavior of the 2PA coefficient as a function of the rotation angle one can determine both $\chi^{(3)}_{xxxx}$ and σ, and this method was used in the past to measure anisotropy of the 3rd order susceptibility tensor in a variety of materials [84]. In Table 7.1 are summarized the expressions of the effective contributions for linear and circular polarized light for three different crystal cuts. It should be noted here that in general, for complete determination of all tensor elements, at least two different measurements are needed since decoupling of the off-diagonal terms is needed. This can be achieved either by using linear polarization and two different cuts, or the use of a circularly polarized beam. By looking at the expressions in Table 7.1, it is obvious that for a (111) crystal orientation this method is not particularly useful as the 2PA coefficient does not depend on the rotation angle, but the extracted value is still useful when used in conjunction with other measurements.

Table 7.1 Effective contributions from off-diagonal $\chi^{(3)}$ components of a zincblende semiconductor ($\bar{4}3m$ class) for several polarization and crystal cut combinations.

Polarization	(100) cut	(111) cut	(110) cut
Linear	$\chi_{xxxx}\left[1-\frac{\sigma}{2}\sin^2(2\theta)\right]$	$\chi_{xxxx}\left[1-\frac{\sigma}{2}\right]$	$\chi_{xxxx}\left[1-\frac{\sigma}{2}\left(1+3\cos^2(\theta)\right)\sin^2(\theta)\right]$
Circular	$2\chi_{xyyx}+\frac{\sigma}{2}\chi_{xxxx}$	$2\chi_{xyyx}+\frac{3\sigma}{2}\chi_{xxxx}$	$2\chi_{xyyx}+\frac{\sigma}{3}\chi_{xxxx}$

For the case of InSb, we were mostly interested in determining whether the anisotropy plays an important role when measuring 2PA. Given the complex interplay of nonlinear effects, it is desirable to eliminate the uncertainty in magnitude arising from using different configurations. The only elements affecting the polarization of the IR beams were the wire-grid polarizers and the Babinet-Soleil compensator. Therefore rotation of polarization with respect to the crystal axes can be achieved in two different ways. First the prisms in the compensator were aligned to give a λ/4 phase shift (quarter-wave) and then the polarization was rotated using one of the wire-grid polarizers. The circular polarization was verified by measuring a constant energy transmitted through the polarizer. Also, for a linear polarization, the sample can also be rotated around the propagation direction of the beam at normal incidence. This is in general avoided since the inhomogeneities in the sample may cause problems when the rotation axis is slightly shifted from the beam axis. Fig. 7.13 (a) shows the transmitted signal when the sample is kept in focus and the polarization is rotated by 180 degrees. The total nonlinear transmittance in the focus was about 0.7. For a (100) cut the variation of the 2PA coefficient is given by

$\alpha_2(\theta) = \alpha_2(0)[1 + \frac{\sigma}{2}\sin^2(2\theta)]$ and this is shown in Fig. 7.13 (b). A variation by +/-1.5% in the transmittance would suggest a maximum anisotropy value of 0.2 for InSb. This is however just an upper limit given the noise level for this data.

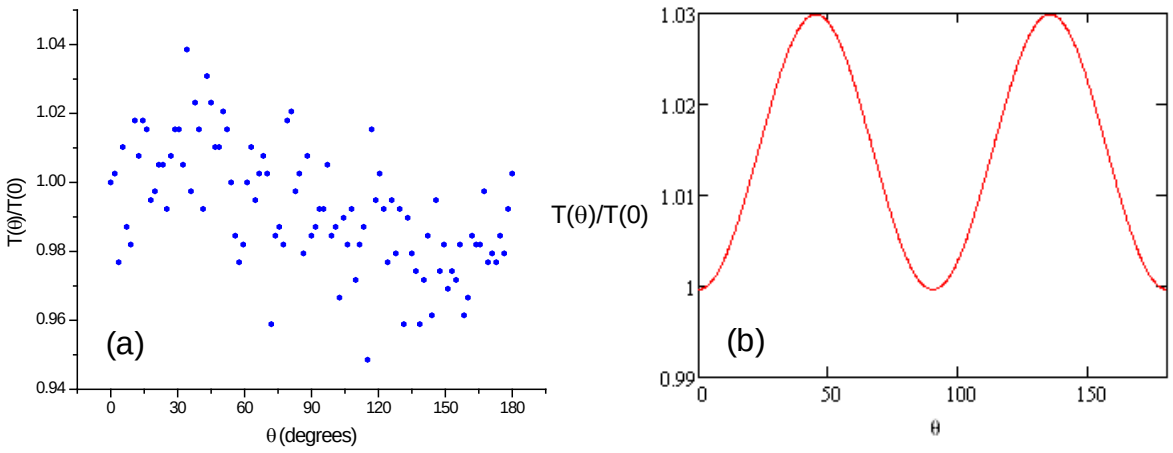

Figure 7.13 Experimental (a) and theoretical (b) variation of the nonlinear transmittance in focus with polarization angle for a (100) cut InSb sample at a wavelength of 10 μm using 9 ps pulses.

Also, the variation in the signal seen has a different periodicity and we believe is mainly given by a small ellipticity in the beam. A theoretical calculation of the 2PA anisotropy was made in Ref. [24] based on a 7-band model for zincblende structures and an empirical approximate formula was proposed. It was shown that anisotropy was mainly influenced by the position of higher conduction bands such that the anisotropy coefficient can be calculated according to

$$\sigma \approx -\frac{2E_{gap}}{E_{gap} + E_{cond}} \tag{5.9}$$

In InSb the next conduction band is situated at 3.1 eV [24, 72] giving an anisotropy value of about 0.1, in somewhat agreement with the experiment since such small anisotropy would

produce a variation in signal of +/- 0.75%, impossible to isolate with our noise level. The conclusion that can be drawn here is that for our experiments anisotropy wasn't an influencing factor. For the time-resolved experiments in particular, the perpendicular polarizations used simply make the "self" and "cross" 2PA coefficients different and therefore the values were fitted independently. A similar but more detailed discussion will be given in the next section.

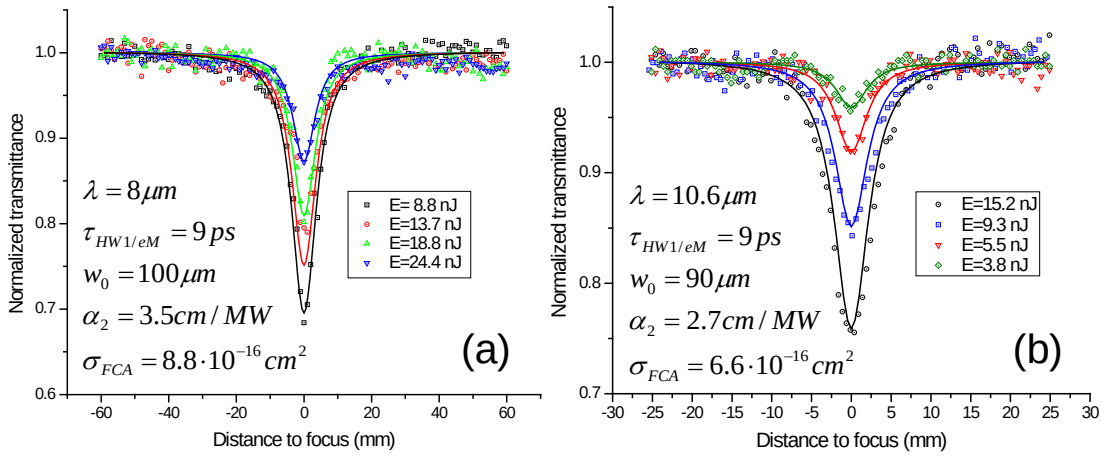

Figure 7.14 Closed aperture Z-scans at 8 μm (a) and 10.6 μm (b).

Fig. 7.14 shows typical open-aperture Z-scan curves taken with picosecond pulses. In (a) data is taken at 8 μm and in (b) at 10.6 μm. The fitting took into account FCA as well as 2PA. The contribution to absorption from FCA is non-negligible and quantifiable. The values obtained from the picosecond Z-scans are generally larger than the femtosecond ones but considering our estimated absolute errors (~±30%) there is a reasonable overlap. A more comprehensive study of 2PA with wavelength and temperature was done by Peter Olszak [74] and the results were shown to be in a reasonable agreement with the theoretical results of Ref. [82].

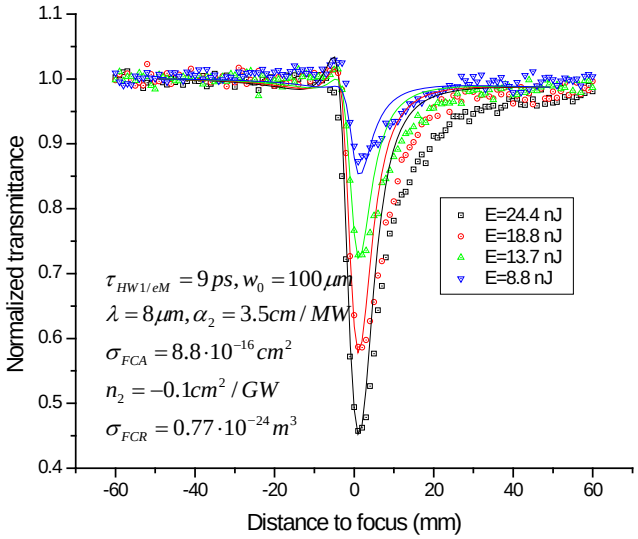

Figure 7.15 Closed-aperture Z-scans at λ = 8 μm.

Closed-aperture Z-scans were taken at 8 μm to estimate the magnitude of free-carrier refractive effects. Fig 7.15 shows the recorded data and the fitting parameters. The analysis shows that FCR is much larger than the contribution from the negative n_2 expected at this wavelength [8], but for consistency we used the theoretical value of n_2 for fitting even though the effects were minimal. An expected value for the free-carrier refraction cross-section can be obtained using the standard Drude-Loretz classical model. The change in the refractive index per generated free carrier per unit volume is

$$\sigma_{ref} = -\frac{e^2}{2\varepsilon_0 m_{car} n_0 \omega^2} \tag{5.10}$$

where m_{car} is the effective mass of the electron or hole. A direct consequence that can be pointed to here is that for the case of refraction the contribution from holes is much smaller due to the much larger effective mass, exactly the opposite of the absorptive case. To account for the

interband transitions contributing to nonlinear refraction, the previous formula can be corrected [85] yielding the following form

$$\sigma_{ref} = -\frac{e^2}{2\varepsilon_0 m_{car} n_0 \omega^2} \frac{E_G^2}{E_G^2 - \hbar^2 \omega^2} \tag{5.11}$$

The value obtained using this model is $1.8*10^{-24}$ m^3, which is about a factor of 2 smaller than the fitted value of $0.77*10^{-24}$ m^3. Similar discrepancies were observed in Ref. [76] and were resolved by employing a more detailed calculation of the shape for the conduction band.

7.3.2. Time-resolved experiments

Separation of instantaneous from the long lived nonlinear effects can be easily done through excite-probe experiments. The degenerate experiments also allow for the determination of the pulse duration which would be otherwise needed to be done in a separate experiment. Using a large range of delays using one set of data one can calculate 2PA, FCA and the Auger coefficient through a carrier density dependent lifetime.

Considering the third-order nonlinearities of interest here, we write the induced nonlinear polarization at frequency ω_i and direction $\mathbf{k}_i$ as a function of component field amplitudes

$$P_i^{(3)}(\omega_i, \mathbf{k}_i) = \frac{\varepsilon_0}{4} \sum_{jkl} \chi_{ijkl}^{(3)}(-\omega_i; \omega_j, \omega_k, \omega_l) E_j(\omega_j, \mathbf{k}_j) E_k(\omega_k, \mathbf{k}_k) E_l(\omega_l, \mathbf{k}_l) \tag{7.12}$$

For our cubic symmetry we can choose to write the nonlinear polarization in the Cartesian coordinate system associated with the principal crystallographic axes denoted by [100], [010] and [001], such that *i, j, k* and *l* correspond to these directions. Similarly to the single beam experiments, polarizations of the two beams and the crystal orientation will determine the effective magnitudes of the nonlinear coefficients involved. In general, for a two-beam

experiment, we need to detect an arbitrary component of the field generated by input fields of arbitrary polarization incident on a crystal of arbitrary orientation. It is therefore useful to use the frame of reference associated with the incident and detected radiation. Following Ref. [86] we can write the Fourier component of the nonlinear polarization at frequency ω_a and polarized in a direction given by unit vector $\hat{\mathbf{a}}$ as

$$P_a^{(3)}(\omega_a, \mathbf{k}_a) = \frac{\varepsilon_0}{4} \sum_{bcd} \sum_{ijkl} \chi_{ijkl}^{(3)}(-\omega_a; \omega_b, \omega_c, \omega_d) a_i^* b_j c_k d_l E_b(\omega_b, \mathbf{k}_b) E_c(\omega_c, \mathbf{k}_c) E_d(\omega_d, \mathbf{k}_d) \quad (7.13)$$

where a_i, b_j, c_k and d_l are the direction cosines for the projections of the initial fields in Eq. 7.12 onto the directions $\hat{\mathbf{i}}, \hat{\mathbf{j}}, \hat{\mathbf{k}}$ and $\hat{\mathbf{l}}$, respectively. Here the unit vectors for polarizations are taken as complex to include also circular polarizations. For our zincblende structures, using symmetry properties we can simply write the particular component of the nonlinear polarization as

$$P_z^{(3)} = \frac{\varepsilon_0}{4} \sum_{bcd} \chi_{eff}(a; b, c, d) E_b E_c E_d \quad (7.14)$$

where

$$\chi_{eff}(a; b, c, d) = \chi_{xxyy}(\hat{\mathbf{a}}^* \cdot \hat{\mathbf{b}})(\hat{\mathbf{c}} \cdot \hat{\mathbf{d}}) + \chi_{xyyx}(\hat{\mathbf{a}}^* \cdot \hat{\mathbf{d}})(\hat{\mathbf{b}} \cdot \hat{\mathbf{c}}) + \chi_{xyxy}(\hat{\mathbf{a}}^* \cdot \hat{\mathbf{c}})(\hat{\mathbf{b}} \cdot \hat{\mathbf{d}}) + \sigma \chi_{xxxx} \sum_i a_i^* b_i c_i d_i \quad (7.15)$$

This is a general formula that can be used for all cubic or isotropic media whether the processes are degenerate or non-degenerate [86]. The summation in Eq. 7.15 contains the dependence on the crystal orientation.

Let us consider now our degenerate pump-probe experiments using linear polarizations. We shall denote the excitation and probe beam polarization directions by $\hat{\mathbf{e}}$ and $\hat{\mathbf{p}}$ with $\hat{\mathbf{q}}$ being the

unit vector of the direction perpendicular to $\hat{\mathbf{e}}$ and the direction of propagation as seen in Fig. 7.16. We have described in Chapter 3 the coupled system of differential equations (Eq. 3.5 and 3.6) governing the propagation of both the excite and the probe beams in the medium. Using the above formalism, we can write the self and cross 2PA coefficients for the excite beam as

$$\alpha_2^{ee} = \frac{\omega}{2n^2c^2\varepsilon_0}\mathrm{Im}\left\{\chi_{eff}(e;e^*,e,e)\right\} = \frac{\omega}{2n^2c^2\varepsilon_0}\mathrm{Im}\left\{\chi_{xxyy}\left|\hat{\mathbf{e}}\cdot\hat{\mathbf{e}}\right|^2 + 2\chi_{xyyx} + \sigma\chi_{xxxx}\sum_i\left|e_i\right|^4\right\} \quad (7.16)$$

$$\begin{aligned}\alpha_2^{ep} &= \frac{\omega}{2n^2c^2\varepsilon_0}2\,\mathrm{Im}\left\{\chi_{eff}(e;p^*,e,p)\right\} = \\ &= \frac{\omega}{n^2c^2\varepsilon_0}\mathrm{Im}\left\{\chi_{xxyy}\left|\hat{\mathbf{p}}\cdot\hat{\mathbf{e}}\right|^2 + \chi_{xyyx}(1+\left|\hat{\mathbf{p}}^*\cdot\hat{\mathbf{e}}\right|^2) + \sigma\chi_{xxxx}\sum_i\left|e_i\right|^2\left|p_i\right|^2\right\}\end{aligned} \quad (7.17)$$

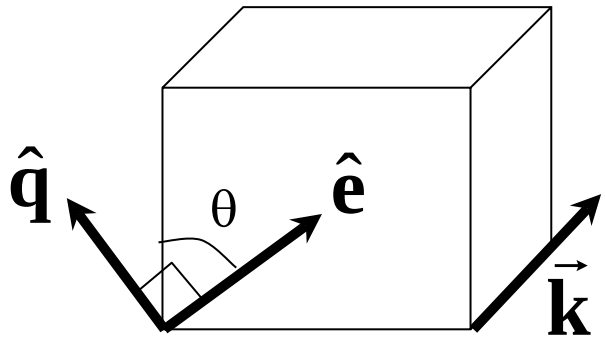

Figure 7.16 Input polarizations in a pump-probe experiment for beams propagating normal to the surface of the sample.

The coefficients for the probe beam can be obtained simply by substituting the appropriate unit vectors for polarization. In our experiments the self-induced 2PA by the probe will be neglected as the irradiance of the probe is negligible and so we shall concentrate on the expressions of the self-induced 2PA by the excite beam (important for calculation of the generation rate for carriers) and of the cross-terms (important in the propagation equation for the probe pulse), for parallel and perpendicular polarizations.

For the parallel polarizations of the excite and probe beams, we take $\hat{\mathbf{p}} = \hat{\mathbf{e}}$ and the 2PA coefficients becomes equal to

$$\alpha_2^{ee} = \frac{\omega}{2n^2c^2\varepsilon_0}\mathrm{Im}\left\{\chi_{xxyy} + 2\chi_{xyyx} + \sigma\chi_{xxxx}\sum_i |e_i|^4\right\} = \frac{\omega}{2n^2c^2\varepsilon_0}\mathrm{Im}\{\chi_{xxxx}\}\left[1 - \sigma + \sigma\sum_i |e_i|^4\right] \quad (7.18)$$

$$\alpha_{2,//}^{pe} = \frac{\omega}{n^2c^2\varepsilon_0}\mathrm{Im}\left\{\chi_{xxyy} + 2\chi_{xyyx} + \sigma\chi_{xxxx}\sum_i |e_i|^4\right\} = 2\alpha_2^{ee} \quad (7.19)$$

It's important to remember then that in the case of parallel polarizations, the cross terms are exactly 2 times larger than the self-induced ones, regardless of the crystal orientation. This is the absorptive equivalent of the "weak-wave retardation" effect [87] associated with the real part of the third-order susceptibility term.

When the polarization of the probe beam is perpendicular to one of the excite beams, $\hat{\mathbf{p}} = \hat{\mathbf{q}}$, we obtain

$$\alpha_{2,\perp}^{pe} = \frac{\omega}{n^2c^2\varepsilon_0}\mathrm{Im}\left\{\chi_{xyyx} + \sigma\chi_{xxxx}\sum_i |e_i|^2|q_i|^2\right\} \quad (7.20)$$

Next, we calculate the actual expressions for our (100) cut for the two polarization configurations. For this crystal orientation, assuming an arbitrary orientation of the excite beam polarization with respect to the crystallographic axes, we write

$$\begin{aligned}\hat{\mathbf{e}} &= \cos(\theta)\hat{\mathbf{x}} + \sin(\theta)\hat{\mathbf{y}} \\ \hat{\mathbf{q}} &= \sin(\theta)\hat{\mathbf{x}} - \cos(\theta)\hat{\mathbf{y}}\end{aligned} \quad (7.21)$$

For this case the 2PA coefficients can be written as

$$\begin{aligned}\alpha_2^{ee} &= \frac{1}{2}\alpha_{2,//}^{pe} = \frac{\omega}{2n^2c^2\varepsilon_0}\mathrm{Im}\{\chi_{xxxx}\}\left[1 - \frac{\sigma}{2}\sin^2(2\theta)\right] \\ \alpha_{2,\perp}^{pe} &= \frac{\omega}{n^2c^2\varepsilon_0}\mathrm{Im}\left\{\chi_{xyyx} + \frac{\sigma}{2}\chi_{xxxx}\sin^2(2\theta)\right\}\end{aligned} \quad (7.22)$$

By looking at these expressions, we can conclude that in InSb (having a small anisotropy coefficient σ) for the perpendicular polarization case the self and cross terms depend almost exclusively on χ_{xxxx} and χ_{xyyx}, respectively. Therefore, when fitting the experimental data we need to assume two independent parameters for the two 2PA coefficients. The expressions for different crystal cuts are obtained in the same manner, by expressing the polarization unit vector in the Cartesian system associated with the principal crystallographic axes. The effective $\chi^{(3)}$ for the cross terms in 2PA assuming a perpendicularly polarized probe incident on (100), (110) and (111) cuts are given in Table 7.2.

Table 7.2 Effective third-order susceptibilities defining the cross 2PA term for different cuts and perpendicularly polarized probe in a zincblende structure.

Cuts	(100)	(110)	(111)
$\chi_{eff}^{(3)}$	$\chi_{xyyx}+\frac{\sigma}{2}\chi_{xxxx}\sin^2(2\theta)$	$\chi_{xyyx}+\frac{3\sigma}{8}\chi_{xxxx}\sin^2(2\theta)$	$\chi_{xyyx}+\frac{\sigma}{6}\chi_{xxxx}$

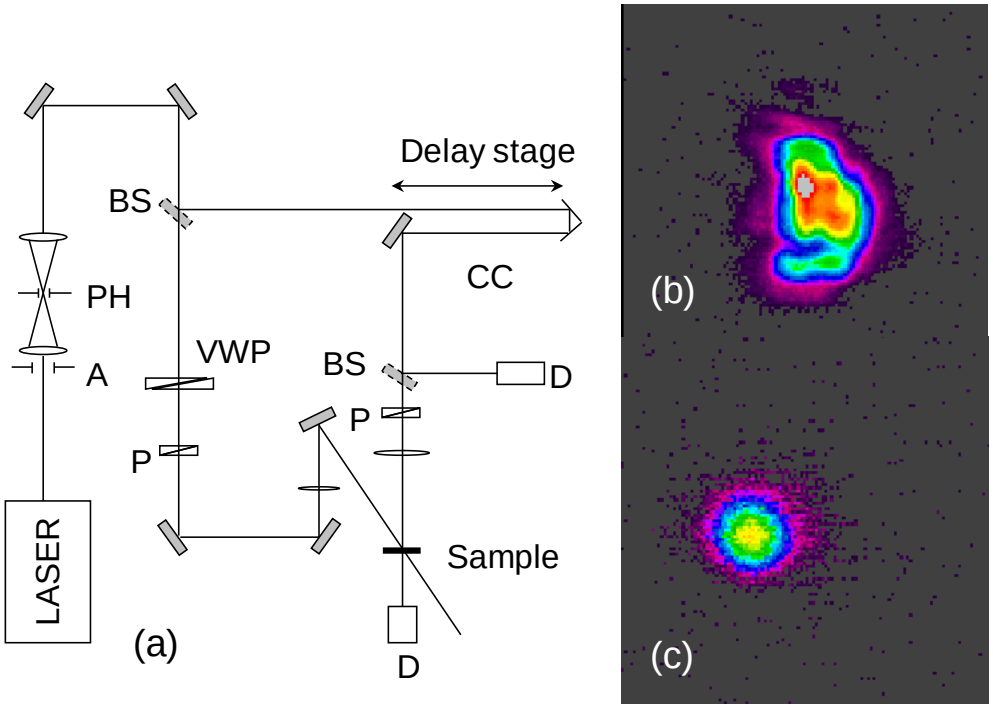

Figure 7.17 Layout of the pump-probe setup (a) and typical unfiltered (b) and filtered (c) spatial beam profiles.

The standard setup used for our time-resolved experiments and typical beam profiles are shown in Fig. 7.17. Usually, the beam quality of our mid-IR wavelengths coming straight out of DFG part of the parametric device wasn't very good. Therefore, before any experiment, we passed the beam through a spatial filtering setup consisting of an input aperture and a telescope with a pinhole (500 μm size) in the focal spot. The energy losses were of about 50% but this way we were able to reach a compromise, sacrificing the total usable energy in order to obtain a better spatial quality.

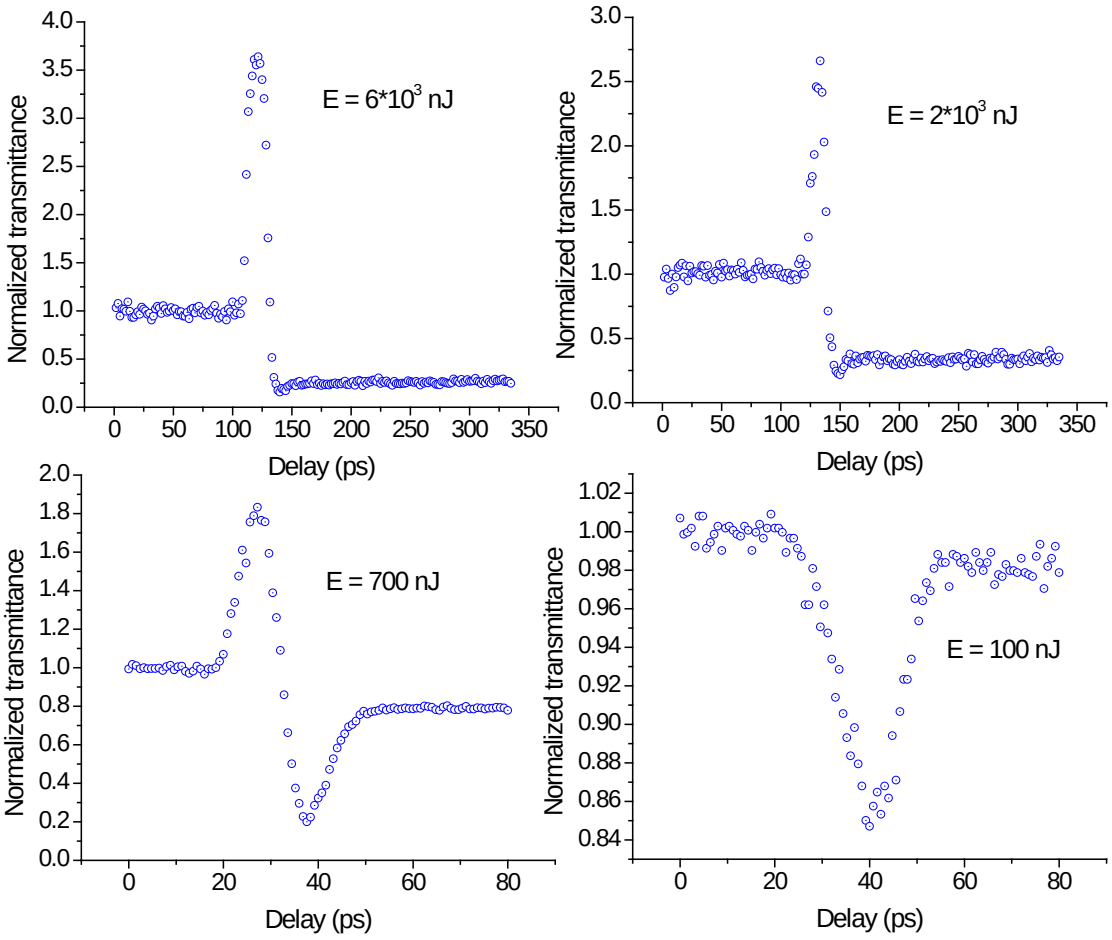

Figure 7.18 Pump-probe curves at 10 μm with parallel polarizations at room temp with 9 ps pulses.

The first pump-probe experiments were attempted using parallel polarizations. Typical data is shown in Fig. 7.18 for several pump energies. In this case, the interference term produces a transient grating scattering light from the pump beam into the direction of the probe beam during the pulse overlap time where the excite and probe are coherent with each other (so-called "coherent artifact") [88]. Since our probe energies were comparatively much lower, even a non-efficient transfer will cause a large change in the signal measured, as seen in the experimental data. These "coherent artifacts" were studied in GaAs [89, 90] and the effects of scattering of the

incident radiation off multiple gratings (absorptive or refractive and associated with either instantaneous or free-carrier effects, and photorefractive effects) were analyzed. For our case we can only eliminate the photorefractive effect as a possible cause since rotation of the sample didn't affect the signal.

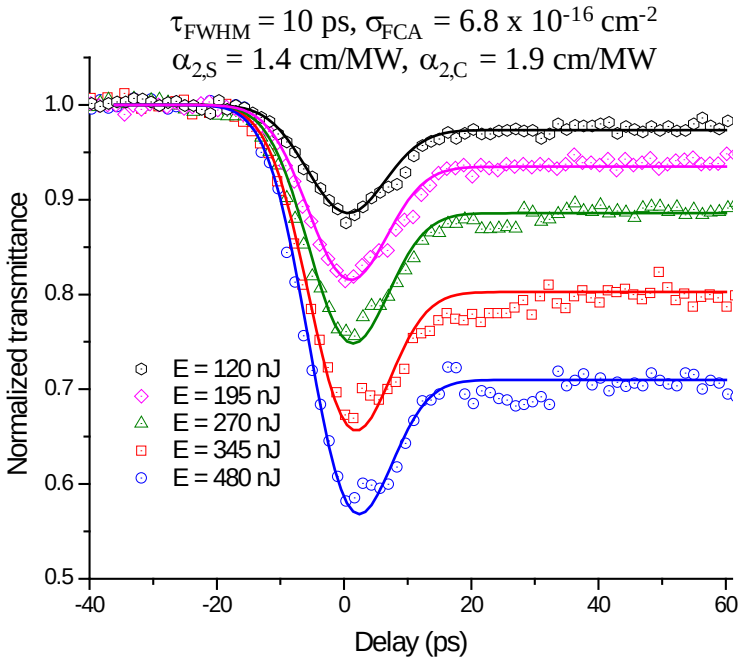

Figure 7.19 Pump-probe data at 10 μm using perpendicular polarizations.

To avoid such effects that would highly complicate our analysis aimed at quantifying 2PA and FCA effects, we used perpendicular polarizations in all our experiments. Fig. 7.19 shows typical pump probe experiments at 10 μm. All the data sets are fit with the same parameters, which will be used also for long delay measurements aimed at characterizing the population dynamics. In our fits we used a FCA absorption cross-section of $6.8*10^{-16}$ cm^2, the value extracted from the FTIR measurements. The values obtained for the self and cross 2PA are 1.4 cm/MW and 1.9 cm/MW, respectively. As mentioned in the previous paragraphs, InSb has a small anisotropy

coefficient making the two coefficients effectively proportional to $\mathrm{Im}\{\chi_{xxxx}\}$ and $2\,\mathrm{Im}\{\chi_{xyyx}\}$, respectively. This suggests a ratio of the two coefficients of about 0.68 which is reasonable considering that its maximum possible value is about 1.2, when the other off-diagonal components are zero.

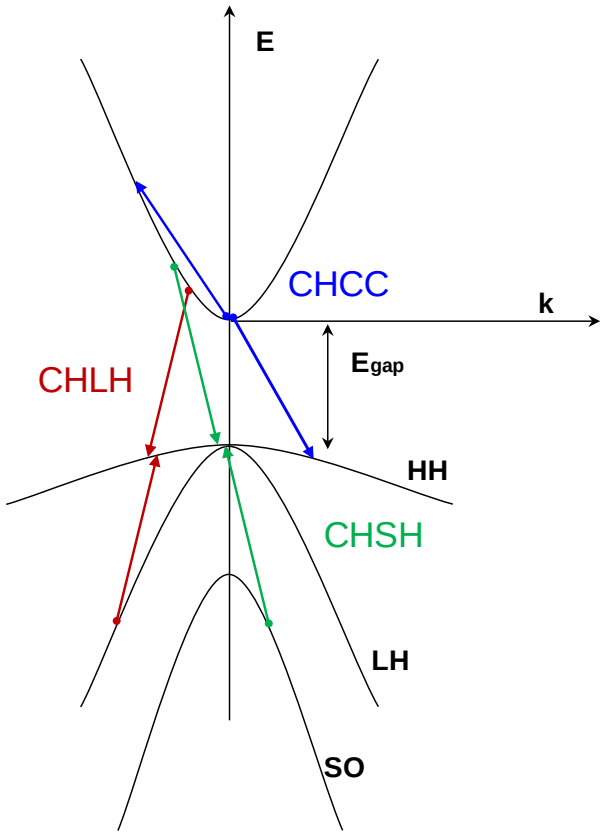

Figure 7.20 Auger recombination process in a direct-gap semiconductor. The different colors correspond to different carrier pairs involved.

An important relaxation process in direct-gap semiconductors is Auger recombination. The recombination of a hole with an electron is an exoenergetic process. The extra energy can be given to another particle (electron or hole) which subsequently is promoted to a higher energetic level (see Fig. 7.20). During the process both energy and momentum are conserved. Depending on the position of the initial states, there are three different channels, denoted by CCHC, CCLH,

and CCSH. This process is a 3-particle process so it depends strongly on the carrier densities. A rigorous analysis would use Fermi-Dirac distributions, but assuming Boltzmann distributions one can obtain simple relations as in Eq. 7.4 pointing out a dependence of the rate on the cube of the carrier density. The Auger recombination is very important particularly in narrow gap semiconductors since it becomes the main relaxation mechanism at higher carrier densities. It negatively affects devices, e.g. optical limiters, by essentially shortening the lifetime of carriers in the excited state. This has been acknowledged as an important factor determining the performance of semiconductor lasers [91], light emitting diodes [92], solar cells [93] and infrared detectors [94].

Early theoretical treatments were made by Beattie [95] and Haug [96]. The relaxation rate was considered to have either a cubic dependence (Beattie) or a quadratic one (Haug) with the carrier density. The experimental data published on bulk InSb is limited. Fauchet *et al.* [97] created a laser-induced electron-hole plasma and studied the recombination through a reflection technique. The quadratic dependence gave the best fit while the cubic value for the Auger coefficient was found to be 2 orders of magnitude smaller than the value predicted theoretically by Beattie. A similar experiment made by Almazov [98], also gave better agreement with the quadratic dependence while the cubic fit gave a value of only one order of magnitude smaller than the theoretical one. An experiment carried out by Chazapis [99] with midinfrared picosecond pulses suggests a quadratic dependence as well. Recent work [76] has shown that a cubic dependence (Eq.7.4) yields similar results to a full analysis using Fermi-Dirac distributions when fitting experimental data. The authors explained the disagreement between the theory and experiment based on the approximations made in the interpretations of the previous numerical results.

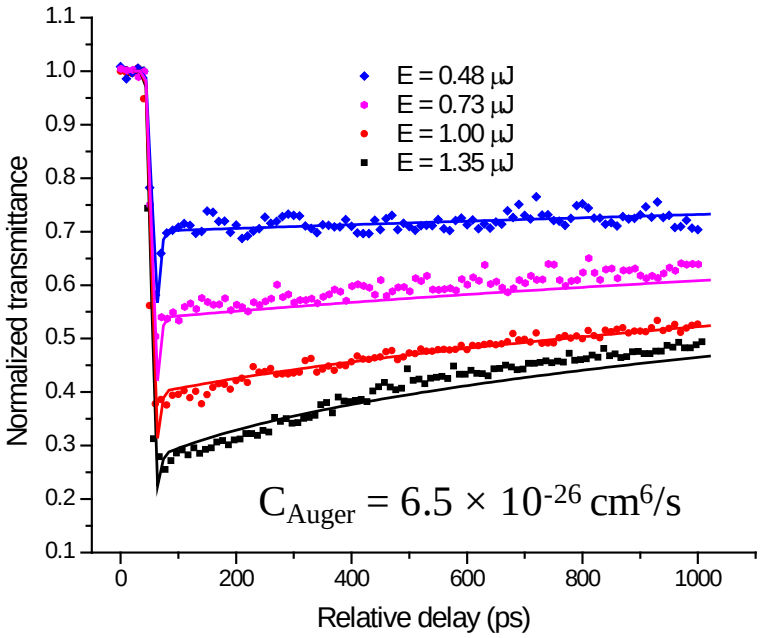

Figure 7.21 Long delay pump probe experiments on InSb at 10 μm with perpendicular polarizations. The parameters used were the same as for the shorter scans of Fig. 7.19.

Most of the experimental data relied on generating very large populations, especially through linear absorption. For this kind of experiment issues like recombination through surface states need to be carefully considered [99]. In our experiments, we used a different approach. The free-carriers were generated through a 2PA process which ensures a larger penetration depth while the maximum densities reached were not as large. The populations obtained were large enough however to observe recombination on a ps time scale. At room temperature the lifetime of carriers is about 160 ns, while the natural lifetime is about 2 μs [100, 101]. These numbers are large enough that for our regular (small signal) time-resolved experiments we can ignore all other relaxation processes. We were able to achieve changes in transmission levels of about 80%, using the maximum energies available. By scanning a longer delay, approximately 1ns, we can

see a decrease in effective lifetime as the generated carrier densities increased. Fig. 7.21 shows the experimental curves for perpendicular polarizations of pump and probe. The fitting parameters were the same as in the case of shorter scans (Fig 7.19). The Auger coefficient obtained was in agreement with the value calculated in Ref. [76]. Moreover, limiting data taken by Peter Olszak with nanosecond pulses [74] was fit with a similar value, $7*10^{-26}$ cm^6s^{-1}, increasing the degree of confidence in these measurements.

CHAPTER 8: CONCLUSION

8.1. Summary

The purpose of this work was to re-visit the existing theories on nonlinearities in semiconductors, to identify limitation on their applicability and to propose improved approaches, and to characterize the nonlinear properties of a narrow-band semiconductor (InSb) given the complex interplay of different physical mechanisms.

The existing models for calculation of 2PA and the nonlinear refraction index (n_2) were discussed and used in order to extend predictions on the nonlinear behavior in the highly non-degenerate frequency limit. Theoretically, 2PA was expected to increase dramatically since in this case both frequencies approach resonances for the "self" and "direct" transitions. We performed a detailed experimental investigation using the pump-probe technique employing both picosecond and femtosecond pulses in several semiconductors (GaAs, CdTe, ZnO, ZnS, ZnSe). The subsequent analysis has shown an extremely large enhancement of the nondegenerate 2PA with respect to the corresponding degenerate values. We obtained enhancement factors as large as 180 in CdTe using pump pulses at 8.9 μm (corresponding to approximately 9.4% of the bandgap) and probing at wavelengths close to the linear absorption edge (corresponding energies as large as 96% of the bandgap). We obtained good agreement with a simple 2-parabolic band theory for all the materials investigated. This large enhancement looks promising for applications like all-optical switching, gated detection and two-photon emission (2PE) and two-photon laser gain in semiconductors [32, 53, 54].

The analysis of existing 3PA experimental data allowed us to identify the limits of applicability for the existing theories using perturbative or "dressed-state" approaches. We

developed a more comprehensive model for zincblende structures based on the $\mathbf{k}\cdot\mathbf{p}$ theory proposed by Kane [23]. The calculation using third-order perturbation theory showed a strong quantum interference of transitions between the same energy levels but using different paths in the more complex 4-band structure employed. We showed the existing simple 2-band calculations cannot be used to predict this behavior for 3PA and compared it to 2PA which has fewer pathways and therefore shows a much less pronounced quantum interference. The theoretically predicted spectra were compared to the experimental ones in a few semiconductors (ZnSe, ZnS, GaAs) with very good agreement in both shape and even in magnitude (within a factor of 3). These calculations may prove useful by identifying low loss spectral regions for THz generation experiments using intense femtosecond pulses [61].

Bound electronic and free-carrier nonlinearities were studied in InSb using mid-IR femtosecond and picosecond pulses. The use of the shorter, femtosecond pulses allowed us to isolate the quasi-instantaneous effects from longer lived carrier associated ones and obtain directly 2PA at several wavelengths around the peak. Although noisy and incapable of producing a quantitative result, our closed-aperture scans showed the expected change in the sign of n_2 around the peak of 2PA and the strong influence of absorptive effects as predicted by the numerical simulations. We were able to extract from the picosecond experimental data using both open and closed-aperture scans 2PA coefficients and free-carrier absorption and refraction cross-sections. The analysis revealed that for these longer pulses free-carrier effects become much more important and even dominant in the case of refraction. The 2PA values obtained are in agreement with newer theoretical calculations [82] and the experimental values obtained from the femtosecond experiments. The FCA cross-sections also agreed with our linear FTIR measurements for the respective wavelengths which also have shown a clear dependence on

sample temperature, demonstrated for the first time. The FCR values were also shown to be in agreement with previous measurements and theoretical analyses [76, 82]. The time-resolved measurements demonstrated a good decoupling of FCA from 2PA and allowed us to isolate two different off-diagonal elements of the $\chi^{(3)}$ tensor by employing perpendicular polarizations for the interacting beams. Using longer delays and much larger input irradiances to induce larger population densities, we were also able to observe relaxation of photo-generated carriers on a ps time scale and measure the respective Auger coefficients. Our numbers are consistent with the calculated values from the literature [76] and were successfully used to interpret optical limiting data taken with nanosecond pulses [74].

8.2. Future Work

The work described in this dissertation was meant to answer some questions and fortunately, also indicated some interesting other venues to be explored. The particular issues that are deemed worthy of further investigation will be outlined below.

The large enhancements seen in 2PA for the extremely nondegenerate case indicate potential applications for optical switching. Feasibility of such experiments in guided geometries should be further explored. Furthermore, the extreme behavior of the nonlinear Kerr coefficient (n_2) needs to be verified experimentally, preferably with longer pulses (picosecond) having much narrower spectral widths for improved resolution. The large absorption effects pose considerable problems and will have to be circumvented. Also, the effects of strong varying n_2 over the larger spectral width of femtosecond pulses would be interesting to investigate from the point of view of phenomena like optical shocks and wave breaking [102].

Arguably the most interesting consequence of the demonstrated strong enhancement of 2PA in extremely frequency nondegenerate schemes is the possibility of observing two-photon emission and two-photon gain in systems with population inversion. A comprehensive theoretical study is necessary to establish the ideal experimental conditions to maximize the current extremely low output [32, 54]. There are still many unanswered questions related to this types of experiments which resolved can significantly shorten the path towards achieving two-photon lasing.

The analysis of the degenerate 3PA in zincblende structures can be extended to a more complex 7-band model [24] to predict anisotropy. A significant anisotropy of 3PA in GaAs has already been demonstrated [61]. Also, the extension of this approach to other crystal symmetries can be made allowing for a better understanding of other materials' spectra.

An interesting problem related to the InSb experiments was the presents of the "coherent artifacts". A good theoretical model to explain the behavior seen should be developed. The anisotropy of the 2PA merits further attention as experiments employing different polarizations and different crystal cuts would help isolate and determine with good precision the off-diagonal elements of the $\chi^{(3)}$ tensor. Another interesting topic that can be investigated is the measured 2PA or 3PA with ultrafast (large bandwidth) pulses, either transform limited or with a well characterized chirp. In a semiconductor, the large spectral bandwidth of pulses would allow multiple types of nonlinear interactions of the present frequencies and these effects would be interesting to evaluate.

LIST OF REFERENCES

1. Denk W., Strickler J.H., and Webb W.W., "Two-photon laser scanning fluorescence microscopy". *Science*, 1990. **248**(4951): p. 73-76.
2. So P.T.C., Dong C.Y., Masters B.R., and Berland K.M., "Two-photon excitation fluorescence microscopy". *Annual Review of Biomedical Engineering*, 2000. **2**: p. 399-429.
3. Maruo S., Nakamura O., and Kawata S., "Three-dimensional microfabrication with two-photon-absorbed photopolymerization". *Optics Letters*, 1997. **22**(2): p. 132-134.
4. Strickler J.H. and Webb W.W., "3-Dimensional Optical-Data Storage in Refractive Media by 2-Photon Point Excitation". *Optics Letters*, 1991. **16**(22): p. 1780-1782.
5. Van Stryland E.W., Wu Y.Y., Hagan D.J., Soileau M.J., and Mansour K., "Optical Limiting with Semiconductors". *Journal of the Optical Society of America B-Optical Physics*, 1988. **5**(9): p. 1980-1989.
6. Agrawal G.P., *Nonlinear fiber optics*. 2nd ed. Optics and photonics. 1995, San Diego: Academic Press. xviii, 592 p.
7. Mizrahi V., Delong K.W., Stegeman G.I., Saifi M.A., and Andrejco M.J., "2-Photon Absorption as a Limitation to All-Optical Switching". *Optics Letters*, 1989. **14**(20): p. 1140-1142.
8. Sheik-Bahae M., Hutchings D.C., Hagan D.J., and Vanstryland E.W., "Dispersion of Bound Electronic Nonlinear Refraction in Solids". *Ieee Journal of Quantum Electronics*, 1991. **27**(6): p. 1296-1309.

9. He J., Qu Y.L., Li H.P., Mi J., and Ji W., "Three-photon absorption in ZnO and ZnS crystals". *Optics Express*, 2005. **13**(23): p. 9235-9247.

10. Olszak P.D., Webster S., Padilha L.A., Cirloganu C.M., Woodall M., Hagan D.J., and Van Stryland E.W. "Energy Band-Gap Dependence of Three-Photon Absorption in Semiconductors". in *Nonlinear Optics: Materials, Fundamentals and Applications*. 2007: Optical Society of America.

11. Doviak J.M., Gibson A.F., Kimmitt M.F., and Walker A.C., "2-Photon Absorption in Indium-Antimonide at 10.6 μm". *Journal of Physics C-Solid State Physics*, 1973. **6**(3): p. 593-600.

12. Miller A., Johnston A., Dempsey J., Smith J., Pidgeon C.R., and Holah G.D., "2-Photon Absorption in InSb and $Hg_{1-X}Cd_XTe$". *Journal of Physics C-Solid State Physics*, 1979. **12**(22): p. 4839-4849.

13. Murdin B.N., Merveille C., Kar A.K., Pidgeon C.R., Jaroszynski D.A., Ortega J.M., Prazeres R., and Glotin F., "Infrared Free-Electron Laser Measurement of Power Limiting by 2-Photon Absorption in Insb". *Optical and Quantum Electronics*, 1993. **25**(3): p. 171-175.

14. Sheik-Bahae M., Mukherjee P., and Kwok H.S., "2-Photon and 3-Photon Absorption-Coefficients of Insb". *Journal of the Optical Society of America B-Optical Physics*, 1986. **3**(3): p. 379-385.

15. Shen Y.R., *The principles of nonlinear optics*. 1984, New York: J. Wiley. xii, 563 p.

16. Franken P.A., Hill A.E., Peters C.W., and Weinreich G., "Generation of Optical Harmonics". *Physical Review Letters*, 1961. **7**(4): p. 118.

17. Boyd R.W., *Nonlinear optics*. 1992, Boston: Academic Press. xiii.

18. Stegeman G., *Nonlinear Optics*. class notes, 2007.

19. Hagan D., *Optical properties of materials*. class notes, 2008.

20. Sheikbahae M., Said A.A., Wei T.H., Hagan D.J., and Vanstryland E.W., "Sensitive Measurement of Optical Nonlinearities Using a Single Beam". *Ieee Journal of Quantum Electronics*, 1990. **26**(4): p. 760-769.

21. Weaire D., Wherrett B.S., Miller D.A.B., and Smith S.D., "Effect of Low-Power Non-Linear Refraction on Laser-Beam Propagation in Insb". *Optics Letters*, 1979. **4**(10): p. 331-333.

22. Arecchi F.T., Schulz-Dubois E.O., Stitch M.L., Colson W.B., Pellegrini C., and Renieri A., *Laser handbook*. 1972, Amsterdam, New York,: North-Holland Pub. Co., American Elsevier Pub. Co. v. <1-6 >.

23. Kane E.O., "Band structure of indium antimonide". *Journal of Physics and Chemistry of Solids*, 1957. **1**(4): p. 249-261.

24. Hutchings D.C. and Wherrett B.S., "THEORY OF ANISOTROPY OF 2-PHOTON ABSORPTION IN ZINCBLENDE SEMICONDUCTORS". *Physical Review B*, 1994. **49**(4): p. 2418-2426.

25. Hutchings D.C. and Wherrett B.S., "Theory of the anisotropy of ultrafast nonlinear refraction in zincblende semiconductors". *Physical Review B*, 1995. **52**(11): p. 8150-8159.

26. Lee C.C. and Fan H.Y., "2-Photon absorption with exciton effect for degenerate valence bands". *Physical Review B*, 1974. **9**(8): p. 3502-3516.

27. Brandi H.S. and Dearaujo C.B., "Multiphoton absorption-coefficien in solids - A universal curve". *Journal of Physics C-Solid State Physics*, 1983. **16**(30): p. 5929-5936.

28. Keldysh L.V., "IONIZATION IN FIELD OF A STRONG ELECTROMAGNETIC WAVE". *Soviet Physics Jetp-Ussr*, 1965. **20**(5): p. 1307-&.

29. Jones H.D. and Reiss H.R., "Intense field-effects in solids". *Physical Review B*, 1977. **16**(6): p. 2466-2473.

30. Sheik-Bahae M., "Quantum interference control of current in semiconductors: Universal scaling and polarization effects". *Physical Review B*, 1999. **60**(16): p. R11257-R11260.

31. Cirloganu C.M., Olszak P.D., Padilha L.A., Webster S., Hagan D.J., and Stryland E.W.V., "Three-photon absorption spectra of zinc blende semiconductors: theory and experiment". *Opt. Lett.*, 2008. **33**(22): p. 2626-2628.

32. Hayat A., Ginzburg P., and Orenstein M., "Measurement and Model of the Infrared Two-Photon Emission Spectrum of GaAs". *Physical Review Letters*, 2009. **103**(2).

33. Said A.A., Sheikbahae M., Hagan D.J., Wei T.H., Wang J., Young J., and Vanstryland E.W., "Determination of Bound-Electronic and Free-Carrier Nonlinearities in ZnSe, GaAs, CdTe, and ZnTe". *Journal of the Optical Society of America B-Optical Physics*, 1992. **9**(3): p. 405-414.

34. Vanstryland E.W., Woodall M.A., Vanherzeele H., and Soileau M.J., "Energy Band-Gap Dependence of 2-Photon Absorption". *Optics Letters*, 1985. **10**(10): p. 490-492.

35. Bolger J.A., Kar A.K., Wherrett B.S., Desalvo R., Hutchings D.C., and Hagan D.J., "Nondegenerate 2-photon absorption-spectra of ZnSe, ZnS and ZnO". *Optics Communications*, 1993. **97**(3-4): p. 203-209.

36. Balu M., Hales J., Hagan D.J., and Van Stryland E.W., "Dispersion of nonlinear refraction and two-photon absorption using a white-light continuum Z-scan". *Optics Express*, 2005. **13**(10): p. 3594-3599.

37. Negres R.A., Hales J.M., Hagan D.J., and Van Stryland E.W., "Experiment and analysis of two-photon absorption spectroscopy using a white-light continuum probe". *Ieee Journal of Quantum Electronics*, 2002. **38**(9): p. 1205-1216.

38. Johnston A.M., Pidgeon C.R., and Dempsey J., "Frequency-dependence of 2-photon absorption in InSb and $Hg_{1-X}Cd_XTe$". *Physical Review B*, 1980. **22**(2): p. 825-831.

39. Haeri M.B., Kingham S.R., and Milsom P.K., "Nonlinear absorption and refraction in indium arsenide". *Journal of Applied Physics*, 2006. **99**(1): p. -.

40. Hutchings D.C., Sheikbahae M., Hagan D.J., and Vanstryland E.W., "Kramers-Kronig Relations in Nonlinear Optics". *Optical and Quantum Electronics*, 1992. **24**(1): p. 1-30.

41. Hutchings D.C. and Vanstryland E.W., "Nondegenerate 2-photon absorption in zincblende semiconductors". *Journal of the Optical Society of America B-Optical Physics*, 1992. **9**(11): p. 2065-2074.

42. Hales J.M., Hagan D.J., Van Stryland E.W., Schafer K.J., Morales A.R., Belfield K.D., Pacher P., Kwon O., Zojer E., and Bredas J.L., "Resonant enhancement of two-photon absorption in substituted fluorene molecules". *Journal of Chemical Physics*, 2004. **121**(7): p. 3152-3160.

43. Wherrett B.S., "Scaling rules for multiphoton interband absorption in semiconductors". *Journal of the Optical Society of America B-Optical Physics*, 1984. **1**(1): p. 67-72.

44. Hutchings D.C. and Vanstryland E.W., "NONDEGENERATE 2-PHOTON ABSORPTION IN ZINC BLENDE SEMICONDUCTORS". *Journal of the Optical Society of America B-Optical Physics*, 1992. **9**(11): p. 2065-2074.

45. Vaidyanathan A., Walker T., Guenther A.H., Mitra S.S., and Narducci L.M., "2-PHOTON ABSORPTION IN SEVERAL DIRECT-GAP CRYSTALS". *Physical Review B*, 1980. **21**(2): p. 743-748.

46. Jones H.D. and Reiss H.R., "INTENSE-FIELD EFFECTS IN SOLIDS". *Physical Review B*, 1977. **16**(6): p. 2466-2473.

47. Bass M. and Optical Society of America., *Handbook of optics*. 2nd ed. 1995, New York: McGraw-Hill.

48. Ikeda K. and Fainman Y., "Material and structural criteria for ultra-fast Kerr nonlinear switching in optical resonant cavities". *Solid-State Electronics*, 2007. **51**(10): p. 1376-1380.

49. Stegeman G.I. and Torruellas T.E., "Nonlinear materials for information processing and communications". *Philosophical Transactions of the Royal Society of London Series a-Mathematical Physical and Engineering Sciences*, 1996. **354**(1708): p. 745-756.

50. Goldman S.P. and Drake G.W.F., "Relativistic 2-Photon Decay-Rates of 2s1/2 Hydrogenic Ions". *Physical Review A*, 1981. **24**(1): p. 183-191.

51. Pfister O., Brown W.J., Stenner M.D., and Gauthier D.J., "Two-photon stimulated emission in laser-driven alkali-metal atoms using an orthogonal pump-probe geometry". *Physical Review A*, 1999. **60**(6): p. R4249-R4252.

52. Pfister O., Brown W.J., Stenner M.D., and Gauthier D.J., "Polarization instabilities in a two-photon laser". *Physical Review Letters*, 2001. **86**(20): p. 4512-4515.

53. Ironside C.N., "2-Photon Gain Semiconductor Amplifier". *Ieee Journal of Quantum Electronics*, 1992. **28**(4): p. 842-847.

54. Hayat A., Ginzburg P., and Orenstein M., "Observation of two-photon emission from semiconductors". *Nat Photon*, 2008. **2**(4): p. 238-241.

55. Beerwerth F., Fröhlich D., Köhler P., Leinweber V., and Voss A., "Three-photon spectroscopy of excitons and polaritons in alkali halides". *Physical Review B*, 1988. **38**(6): p. 4250.

56. Catalano I.M., Cingolan.A, and Minafra A., "3-Photon luminescence in CdS". *Optics Communications*, 1974. **11**(3): p. 254-256.

57. Catalano I.M., Cingolani A., Ferrara M., and Minafra A., "3-Photon nonlinear cross-section of Gallium-Phosphide". *Optics Communications*, 1975. **15**(2): p. 281-283.

58. Catalano I.M., Cingolani A., and Minafra A., "Multiphoton impurity luminescence in zinc sulphide". *Optics Communications*, 1973. **7**(3): p. 270-271.

59. Fröhlich D., Kirchhoff S., Köhler P., and Nieswand W., "Three-photon difference-frequency spectroscopy of polaritons in alkali halides". *Physical Review B*, 1989. **40**(3): p. 1976.

60. Hasselbeck M.P., Said A.A., van Stryland E.W., and Sheik-Bahae M., "Three-photon absorption in InAs". *Optical and Quantum Electronics*, 1998. **30**(3): p. 193-200.

61. Hurlbut W.C., Lee Y.S., Vodopyanov K.L., Kuo P.S., and Fejer M.M., "Multiphoton absorption and nonlinear refraction of GaAs in the mid-infrared". *Optics Letters*, 2007. **32**(6): p. 668-670.

62. Lepore M., Tommasi R., and Catalano I.M., "Spectral behavior of 3-photon absorption-coefficient in II-VI-compounds - ZnO, CdS and ZnSe". *Solid State Communications*, 1992. **84**(4): p. 463-468.

63. Lepore M., Tommasi R., and Catalano I.M., "3-Photon-absorption spectroscopy in an indirect-gap material - CdI_2". *Physical Review B*, 1993. **47**(12): p. 7580-7583.

64. Mitra S.S., Judell N.H.K., Vaidyanathan A., and Guenther A.H., "3-Photon absorption in direct-gap crystals". *Optics Letters*, 1982. **7**(7): p. 307-309.

65. Pacebutas V., Krotkus A., Suski T., Perlin P., and Leszczynski M., "Photoconductive Z-scan measurement of multiphoton absorption in GaN". *Journal of Applied Physics*, 2002. **92**(11): p. 6930-6932.

66. Vivas M.G., Shih T., Voss T., Mazur E., and Mendonca C.R., "Nonlinear spectra of ZnO: reverse saturable, two- and three-photon absorption". *Optics Express*. **18**(9): p. 9628-9633.

67. Kang J.U., Villeneuve A., Sheikbahae M., Stegeman G.I., Alhemyari K., Aitchison J.S., and Ironside C.N., "Limitation due to 3-photon absorption on the useful spectral range for nonlinear optics in AlGaAs below half band-gap". *Applied Physics Letters*, 1994. **65**(2): p. 147-149.

68. Ashkinad.Bm, Ryvkin S.M., and Yaroshet.Id, "Thermal and Impact Ionization of Excitons in Gap in Case of 2-Photon Excitation". *Soviet Physics Semiconductors-Ussr*, 1969. **3**(4): p. 455-&.

69. Yu P.Y. and Cardona M., *Fundamentals of semiconductors: physics and materials properties*. 2nd updated ed. 1999, Berlin ; New York: Springer. xvi, 620 p.

70. Dresselhaus G., "Spin-Orbit Coupling Effects in Zinc Blende Structures". *Physical Review*, 1955. **100**(2): p. 580.

71. Dinu M., "Dispersion of phonon-assisted nonresonant third-order nonlinearities". *Ieee Journal of Quantum Electronics*, 2003. **39**(11): p. 1498-1503.

72. Hellwege K.H., Börnstein R., and Landolt H., *Zahlenwerte und Funktionen aus Naturwissenschaften und Technik, neue Serie*. 1961, Berlin,: Springer-Verlag. v.

73. Kaplan A.E., "“External” self-focusing of light by a nonlinear layer". *Radiophysics and Quantum Electronics*, 1969. **12**(6): p. 692-696.

74. Olszak P., *Nonlinear absorption and free-carrier recombination in direct gap semiconductors*, in *CREOL*. 2010, University of Central Florida: Orlando.

75. Weiler M.H., "Non-Parabolicity and Exciton Effects in 2-Photon Absorption in Zincblende Semiconductors". *Solid State Communications*, 1981. **39**(8): p. 937-940.

76. Dubikovskiy V., Hagan D.J., and Van Stryland E.W., "Large nonlinear refraction in InSb at 10 um and the effects of Auger recombination". *Journal of the Optical Society of America B-Optical Physics*, 2008. **25**(2): p. 223-235.

77. Van Stryland E.W., Vanherzeele H., Woodall M.A., Soileau M.J., Smirl A.L., Guha S., and Boggess T.F., "2 Photon-Absorption, Nonlinear Refraction, and Optical Limiting in Semiconductors". *Optical Engineering*, 1985. **24**(4): p. 613-623.

78. Hasselbeck M.P., VanStryland E.W., and SheikBahae M., "Dynamic band unblocking and leakage two-photon absorption in InSb". *Physical Review B*, 1997. **56**(12): p. 7395-7403.

79. Veitas G., *personal communication*. 2010.

80. LightConversion, *TOPAS manual*. 2003.

81. Kurnick S.W. and Powell J.M., "Optical Absorption in Pure Single Crystal InSb at 298 deg and 78 deg K". *Physical Review*, 1959. **116**(3): p. 597.

82. Krishnamurthy S., Yu Z.G., Gonzalez L.P., and Guha S., "Accurate evaluation of nonlinear absorption coefficients in InAs, InSb, and HgCdTe alloys". *Journal of Applied Physics*, 2007. **101**(11): p. -.

83. Bechtel J.H. and Smith W.L., "2-Photon Absorption in Semiconductors with Picosecond Laser-Pulses". *Physical Review B*, 1976. **13**(8): p. 3515-3522.

84. DeSalvo R., Sheikbahae M., Said A.A., Hagan D.J., and Vanstryland E.W., "Z-Scan Measurements of the Anisotropy of Nonlinear Refraction and Absorption in Crystals". *Optics Letters*, 1993. **18**(3): p. 194-196.

85. Auston D.H., Mcafee S., Shank C.V., Ippen E.P., and Teschke O., "Picosecond Spectroscopy of Semiconductors". *Solid-State Electronics*, 1978. **21**(1): p. 147-150.

86. Dvorak M.D., Schroeder W.A., Andersen D.R., Smirl A.L., and Wherrett B.S., "Measurement of the Anisotropy of 2-Photon Absorption-Coefficients in Zincblende Semiconductors". *Ieee Journal of Quantum Electronics*, 1994. **30**(2): p. 256-268.

87. Van Stryland E.W., Smirl A.L., Boggess T.F., Soileau M.J., Wherrett B.S., and Hopf F.A., "Weak-Wave Retardation and Phase-Conjugate Self-Defocusing in Si". *Applied Physics B-Photophysics and Laser Chemistry*, 1982. **29**(3): p. 159-160.

88. Palfrey S.L. and Heinz T.F., "Coherent Interactions in Pump-Probe Absorption-Measurements - the Effect of Phase Gratings". *Journal of the Optical Society of America B-Optical Physics*, 1985. **2**(4): p. 674-679.

89. Smirl A.L., Valley G.C., Bohnert K.M., and Boggess T.F., "Picosecond Photorefractive and Free-Carrier Transient Energy-Transfer in GaAs at 1-um". *Ieee Journal of Quantum Electronics*, 1988. **24**(2): p. 289-303.

90. Valley G.C. and Smirl A.L., "Theory of Transient Energy-Transfer in Gallium-Arsenide". *Ieee Journal of Quantum Electronics*, 1988. **24**(2): p. 304-310.

91. Sugimura A., "Auger Recombination Effect on Threshold Current of Ingaasp Quantum Well Lasers". *Ieee Journal of Quantum Electronics*, 1983. **19**(6): p. 932-941.

92. Bergh A.A. and Dean P.J., *Light-emitting diodes*. 1976, Oxford: Clarendon Press. viii, 591 p.

93. Vonroos O. and Landsberg P.T., "Effect of Recombination on the Open-Circuit Voltage of a Silicon Solar-Cell". *Journal of Applied Physics*, 1985. **57**(10): p. 4746-4751.

94. Grein C.H., Young P.M., Flatte M.E., and Ehrenreich H., "Long wavelength InAs/InGaSb infrared detectors: Optimization of carrier lifetimes". *Journal of Applied Physics*, 1995. **78**(12): p. 7143-7152.

95. Beattie A.R., "Auger Transitions in Semiconductors and Their Computation". *Journal of Physics C-Solid State Physics*, 1985. **18**(35): p. 6501-6515.

96. Haug A., "Carrier Density Dependence of Auger Recombination". *Solid-State Electronics*, 1978. **21**(11-1): p. 1281-1284.

97. Fauchet P.M., "The Auger Rate in Highly Excited Indium-Antimonide". *Physica Status Solidi B-Basic Research*, 1982. **110**(1): p. K11-K15.

98. Almazov L.A., Liptuga A.I., Malyutenko V.K., and Fedorenko L.L., "Properties of a High-Density Non-Equilibrium Plasma in InSb". *Soviet Physics Semiconductors-Ussr*, 1980. **14**(10): p. 1154-1158.

99. Chazapis V., Blom H.A., Vodopyanov K.L., Norman A.G., and Phillips C.C., "Midinfrared Picosecond Spectroscopy Studies of Auger Recombination in Insb". *Physical Review B*, 1995. **52**(4): p. 2516-2521.

100. Hilsum C., "Properties of p-type Indium Antimonide II: Photoelectric Properties and Carrier Lifetime". *Proceedings of the Physical Society*, 1959. **74**(1): p. 81.

101. Wertheim G.K., "Carrier Lifetime in Indium Antimonide". *Physical Review*, 1956. **104**(3): p. 662.

102. Rothenberg J.E., "Femtosecond optical shocks and wave breaking in fiber propagation". *J. Opt. Soc. Am. B*, 1989. **6**(12): p. 2392-2401.